THE MODELING AND USE OF SYNTACTIC FOAMS FOR PASSIVE CONTROL OF FLUID-BORNE NOISE

A Dissertation
Presented to
The Academic Faculty

By

Kenneth A. Marek

In Partial Fulfillment of the
Requirements for the Degree
Doctor of Philosophy in Mechanical Engineering

George W. Woodruff School of Mechanical Engineering
Georgia Institute of Technology
December 2014

THE MODELING AND USE OF SYNTACTIC FOAMS FOR PASSIVE CONTROL OF FLUID-BORNE NOISE

Approved by:

Dr. Kenneth A. Cunefare, Advisor
School of Mechanical Engineering
Georgia Institute of Technology

Dr. Laurence Jacobs
School of Civil and Environmental Engineering
Georgia Institute of Technology

Dr. Julien Meaud
School of Mechanical Engineering
Georgia Institute of Technology

Dr. Wayne Book
School of Mechanical Engineering (Emeritus)
Georgia Institute of Technology

Dr. Donggang Yao
School of Materials Science and Engineering
Georgia Institute of Technology

Date Approved: August 20, 2014

ACKNOWLEDGEMENTS

I would like to thank my academic advisor, Dr. Cunefare, for all his helpful input over the years. I extend my thanks also to my thesis committee, and to all the friends and family who have supported me over the last several years; and also specifically to Marilyn for her encouragement these last several months.

This research was supported by the Center for Compact and Efficient Fluid Power, a National Science Foundation Engineering Research Center funded under cooperative agreement number EEC-0540834.

TABLE OF CONTENTS

LIST OF TABLES

LIST OF FIGURES

LIST OF SYMBOLS

$A_{i,n}$, A_n	Forward travelling wave amplitude in region *i*, mode number *n*
$B_{i,n}$, B_n	Reverse travelling wave amplitude in region *i*, mode number *n*
E	Young's modulus
F	Perforate layer hole area fraction
F_H	Hard volume fraction of buckled microsphere versus original sphere volume
F_i	Volume fraction of component *i* versus total volume
G_B, G_U	Original volume fraction of microspheres which are currently buckled (B) or unbuckled (U)
J_m	Bessel function of the first kind, order *m*
K, K_i	Bulk modulus of component *i*
L_0, L_1, L_2	Noise suppressor length measurements
$L_{Pi,m}$	Acoustic sound pressure level for condition *i*, pressure index *m*
M, N	Number of solution modes; in Chapter 6, *M* is number of pressures considered in optimization, and N is number of frequencies
P_{atm}	Atmospheric pressure
P_c	Precharge gauge pressure

P_{cr}, P_{cr0}	Critical pressure at which spheres buckle; with subscript 0, nominal critical pressure
P_s	System gauge pressure
P_{tot}	Absolute system pressure
Q_i	Acoustic volume velocity
RMSE	Root mean squared error
T_m	Time weighting factor
TL	Transmission loss
Y_m	Bessel function of the second kind, order m
V, V_i	Volume
Z_0	Acoustic impedance
Z_p	Acoustic impedance across perforate layer
a, a_0	Prototype suppressor radial dimensions
a_h	Perforate layer hole radius
b, b_0	Prototype suppressor radial dimensions
c_i	Speed of sound in medium represented by i
e_e	Experimental error value

f	Frequency (in Hz)
k_i	Acoustic wavenumber for wave/medium i
k_r	Radial wavenumber
k_x	Axial wavenumber
$k_{Rx,n}$, $k_{Rri,n}$	Directional wavenumber in region R, mode number n; axial direction (x) or radial direction (r) with wave/medium type i
m_b	Bladder mass
p_i, $p_{R,n}$	Acoustic pressure corresponding to value i; or in region R, mode number n
q	Perforate layer hole separation distance
q_i	Acoustic velocity
r, r_i	radial measurement or location
t	Time, or thickness
t_{ij}	Transfer matrix elements
$u_{r,n}$, $u_{x,n}$, $u_{Rr,n}$, $u_{Rx,n}$	Acoustic displacement in region R, mode n, in the radial (r) or axial (x) direction
w	Perforate layer thickness
x, x_i, $\overline{x}$	Axial measurement or location
y_i	Experimental pressure measurements at location x_i

$y_{i,n}$	Amplitude coefficients which compose the eigenvector solution of the radial eigenvalue problem, n representing the mode number of the eigenvalue
$\Psi_{R,i}$	Integral weighting function in region R and set of mode numbers i
α_i	Analysis or optimization parameter
λ, λ_f	First Lamé parameter
μ	Second Lamé parameter (shear modulus)
ρ, ρ_i	Density
σ_b	Bladder sheet density
σ_s	Standard deviation
$\tau_{r,n}$, $\tau_{x,n}$, $\tau_{rx,n}$	Stress for mode n in the radial (r) or axial (x) direction; or shear stress in the rx plane
φ, φ_f	Scalar displacement potential
$\vec{\psi}$	Vector displacement potential
ω	Frequency (in radians/s)

SUMMARY

Syntactic foams—composite materials consisting of hollow particles embedded in a host matrix—have many applications for manufactured products, including weight reduction, thermal insulation, and noise reduction. In this thesis, a certain variety of syntactic foam is investigated with regards to reducing fluid borne noise in hydraulic systems. Such a foam maintains stiffness at low hydrostatic pressures and becomes compressible as pressure increases. With this compressibility, the foam is potentially useful as a liner for a reactive noise control device, much like compressed gas style devices currently in use; but the syntactic foam additionally adds significant damping to the system. In order to predict device performance, a linear multimodal model is developed of a hydraulic suppressor, constructed as an expansion chamber lined with a syntactic foam insert. Material models are developed for various compositions of the foam liners, based on an inverse analysis matching the model to experimental results. Two model simplifications are considered, and it is found that a simplified bulk modulus model gives sufficiently accurate results to make approximate predictions of suppressor performance. Several optimizations are performed to predict the optimal material composition for hydraulic excavator work cycles. To help compare the prototype suppressor against commercially available bladder style suppressors, a model is developed for the bladder style silencer and is validated experimentally. Overall, this work both demonstrates the current and potential utility of syntactic foam as a device lining material, and contributes new models to the hydraulics noise control community.

CHAPTER 1

INTRODUCTION

1.1 Motivation

Hydraulic systems are used in many high power applications, including many types of stationary and mobile machinery. However, such systems are typically noisy. This noise may have many sources, including mechanical impacts, diesel engines for many applications, hydraulic pumps and motors, and valves or other actuating devices. In these latter examples, much of the noise generated is transmitted directly into the hydraulic fluid. This fluid-borne noise is often characterized in industry as pressure ripple or flow ripple. Fluid-borne noise can be detrimental to a hydraulic system in several ways. It may couple to the mechanical structure, causing leakage, structural vibration, and airborne noise. The fluid and structure borne noise can increase the fatigue loading on components, thus increasing the probability of component failure, and the flow ripple at an actuator location can cause decreased actuator precision. Additionally, airborne noise, besides being an annoyance, can interfere with communication and even contribute to hearing loss if left unchecked. It is therefore beneficial to reduce fluid-borne noise in the system.

In air ducting applications, both reactive and dissipative elements are commonly installed to reduce fluid-borne noise in the system. When a liquid such as hydraulic fluid is the fluid medium, however, air ducting solutions become problematic due to the much higher sound speed in the fluid. The effectiveness of reactive and dissipative elements are dependent on component size relative to a wavelength, so to keep component size small,

hydraulic noise suppression devices introduce compressibility or compliance to lower the effective sound speed. This effect is usually produced either by introducing a compressed nitrogen volume, separated from the hydraulic fluid by a rubber bladder, or by routing the fluid through a hose, the outer walls of which are somewhat more compliant than metal hydraulic pipes. However, the compliance of hoses is limited by the need to contain the working pressure; also, breakout noise increases with hose wall compliance. Bladder style suppressors have been successfully employed in industry, but they suffer from the need for maintenance of the bladder nitrogen charge, and also require a considerable amount of machining to produce. Thus, if a syntactic foam is developed which is simpler to manufacture and requires reduced maintenance compared to the bladder style suppressor, considerable reductions could be achieved for both production and operating costs.

1.2 Objectives

It is hypothesized that syntactic foam can be an effective liner for various hydraulic noise suppression technologies. To begin validating this hypothesis, a model is developed of an in-line suppressor, assuming known properties of the liner. Viscoelastic properties are determined for various liner materials, based on an inverse analysis using experimental transmission loss data, as well as available independent data. A sensitivity study is performed on the estimates found from inverse analysis, to help determine reliability of the results. Additionally, material parameters are optimized for transmission loss in a certain hydraulic application. A model is also developed for a commercially available bladder style suppressor, against which current and future syntactic foam lined devices can be compared. The validation for the prototype and commercial in-line noise

suppressors is supported by experimental data, and certain model simplifications are examined for the various models once they are validated.

1.3 Organization

This thesis is organized as follows. Chapter 1 briefly introduces the work to be presented. Chapter 2 provides a literature review to provide background information on the work. This includes information on device modeling as well as syntactic foams, and it concludes with more specific contextual information for the models presented in later chapters. Chapter 3 presents the experimental apparatus, as well as some information regarding analysis and filtering of raw experimental data. In Chapter 4, the main model for the prototype hydraulic noise suppressor is presented and validated for one particular type of liner. Chapter 5 analyzes several more prototype liners, using both the material property estimation method used in Chapter 4, as well as composition data and experimental compression tests on the liners. In Chapter 6, model simplifications are considered, and a theoretical optimal liner material is determined based on the noise and pressure profile for a hydraulic system. Chapter 7 considers the performance of compressed gas style commercial in-line suppressors, including the development of a multimodal model for these devices. Commercial device performance is also briefly compared to the optimized prototype device as developed in Chapter 6. Finally, Chapter 8 presents a closing summary, along with conclusions and ideas for future work.

CHAPTER 2

BACKGROUND AND LITERATURE REVIEW

This chapter provides background information and a review of relevant literature concerning the current study. First, noise control is discussed with regards to hydraulic systems. Typical hydraulic noise control devices are described, and models of different types of devices are explored. Next, viscoelastic materials are introduced, with a discussion of their properties and current techniques for determining viscoelastic material properties. Syntactic foams are then introduced, with current and potential uses for hydraulic noise control. Finally, the present work is described in this the context of this literature review.

2.1 Noise control in hydraulic systems

2.1.1 Hydraulic noise control devices

While a variety of passive methods are available to reduce fluid-borne noise in hydraulic systems, a common element is the addition of system compliance. Without added compliance, the high bulk modulus of hydraulic fluid allows the system to react very quickly to changes in inputs, resulting in high speed control and high mechanical efficiencies. However, a tradeoff is that any fluid-borne noise in the system, often characterized as either pressure ripple or flow ripple, is also communicated very efficiently throughout the system, possibly resulting in problems such as reduced actuator precision, excessive fatigue loading, leakage, and unwanted structural vibrations. To reduce fluid-borne noise, compliance can be added to the system circuit using a variety of different methods.

Different sources of compliance can have markedly different effects on system performance. Entrained air in the hydraulic fluid adds compliance but is undesirable because it can cause unpredictable performance, and may cause additional problems as it separates from the fluid. However, it can be desirable to add a compliant device such as a side branch accumulator or an in-line suppressor very near to the noise source of interest, often a hydraulic pump. Accumulators consist of a large compressed gas volume, contained in a side branch device and separated from the hydraulic fluid by either a rubber bladder or a piston. They are considered to be low-pass noise filters, and are often used for various roles, including as energy storage, oil storage, or shock reduction devices. In-line devices similarly include a compressed gas volume, separated from the hydraulic fluid by a rubber bladder. They are marketed specifically for broadband noise reduction. Little research is found regarding these compressed gas style noise reduction devices. Transient response of an accumulator for water hammer reduction is studied by Rabie[1]. Numerous patents[2-11] have been filed for in-line hydraulic silencing devices. Often called suppressors or attenuators, these devices utilize either compressed gas or a solid or foam liner, but only a particular bladder style device[8] has been found to be commercially available. The manufacturer of this in-line suppressor has shown some experimental time-domain data in a conference publication[12], but the available data are not very useful for the prediction of general device performance; in fact, no frequency domain models of any sort have been uncovered. However, geometrically similar in-line silencers for airflow applications are extensively studied in research literature and are considered more extensively in the next section.

Besides the aforementioned high compliance devices, hoses and tuners are also commonly used for noise reduction. Hoses, due to their wall compliance and viscoelasticity, can be used to provide reactive and dissipative noise control to a hydraulic system. Their flexibility also allows them to decouple structural vibrations between their connection points. However, hoses are generally employed as flexible ducts, with noise reduction being a secondary consideration. In contrast, tuners are constructed of an outer hose, with an inner tube of varied composition, with plastic tubing and coiled or segmented metal being the usual options. The device functions in principle roughly like a harmonic resonator, although since it usually involves many flow paths, its actual performance can be quite complex. Like the in-line suppressor, tuners are used explicitly for noise control. Some research is available regarding hoses and tuners for noise control, and is explored in a following section.

2.1.2 In-line silencer/suppressor models

As mentioned above, many in-line hydraulic noise suppression devices have been designed and patented, but only a certain bladder style device is currently commercially produced, and no analytical models are available for any such devices. Nevertheless, a considerable amount of literature has been produced studying cylindrical lined silencers for airflow applications. These silencers, rather than employing high compliance, have a highly dissipative liner made of a fibrous or porous material. While the models vary somewhat in detail, important elements may include a perforate layer between the main flow path and the liner, extension of the inlet and outlet pipes into the expansion area, and mean flow effects in both the central flow path and the porous or fibrous liner.

For the commonly studied example of a cylindrical, radially symmetric device, a number of models have been developed in which a radial eigenvalue problem is solved to find a number of radial modes, and modal amplitudes are found by applying boundary or continuity conditions at a number of axial boundaries. In general, the various field quantities G_f are of the form

$$G_f = \left(A_1 J_m\left(k_r r\right) + A_2 Y_m\left(k_r r\right)\right)\left(A_3 e^{ik_x x} + A_4 e^{-ik_x x}\right) e^{i\omega t}, \tag{2.1}$$

for axial and radial coordinates x and r (see Blackstock[13] chapter 11, p. 389). Radial and axial wavenumbers k_r and k_x, relate to k by

$$k^2 = k_r^2 + k_x^2. \tag{2.2}$$

Complex amplitude coefficients A_1 through A_4 are determined for each region into which the model is divided. J_m and Y_m are Bessel functions of the first and second kind of order m, where $m = 0$ for pressure, normal stress, and axial displacement or velocity, and $m = 1$ for shear stress and radial displacement or velocity. A relatively simple model is demonstrated by Xu *et al*.[14], who study the effects of liner thickness and resistivity. Peat[15] demonstrates the theoretical derivation of a transfer matrix for an in-line silencer. In air silencers, the flow Mach number is often high enough to affect silencer performance, since the axial sound speed, and thus the axial wavenumbers, for the forward and reverse travelling waves are influenced by mean flow and are no longer identical. Cummings and Chang[16] examine mean flow in the liner section; Kirby and Denia[17] study the impact of high Mach flow numbers. Other studies focus on approximations for low frequencies[15, 18]. A study by Nennig *et al*.[19] expands this body of work by considering multiple wave propagation types in the poroelastic liner of a silencer. More complex geometry can be considered by explicitly examining the effects

of a perforated annulus[20]. The perforated annulus is modeled as an impedance layer in this type of analysis; and although theoretical models have been developed, such as in chapter 9 of Bies and Hansen[21], the published silencer models have instead relied on experimental impedance studies[22], some of which include the effects of grazing flow[23] or resistive backing materials[24, 25]. Several studies have examined silencers with both perforate layers and inlet/outlet extensions as well[26-28]. Panigrahi and Munjal give a brief overview of some of the varying levels of model complexity[29]. In addition to analytical models, some finite element and boundary element models of these silencers have been developed[26, 27, 30, 31], often in conjunction with analytical solutions.

2.1.3 Hose and tuner acoustic models

Hoses are found in a wide range of hydraulic devices. Because of their flexibility, they allow for easy connections between misaligned or moving components. They have the additional benefit of partially decoupling components such that propagation of structural vibration and fluid pressure ripple is reduced. One typical area of installation is at the outlet of a hydraulic pump. Hydraulic pumps are a major source of both vibration and pressure ripple in hydraulic systems. While both types of excitation can cause unwanted noise in the rest of the system, Longmore and Schlesinger have shown that for a typical pump and hose, the pressure ripple is a significantly more important source than pump vibration, and thus requires significantly more attenuation[32].

In order to reduce the size of noise control components for fluid power systems, compliant boundaries are exploited to reduce the effective sound speed in the device. Klees used this principle in his patent for an attenuating device[33], which is now

commonly referred to as a tuned cable or tuning coil, and has been modeled simply as a concentric version of a side-branch resonator by Hastings and Chen[34]. More complex models take into account additional factors such as fluid leakage along the hose insert[35, 36].

A number of models have been introduced for straight hoses which approximate the hose influence as a reduction in sound speed propagation, considering only a plane wave propagation mode[37-39]. Munjal and Thawani[37, 40], using isotropic hose models, have examined the tradeoff between fluid-borne noise reduction (axial transmission within the fluid) and breakout noise (transverse transmission into the environment), noting that overall noise control is generally limited by fluid-borne noise at lower frequencies, and by breakout noise at higher frequencies. Recent models have incorporated the anisotropy of the hose construction method, modeling two modes of propagation[35, 41]. A significant shortcoming of all these theoretical modeling techniques is that experimental testing is required to determine the properties for each hose. Several approaches are used to model these properties. Yu and Kojima[41, 42] characterize the viscoelasticity of hoses as a series of two Kelvin-Voight elements, while Johnston et al.[43], based on the Drew et al. model[35], determine frequency-independent viscoelastic properties of a wide variety of hoses, for a certain frequency band of interest. This latter model is also supported by experimental findings of almost constant complex amplitude of axial unit stiffness, which according to Longmore et al.[44] would require a large number of Kelvin-Voight elements to approximate theoretically.

2.2 Viscoelastic materials

The syntactic foams described in this thesis are composed of viscoelastic materials, and thus display viscoelastic composite properties as well. Both temperature and pressure dependence are important in the composite material performance. A discussion of basic viscoelastic properties and measurement methods is followed by information specific to composites and syntactic foam specifically.

2.2.1 Basic properties

It is commonly known that, all other things being equal, viscoelastic materials change behavior based on their temperature. At low temperatures they are characterized as glassy; as temperature increases, they enter a rubbery region, followed by rubbery flow and liquid flow[45]. In order to account for the energy dissipated when the material is deformed, an elastic modulus, such as Young's modulus *E*, will be described in terms of a storage modulus *E'* and a loss modulus *E''* by the relations

$$E = E' + iE'', \tag{2.3}$$

$$E'' = E' \tan\delta, \tag{2.4}$$

where δ is the phase angle between stress and strain, and tan δ is known as the loss factor[45]. A high loss factor is often desirable for noise and vibration control, and it is found that the loss factor has a maximum in the temperature region where the material changes from glassy to rubbery, known as the glass transition region; this region corresponds to a rapid change in the storage modulus as well[46]. This region may be characterized by a single glass transition temperature T_g, above which most amorphous materials become fluid, and above which thermoset polymers become elastomers[47]. Importantly, the properties including T_g are also dependent on the excitation strain rate or

frequency in a predictable manner. For example, consider a curve in which an elastic modulus is plotted versus frequency at a specified temperature. For a curve found at temperature T_1, the frequency axis can be shifted to match the curve of reference temperature T_0 using the equation

$$\log a_T = \frac{-b_1 (T_1 - T_0)}{b_2 + T_1 - T_0}, \tag{2.5}$$

where b_1 and b_2 are material constants and a_T is the shift factor, which is the ratio of the shifted frequency to a reference frequency[46, 48]. Practically speaking, this means that temperature and excitation frequency have inverse effects on the material properties. In addition, pressure also influences properties including T_g[49].

2.2.2 Property measurement

Polymers and polymer composites exhibit complex behavior versus variation in temperature, frequency, and pressure. For this reason it is both difficult and desirable to characterize their behavior so that they can be efficiently used in an application. Static Young's modulus[50] and Poisson's ratio[51] can be extracted from compressive and tensile tests, but two complex, frequency-dependent (often called dynamic) parameters are needed to characterize the material for acoustic or vibration purposes. In order to find one or two complex dynamic moduli simultaneously, a vibration excitation is applied to a sample, and the vibration response is measured. Simple versions of this method are applied by Capps[46] and Buchanan[52] to obtain only a Young's modulus of a rod sample; and Buchanan also introduces frequency dependent error estimates. A similar method is introduced by Willis et al.[53] in which measurement of both bulk and shear moduli are obtained using finite element analysis to solve an inverse problem based on

experimental measurements. Because of their experimental nature, these measurement techniques are applicable to both pure polymers and syntactic foam composites on a macroscopic scale.

2.2.3 Syntactic foams

Although the properties of composites can be measured, it is much more beneficial to have models to predict material behavior. A simple way to estimate composite properties of a syntactic foam is to take the average of the matrix material and effective values of the embedded microballoons, weighted by volume fraction; for example, Sajo[54] uses this method to find effective compressibility. More complex analytical models are used by Marur[55] and Tagliavia et al.[56] to find two elastic properties; and Baird et al.[57] extend to air-filled microsphere composites several previous methods to determine properties based on wave scattering methods. Finite element methods[55, 58] have also been employed to determine the composite properties. All of these models assume that the "bulk" elastic properties of the microballoons is known; this obviously cannot be measured directly by the usual bulk material tests, so it is either presented as an assumed value or estimated based on experimental data. Yuan and Lu[59] also provide an equation to estimate the microballoon properties based on the microballoon wall material properties and the contained air volume. In addition to properties based on composition, it is noted that the matrix material, and therefore the composite, will have a dependence on temperature and pressure as well. Song et al.[60] study temperature effects on a particular syntactic foam and develop a phenomenological model based on their results. Gaunaurd et al.[61] perform a numerical study of pressure effects on a voided polymer without microballoons, and Questad et al.[49] study the

relations of pressure, volume, and temperature both analytically and experimentally for a plain elastomer. In addition, the temperature-frequency relation in Equation (2.5) may be employed to add a temperature dependence to the previous models.

In addition to quantitative analyses, it is also desirable to qualitatively know how changing material composition affects material properties of the composite. In this regard, it can be said that the addition of microballoons affects the elastic modulus and strength of the host matrix, depending on the microballoon volume fraction and wall thickness[62, 63]; Sankaran et al.[64] note that for three phase syntactic foams, the addition of microballoons can also shift the glass transition temperature. Recent research regarding syntactic foams has also addressed functional gradients and the addition of nanoparticles. A study by Gupta and Ricci[65] indicates that changing microballoon wall thickness throughout the composite is preferable to changing microballoon volume fraction when creating a gradient. In addition, Rongong et al.[66] show that the addition of nanoparticles to syntactic foams can also alter the glass transition temperature. Finally, a study by Trivett et al.[67] concerning polymer microspheres in castor oil notes that the microspheres will buckle reversibly at a critical pressure P_{cr}; thus, above P_{cr}, they act roughly as air bubbles with relatively low stiffness; while below P_{cr}, they are stiffer. It is thus conceivable that polymer microspheres could be used to tailor the stiffness of a syntactic foam such that stiffness is reduced above a specified P_{cr}.

2.2.4 Syntactic foam in hydraulic silencing

Very little is found in the literature regarding syntactic foam for hydraulic noise control. Wheeler and Frentzos[68] have been awarded a patent for an in-line silencing device, and DiRe[69] has patented a pump outlet insert, both of which use syntactic

foams. However, like for the suppressors and attenuators mentioned in a previous section, no studies were found regarding performance of these devices. Also, these devices did not employ polymer microspheres like those which have been found to reversibly buckle. Thus, syntactic foams utilizing polymer microspheres are found to be a promising material to develop as a liner for silencing applications. Such liners are developed and analyzed for prototype in-line suppressors in this work.

2.3 This work in context

While the previous sections have described the background against which this work is performed, this section explains how the present work differs from and adds to previous knowledge and methods. Below, the syntactic foam lined suppressor is placed into context, as well as the models for the prototype suppressors, syntactic foam liners, and commercial suppressors.

2.3.1 Compliant-liner devices

The potential benefits of a compliant-liner noise suppression device over other technologies are many; this is suggested by the large number of patents for these devices. However, the absence of all but one of these devices from the marketplace suggests that practical implementation may be difficult, such that further development is needed, including this present work. Commentary on the difficulties in designing and modeling the devices is left to the later chapters, but some of the benefits over noise reduction methods such as hoses and tuners are discussed here.

There are several general advantages to compliant-liner devices. First, since the liner is not structural, it can be much more compliant than the hoses or hose sections of tuning coils which must also effectively contain the working pressure. Second, unlike

hoses, the liner does not have direct contact with the air in the external environment; a device with an approximately rigid outer shell and compliant lined interior is thus much less susceptible to breakout noise. Thus, the compliant-liner device is expected to result in significantly less breakout noise than a hose, especially at higher frequencies[37]. Finally, if it is assumed that some length of hose is still present in the system, it is probable that structural vibrations are not significantly transmitted[32], so that the fluid-borne noise which is addressed by the device is the primary noise of interest.

The arguments in the paragraph above are applicable to both the prototype and commercial noise suppression devices; here, some of the potential advantages of the prototype over the commercial device are discussed. The main anticipated advantages of the syntactic foam lined device are maintenance and manufacturing. The commercial compressed gas device requires periodic maintenance to ensure that the gas precharge pressure is maintained. Additionally, it has a number of complex manufactured parts, which increases the cost of building the device. The prototype device, in contrast, requires no complex metal parts; it consists solely of the external shell and the foam liner. Additionally, the liner requires no regular maintenance. Thus, the prototype device's reduced complexity and maintenance requirements may make it more economically advantageous. Other potential advantages are the ability to manufacture different liners using the same outer shell, with the different liners being engineered to have a wide range of performance characteristics. As discussed in later chapters, potential transmission loss performance of the syntactic foam devices appears to be favorable compared to the compressed gas devices as well. One potential drawback of the new device is the lifetime and degradation of the liners, which has not yet been studied.

2.3.2 Suppressor models

The models for the prototype and commercial suppressors, while sharing many basic elements with each other and with air silencer models, each present their own challenges and unique features. Both models presented here are simplified somewhat compared to the air models. First, the liners in both cases are impenetrable by the hydraulic fluid, so any flow in the liners can be ignored. Second, the mean hydraulic fluid flow can be ignored, since the flow Mach number is negligibly small due to the high speed of sound in hydraulic fluid versus air. However, several additional complications must be addressed.

In the prototype model, the nonlinear liner compression must be addressed, along with the propagation of shear as well as longitudinal waves in the liner. The liner compression not only needs to be determined in some manner, but it also changes the liner density and creates small flow gaps which must be modeled. As none of the previous models have addressed such problems, this constitutes a new development in device modeling. Additionally, the liner supports shear waves; of the presented models, only Nennig et al.[19] consider shear, and the Biot model they use is not appropriate to the prototype liner material. Specifically, the Nennig et al. model couples the liner motion to the motion of fluid within the liner, which is not applicable to the present case, as the liner is non-porous; additionally, the weakening of boundary conditions and the use of an iterative mode-matching method as in their work has been shown to be inappropriate for the devices considered in the present work[70]. In addition to these considerations, temperature of the working fluid and liner is also an important consideration in device

performance. For the prototype model, temperature considerations are moved to the syntactic foam model, discussed in Section 2.3.3.

The model for the compressed gas style commercial suppressor addresses a different set of problems, including the rubber bladder layer, a perforate impedance layer, and the effects of temperature and precharge pressure on device effectiveness. With the exception of the perforate layer, none of these aspects have been addressed in the models cited previously. However, all studies of perforate impedance have relied on experimental values where air was the acoustic fluid, and are thus still inapplicable to the device using hydraulic fluid.

2.3.3 Syntactic foam liner model

While some models have been developed for syntactic foam properties, they tend to be limited to a very specific foam composition, and none addresses the possibility of buckling microspheres. The models developed for liners in this work are largely empirical, with some attention to easily measurable attributes or known data about the constituent parts.

CHAPTER 3

EXPERIMENTAL METHODS AND APPARATUS

Transmission loss data are experimentally obtained for both commercial and experimental deices in the following chapters. As the experimental method and apparatus are common to these various devices, they are presented here in their own chapter. The approach for determining and mitigating experimental error is also discussed.

3.1 Experimental setup and test method

Experimental measurements are taken on a test rig constructed according to ISO 15086-2[71]. Figure 1 shows a diagram of the test rig. Flow is supplied by a Sauer Danfoss H1 bidirectional 9-piston axial piston pump driven by a Siemens Simovert Masterdrive variable frequency drive (VFD) via a Siemens 60 HP variable-speed ac motor. The test section consists of a test device with a long section of pipe on its upstream and downstream sides. These pipes are instrumented with piezoelectric pressure transducers PCB model 101A06, at positions labeled x_1 to x_6. The signals are passed through signal conditioners PCB model 480B21 and 482A16 and digitized by a 24-bit, 8-channel National Instruments model 4472 data acquisition board. Samples are taken at 10800 samples/second for 5120 samples per sample record by a data acquisition system (DAQ) mounted in a PC. Transfer functions between the transducers are obtained by using 100 vector averaged sample records. $A_{1U,0}$ and $B_{1U,0}$ are the forward and reverse travelling plane wave amplitudes at the test suppressor's upstream port (x_U), and $A_{1D,0}$ and $B_{1D,0}$ are the forward and reverse wave amplitudes of the plane waves at the downstream port (x_D). The wave amplitude subscripts are consistent with, and more fully

explained in, subsequent chapters. A termination suppressor is mounted at the end of the downstream pipe to reduce noise contamination in the downstream section. Pressure is developed using a Parker F1220S flow control valve downstream of the test section. An open Parker N820S flow control needle valve is placed upstream of the test section to generate broadband noise excitation. Hydraulic fluid temperatures at the entrance of the rig and at the inner radius of the component under test are measured with K type thermocouples, calibrated with an Omega CL3512A thermocouple calibrator and read by a National Instruments 9211A thermocouple reader. The upstream and downstream pipes have inner diameters of 0.0191 m (0.75 in), and the pressure transducers are mounted flush to the internal pipe walls, at positions relative to x_U and x_D as indicated in Table 1. Static pressure transducers are mounted immediately upstream and downstream of the test device; pressure drop for the test devices is generally found to be within the 70 kPa (10 psi) resolution of these sensors, which is a minor fraction of the overall system pressure.

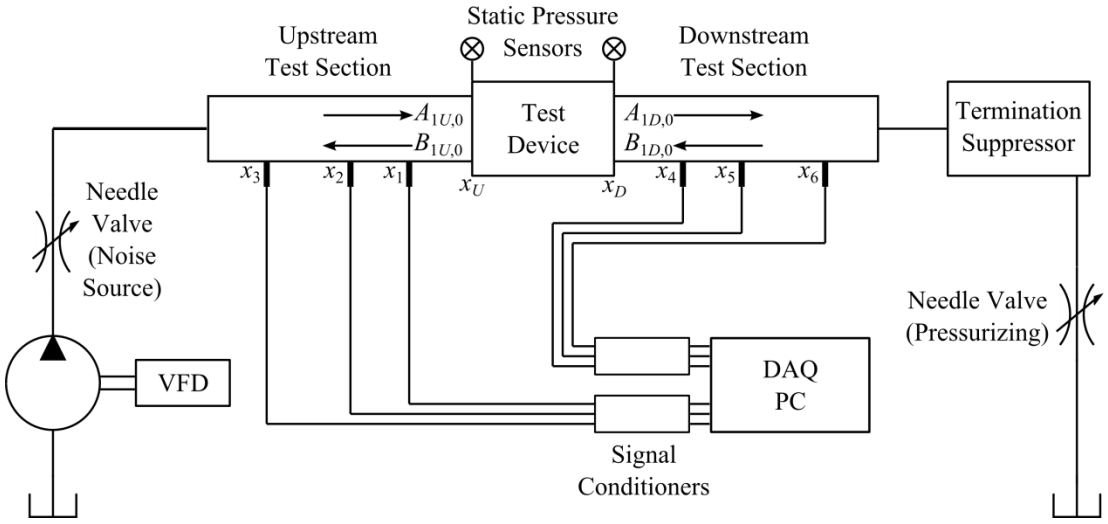

Figure 1: Schematic of test setup for measurement of fluid acoustic properties of a suppressor under test.

Table 1: Dynamic pressure transducer positions

Measurement	Value (m)
x_U-x_1	0.37
x_U-x_2	0.70
x_U-x_3	1.17
x_4-x_D	0.37
x_5-x_D	0.70
x_6-x_D	1.17

3.2 Data analysis

In order to determine a transfer matrix for the device under test, the complex wave amplitudes $A_{1U,0}$, $B_{1U,0}$, $A_{1D,0}$, and $B_{1D,0}$, shown in Figure 1, must be determined. Based on the given pipe radius and a sound speed in hydraulic fluid of around 1400 m s^{-1}, the first cutoff frequency (see chapter 10 of Blackstock [13]) in the instrumented pipes is about 43 kHz, far above the frequencies of interest for this work (below 5000 Hz). Additionally, the pressure transducers are far from any discontinuities, so evanescent waves at the transducer locations are negligible, and theoretically only the plane wave amplitudes will be measured. Wave amplitudes on each side of the test device are found using a multi-point method with three sensors[72], which avoids a half-wavelength indeterminacy that is present with only two sensors. Transfer functions are used to compare the pressure between each sensors, eliminating the need for absolute calibration.

The plane wave propagation assumption for experimental data is represented by the mathematical model

$$\bar{Y}_U = \mathbf{E}_U \begin{bmatrix} A_{1U,0} \\ B_{1U,0} \end{bmatrix}, \bar{Y}_D = \mathbf{E}_D \begin{bmatrix} A_{1D,0} \\ B_{1D,0} \end{bmatrix}, \tag{3.1}$$

$$\bar{Y}_U = \begin{bmatrix} y_1 \\ y_2 \\ y_3 \end{bmatrix}, \bar{Y}_D = \begin{bmatrix} y_4 \\ y_5 \\ y_6 \end{bmatrix}, \tag{3.2}$$

$$\mathbf{E}_U = \begin{bmatrix} e^{ik(x_U - x_1)} & e^{-ik(x_U - x_1)} \\ e^{ik(x_U - x_2)} & e^{-ik(x_U - x_2)} \\ e^{ik(x_U - x_3)} & e^{-ik(x_U - x_3)} \end{bmatrix}, \mathbf{E}_D = \begin{bmatrix} e^{ik(x_4 - x_D)} & e^{-ik(x_4 - x_D)} \\ e^{ik(x_5 - x_D)} & e^{-ik(x_5 - x_D)} \\ e^{ik(x_6 - x_D)} & e^{-ik(x_6 - x_D)} \end{bmatrix}. \tag{3.3}$$

Here y_1 through y_6 represent the complex pressure amplitude measurements taken at locations x_1 through x_6, and normalized by y_1. Wave amplitudes are found using the pseudoinverse function,

$$\begin{bmatrix} A_{1U,0} \\ B_{1U,0} \end{bmatrix} = \text{pinv}(\mathbf{E}_U)\bar{Y}_U, \begin{bmatrix} A_{1D,0} \\ B_{1D,0} \end{bmatrix} = \text{pinv}(\mathbf{E}_D)\bar{Y}_D, \tag{3.4}$$

which gives a least-squares approximation of the wave amplitudes. This is also discussed by Earnhart et al.[73]

Acoustic pressure p_1 and volume velocity Q_1 at the upstream port, and likewise p_2 and Q_2 at the downstream port, can be calculated from the wave amplitudes using the equations

$$\begin{aligned} p_1 &= A_{1U,0} + B_{1U,0} \quad & p_2 &= A_{1D,0} + B_{1D,0} \\ Q_1 &= \frac{A_{1U,0} - B_{1U,0}}{Z_0} \quad & Q_2 &= \frac{A_{1D,0} - B_{1D,0}}{Z_0} \end{aligned}, \tag{3.5}$$

where

$$Z_0 = \frac{\rho_f c_f}{\pi r_0^2} \tag{3.6}$$

is the acoustic impedance, ρ_f is the density of the fluid, c_f is the speed of sound in the fluid, and r_0 is the inner radius of the pipe.

Acoustic pressures and volume velocities at the suppressor ports are related by a transfer matrix with elements t_{ij},

$$\begin{bmatrix} p_1 \\ Q_1 \end{bmatrix} = \begin{bmatrix} t_{11} & t_{12} \\ t_{21} & t_{22} \end{bmatrix} \begin{bmatrix} p_2 \\ Q_2 \end{bmatrix}. \tag{3.7}$$

It is assumed that the test suppressor is geometrically symmetric end to end, and that the system is assumed to be reciprocal, resulting in

$$t_{11} = t_{22},\ t_{21} = \frac{1+t_{11}^2}{t_{12}}. \tag{3.8}$$

Thus, once acoustic pressures and volume velocities are calculated, the transfer matrix elements can thus be solved by combining Equations (3.7) and (3.8). Specifically,

$$t_{11} = t_{22} = \frac{p_1 Q_1 + p_2 Q_2}{p_1 Q_2 + p_2 Q_1} \tag{3.9}$$

$$t_{12} = \frac{p_1^2 - p_2^2}{p_1 Q_2 + p_2 Q_1} \tag{3.10}$$

$$t_{21} = \frac{Q_1^2 - Q_2^2}{p_1 Q_2 + p_2 Q_1} \tag{3.11}$$

While the transfer matrix model is useful for system modeling, it is desirable to have a single value metric to compare devices at various frequencies or noise spectra. The anechoic transmission loss (TL) is used in this work, and can be found experimentally using the equation

$$\mathrm{TL} = 20\log_{10}\frac{1}{2}\left|t_{11} + \frac{t_{12}}{Z_0} + Z_0 t_{21} + t_{22}\right|. \tag{3.12}$$

Substituting the port wave amplitudes using Equations (3.5) through (3.8) yields the new TL equation

$$\mathrm{TL}=20\log_{10}\left|\frac{A_{1U,0}^2 - B_{1D,0}^2}{A_{1U,0}A_{1D,0} - B_{1U,0}B_{1D,0}}\right|. \tag{3.13}$$

In the case of an anechoic experiment $B_{1D,0} = 0$, the TL equation reduces to the ratio of incident to transmitted pressure amplitude:

$$\mathrm{TL}_{\mathrm{anechoic}} = 20\log_{10}\left|\frac{A_{1U,0}}{A_{1D,0}}\right|. \tag{3.14}$$

Regardless of experimental conditions, Equations (3.13) and (3.14) theoretically produce the same TL results for a device with a given transfer matrix.

3.3 Artifacts and data filtering

Several filters are applied to ensure the integrity of experimentally obtained data. The ISO standard[71] calls for the removal of very low frequencies, and any data with coherence below 0.95. While this gives a significant improvement, very distinct artifacts still remain after this processing. An example set of data is shown in Figure 2, where severe spikes in the TL data can be seen around 550 and 950 Hz, and some less drastic roughness is observed at other frequencies, especially above about 1700 Hz. The source of such artifacts is still being investigated, but they are presently correlated with strong standing waves in the system; coherent noise (that is, alternate transmission modes) especially in the downstream test section; and a low signal-to-noise ratio, again especially downstream. To further improve the quality, it is found that additional data filtering can be applied by means of an experimental model error estimate (e_e).

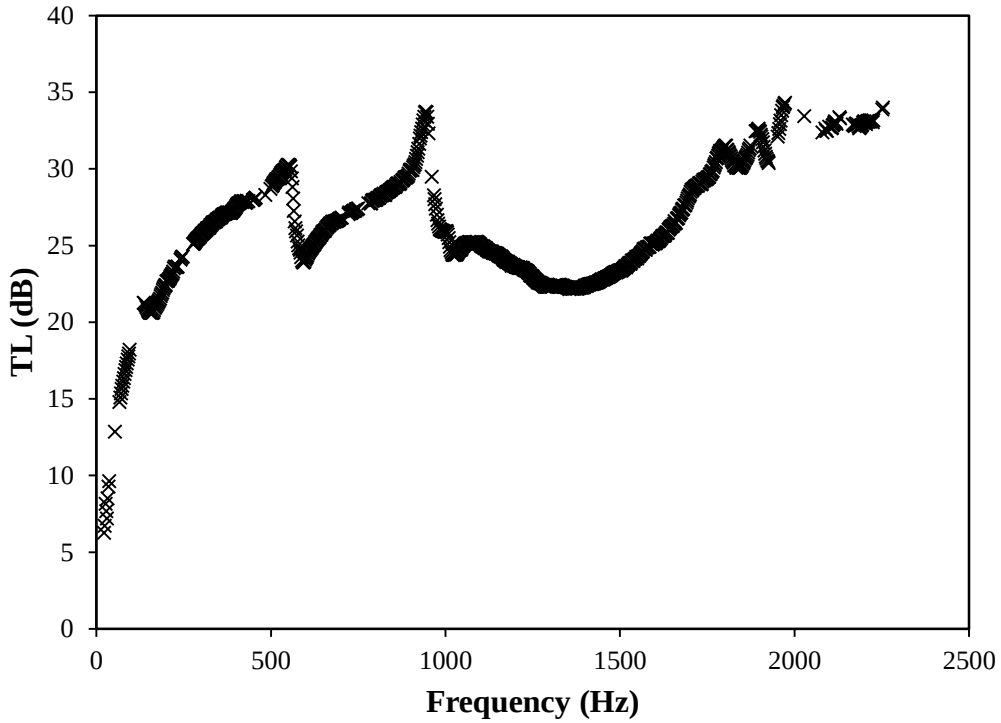

Figure 2: Transmission loss example for first prototype suppressor, 400 psi, ~35C, after frequency and coherence filtering.

To find this error estimate, the complex wave amplitudes must be found from Equation (3.4) and the corresponding experimental measurements y_i. A new set of "theoretical measurements" $\bar{Y}'_U$ and $\bar{Y}'_D$ with elements y'_i are introduced as

$$\bar{Y}'_U = \mathbf{E}_U \begin{bmatrix} A_{1U,0} \\ B_{1U,0} \end{bmatrix}, \bar{Y}'_D = \mathbf{E}_D \begin{bmatrix} A_{1D,0} \\ B_{1D,0} \end{bmatrix}, \tag{3.15}$$

where y'_i would be equal to y_i if experimental measurements corresponded exactly to the plane wave model presented in Equation (3.1). However, due to various sources of error,

$$\bar{Y}'_U \neq \bar{Y}_U, \bar{Y}'_D \neq \bar{Y}_D \tag{3.16}$$

in general. The extent to which the model measurements match the actual experimental measurements is thus an indicator of how much of the measured pressure is due to plane wave propagation. To get a single error value, the maximum is used to define e_e:

$$e_e = \max \left| \frac{y_i' - y_i}{y_i} \right|. \tag{3.17}$$

It is interesting to note that this error analysis is only possible because more measurements are taken than the number of unknown amplitude coefficients. Thus, a method which was introduced to reduce half-wavelength spacing errors proves to have additional utility in analyzing experimental error. The error estimate is illustrated in Figure 3, where it can be seen that the aforementioned TL spikes correspond to frequencies with a very high value of e_e; conversely, smooth portions of the graph have relatively lower error. Various e_e filters are applied in the following chapters for model validation and material property estimation purposes.

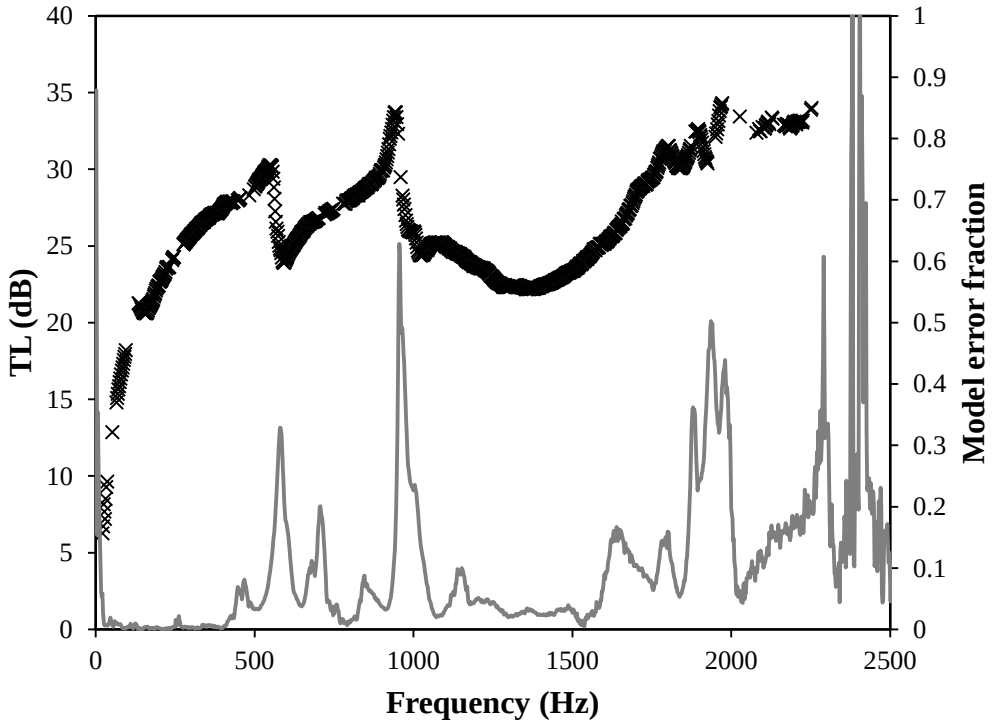

Figure 3: Transmission loss example from Figure 2 with calculated model error e_e plotted: × Experimental TL; ▬ Model error. Smooth TL regions tend to correspond to lower error.

In addition to the error estimate criterion shown above, TL artifacts have also been correlated[74] with the relation

$$\tan^{-1}\left|\frac{B_{1U,0}B_{1D,0}}{A_{1U,0}A_{1D,0}}\right| \approx 0\,. \tag{3.18}$$

This condition correlates to resonance behavior in the pipe sections, and flags artifacts with similar effectiveness to the e_e calculation. However, while the resonance correlation is informative, Equation (3.18) does not show a causal relationship to the artifacts, and is one step further removed from the raw data than Equation (3.17). Additionally, it flags some frequencies without apparent artifacts, thus serving as an insufficient criterion[74]. For these reasons, the e_e value is used exclusively for artifact filtering.

3.4 Compression tests

In addition to transmission loss testing, some tests were performed to experimentally determine the compression of various liners versus system pressure. For this test, the liner is placed in a close-fitting steel chamber with a viewport on one end which is large enough to determine the liner internal radius; the chamber is shown in Figure 4. Digital photographs at a series of increasing system pressures are then analyzed to determine the change in inner radius. Some error may be introduced when determining the size for each photograph, since the inner boundary may not appear perfectly circular in the photograph, and its exact boundaries may not be clear. Boundary uncertainty error appears to be limited to about 0.15 mm, or about 1% of initial radius, based on measurement scatter of relatively incompressible solid polymer samples. Size distortion due to liner motion after compression begins may also contribute to the total measurement error, as there are no measures to determine distance of the liner from the

viewing port. Model-based best-fit curves are used to reduce error in the analysis discussed in Chapter 5.

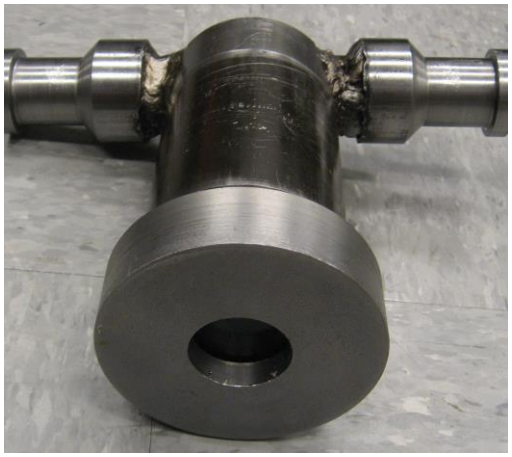

Figure 4: Pressure chamber with viewport, used for compression tests.

CHAPTER 4

ANALYSIS OF PROTOTYPE SYNTACTIC FOAM LINED SUPPRESSOR

In order to demonstrate the efficacy of syntactic foam liners in a hydraulic silencing device, the device itself must first be modeled. The model developed in this chapter is based on a multimodal expansion technique commonly used to model airflow silencers. The experimental validation of the model is made difficult by the lack of *a priori* knowledge of the liner material properties. Thus, estimated material properties and the device model are validated simultaneously using data from two different length devices. Additionally, a finite element model provides theoretical model validation, given assumed material properties.

4.1 Modeling

4.1.1 Suppressor Geometry

The pertinent geometry of the suppressor to be modeled is shown in Figure 5. It has an inlet port at $x = 0$ and an outlet port at $x = L_0$. The inlet and outlet pipes are of radius r_0. The expansion section may contain a liner material which, when the system is unpressurized, extends from radius a_0 to b_0 and has axial length L_0. When static pressure is applied, the liner compresses to radii a and b, and the length compresses to length L, forming axial gaps of width L_1 and L_2, and introducing new discontinuities at the planes $x = L_1$ and $x = L_0 - L_2$ as shown in the figure. This compressed geometry is then used for analysis at that pressure. For purposes of the present simulation, it is assumed that the liner stays axially centered. The liner material's elasticity is characterized by Lamé parameters λ and μ. In general the material properties of the liner will vary with static

pressure, so it would be inaccurate to calculate deformation based only on the pressurized values of λ and μ. For the theoretical development it will therefore be assumed that the compressed dimensions at a given operating pressure are known.

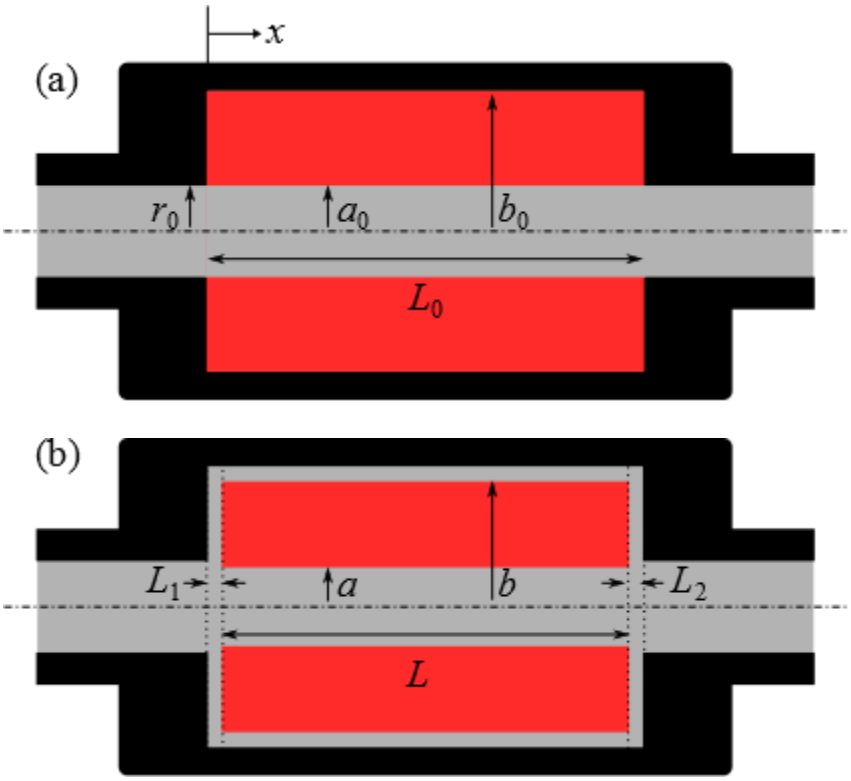

Figure 5: Geometry of silencer model. (a) The upstream and downstream pipes have radius r_0, and the expansion section has outer radius b_0 and length L_0, and is separated from the pipes by port planes $x = 0$ and $x = L_0$. The liner (red) extends from radius a_0 to b_0 along the whole expansion length. (b) When the system is pressurized, the liner compresses to radii a and b and length L. This leaves axial gaps of length L_1 and L_2 on the upstream and downstream ends of the silencer. The upstream and downstream end planes of the liner then become $x = L_1$ and $x = L_0 - L_2$.

4.1.2 Multimodal Model

The model developed in the following is based on a multimodal radial expansion of the waves in the fluid in all regions, as well as in the liner within region 2. In the fluid domain, the wave equation as a function of displacement potential φ_f is

$$\nabla^2 \varphi_f = \frac{1}{c_f^2} \ddot{\varphi}_f \,. \tag{4.1}$$

In the liner domain, scalar and vector displacement potentials φ and $\vec{\psi}$ conform to:

$$\nabla^2\varphi = \frac{1}{c_L^2}\ddot{\varphi}, \tag{4.2}$$

$$\nabla^2\vec{\psi} = \frac{1}{c_T^2}\ddot{\vec{\psi}}. \tag{4.3}$$

Sound speed c_f in the fluid, and longitudinal and shear wave sound speeds c_L and c_T in the liner are defined by:

$$c_f = \sqrt{\frac{\lambda_f}{\rho_f}}, \tag{4.4}$$

$$c_L = \sqrt{\frac{\lambda + 2\mu}{\rho_s}}, \tag{4.5}$$

$$c_T = \sqrt{\frac{\mu}{\rho_s}}, \tag{4.6}$$

where λ_f is the fluid bulk modulus, and ρ_f and ρ_s are fluid and liner densities. Wavenumbers k are defined in terms of acoustic frequency ω and sound speeds by

$$k_f = \frac{\omega}{c_f}, \quad k_L = \frac{\omega}{c_L}, \quad k_T = \frac{\omega}{c_T}. \tag{4.7}$$

As seen in Figure 6(a), the system is divided into five regions or sub-regions. Region 1 contains the inlet and outlet pipes; region 2 has the axial section of the silencer with the compressed liner; and region 3 contains the axial silencer gap sections where the compressed liner is not present. Regions 1 and 3 are further subdivided when needed to differentiate the upstream and downstream sections, and are marked with a U and D in this case. The planes at $x = 0$, $x = L_1$, $x = L + L_1$, and $x = L_0$ (see Figure 5(a)) separate the different regions. As partially illustrated in Figure 6(b), $A_{R,n}$ and $B_{R,n}$ represent the

complex amplitudes of the forward and reverse travelling waves of mode n in region R. These amplitudes are taken at the upstream (left) port defining each region, with the exception of $A_{1U,n}$ and $B_{1U,n}$, which are found at $x = 0$. The subscript n is an integer index for the radial modes of the forward and reverse travelling waves, and $n = 0$ corresponds to the lowest or plane wave mode.

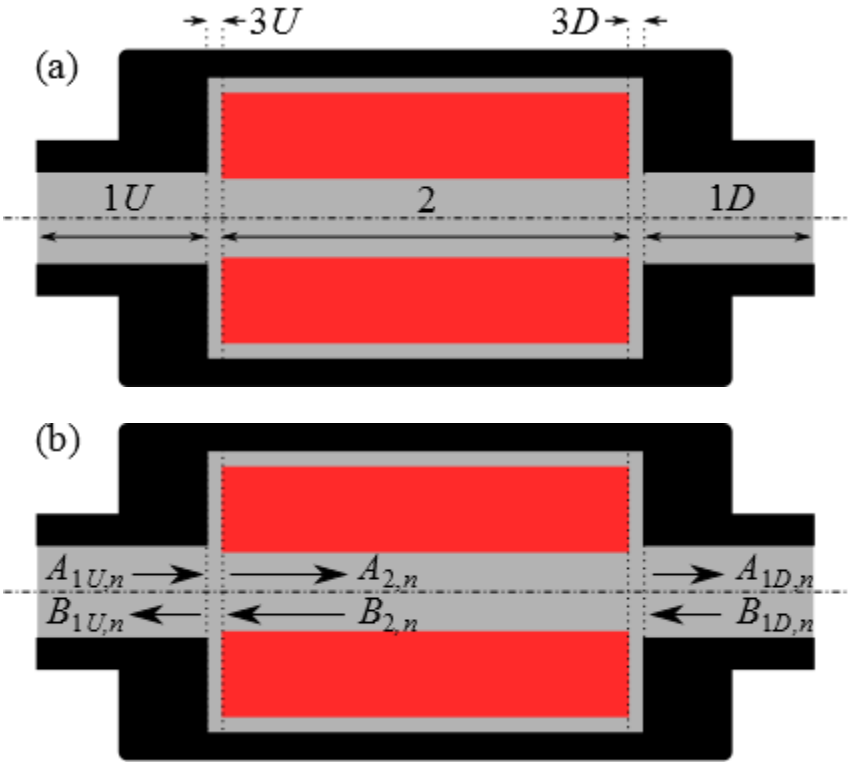

Figure 6: Silencer divided into five regions corresponding to different areas of radial geometry. Region 1 includes the inlet and outlet pipes, region 2 includes the lined section of the silencer, and region 3 contains the axial gaps. Regions 1 and 3 are further separated into upstream and downstream sections 1U, 1D, 3U, and 3D. For a given radial mode n, each region R contains upstream and downstream travelling waves of complex amplitude $A_{R,n}$ and $B_{R,n}$; these are labeled explicitly for region 1.

The acoustic pressure and displacement fields in each region are a function of modal amplitudes $A_{R,n}$ and $B_{R,n}$, each n of which corresponds to a different radial mode. These radial modes are characterized by axial wavenumbers $k_{Rx,n}$. Additionally, each axial wavenumber is related to radial wavenumbers $k_{Rrf,n}$ for fluid-borne waves, with

subscript *f* replaced by *L* or *T* for longitudinal or shear waves in the liner. The relations are:

$$k_f^2 = k_{Rx,n}^2 + k_{Rrf,n}^2, \tag{4.8}$$

$$k_L^2 = k_{Rx,n}^2 + k_{RrL,n}^2, \tag{4.9}$$

$$k_T^2 = k_{Rx,n}^2 + k_{RrT,n}^2, \tag{4.10}$$

with Equations (4.9) and (4.10) being applicable only in region 2.

The solutions to equations (4.1) through (4.3), given the radial symmetry of the system, are:

$$\varphi_f = \begin{cases} \left(J_0\left(k_{1rf,n}r\right)\right)\left(A_{1,n}\,\mathrm{e}^{-\mathrm{i}k_{1x,n}\bar{x}} + B_{1,n}\,\mathrm{e}^{\mathrm{i}k_{1x,n}\bar{x}}\right)\mathrm{e}^{\mathrm{i}\omega t}, \text{region 1} \\ \left(y_{1,n}J_0\left(k_{2rf,n}r\right)\right)\left(A_{2,n}\,\mathrm{e}^{-\mathrm{i}k_{2x,n}\bar{x}} + B_{2,n}\,\mathrm{e}^{\mathrm{i}k_{2x,n}\bar{x}}\right)\mathrm{e}^{\mathrm{i}\omega t}, \text{region 2, } r< a \\ \left(y_{6,n}J_0\left(k_{2rf,n}r\right) + y_{7,n}Y_0\left(k_{2rf,n}r\right)\right)\left(A_{2,n}\,\mathrm{e}^{-\mathrm{i}k_{2x,n}\bar{x}} + B_{2,n}\,\mathrm{e}^{\mathrm{i}k_{2x,n}\bar{x}}\right)\mathrm{e}^{\mathrm{i}\omega t}, \text{region 2, } r > b \\ \left(J_0\left(k_{3rf,n}r\right)\right)\left(A_{3,n}{}^{-\mathrm{i}k_{3x,n}\bar{x}} + B_{3,n}\,\mathrm{e}^{\mathrm{i}k_{3x,n}\bar{x}}\right)\mathrm{e}^{\mathrm{i}\omega t}, \text{region 3} \end{cases}, \tag{4.11}$$

$$\varphi = \left(y_{2,n}J_0\left(k_{2rL,n}r\right) + y_{3,n}Y_0\left(k_{2rL,n}r\right)\right)\left(A_{2,n}\,\mathrm{e}^{-\mathrm{i}k_{2x,n}\bar{x}} + B_{2,n}\,\mathrm{e}^{\mathrm{i}k_{2x,n}\bar{x}}\right)\mathrm{e}^{\mathrm{i}\omega t}, \tag{4.12}$$

$$\bar{\psi} = \left(y_{4,n}J_1\left(k_{2rT,n}r\right) + y_{5,n}Y_1\left(k_{2rT,n}r\right)\right)\left(A_{2,n}\,\mathrm{e}^{-\mathrm{i}k_{2x,n}\bar{x}} + B_{2,n}\,\mathrm{e}^{\mathrm{i}k_{2x,n}\bar{x}}\right)\mathrm{e}^{\mathrm{i}\omega t}\,\hat{e}_\theta, \tag{4.13}$$

$$\bar{x} = \begin{cases} x, & \text{region } 1U \\ x - L_0, & \text{region } 1D \\ x - L_1, & \text{region } 2 \\ x, & \text{region } 3U \\ x - L_1 - L, & \text{region } 3D \end{cases}, \tag{4.14}$$

where J_m and Y_m are the m^{th} order Bessel functions of the first and second kind. Complex coefficients $y_{1,n}$ through $y_{7,n}$ are found by applying radial boundary conditions as described below. Relations between the displacement potentials in Equations (4.11) through (4.13) and the acoustic stresses, pressures, and displacements in the system can

be derived using Chapter 2 of Achenbach's textbook[75]. In the fluid medium, for regions 1 and 3,

$$u_{r,n} = -k_{Rrf,n} J_1\left(k_{Rrf,n} r\right)\left(A_{R,n}\, \mathrm{e}^{-\mathrm{i}k_{Rx,n}\bar{x}} + B_{R,n}\, \mathrm{e}^{\mathrm{i}k_{Rx,n}\bar{x}}\right)\mathrm{e}^{\mathrm{i}\omega t}, \tag{4.15}$$

$$u_{x,n} = -\mathrm{i}k_{Rx,n} J_0\left(k_{Rrf,n} r\right)\left(A_{R,n}\, \mathrm{e}^{-\mathrm{i}k_{Rx,n}x} - B_{R,n}\, \mathrm{e}^{\mathrm{i}k_{Rx,n}\bar{x}}\right)\mathrm{e}^{\mathrm{i}\omega t}, \tag{4.16}$$

$$u_\theta = 0, \tag{4.17}$$

$$\tau_{r,n} = \tau_{x,n} = \tau_{\theta,n} = -k_f^2 \lambda_f J_0\left(k_{Rrf,n} r\right)\left(A_{R,n}\, \mathrm{e}^{-\mathrm{i}k_{Rx,n}\bar{x}} + B_{R,n}\, \mathrm{e}^{\mathrm{i}k_{Rx,n}\bar{x}}\right)\mathrm{e}^{\mathrm{i}\omega t}, \tag{4.18}$$

$$\tau_{rx,n} = \tau_{xr,n} = \tau_{r\theta,n} = \tau_{\theta r,n} = \tau_{x\theta,n} = \tau_{\theta x,n} = 0, \tag{4.19}$$

where R substitutes for the region number. For the fluid medium in region 2, where $r \le a$,

$$u_{r,n} = -k_{2rf,n} y_1 J_1\left(k_{2rf,n} r\right)\left(A_{2,n}\, \mathrm{e}^{-\mathrm{i}k_{2x,n}\bar{x}} + B_{2,n}\, \mathrm{e}^{\mathrm{i}k_{2x,n}\bar{x}}\right)\mathrm{e}^{\mathrm{i}\omega t}, \tag{4.20}$$

$$u_{x,n} = -\mathrm{i}k_{2x,n} y_1 J_0\left(k_{2rf,n} r\right)\left(A_{2,n}\, \mathrm{e}^{-\mathrm{i}k_{2x,n}\bar{x}} - B_{2,n}\, \mathrm{e}^{\mathrm{i}k_{2x,n}\bar{x}}\right)\mathrm{e}^{\mathrm{i}\omega t}, \tag{4.21}$$

$$u_{\theta,n} = 0, \tag{4.22}$$

$$\tau_{r,n} = \tau_{x,n} = \tau_{\theta,n} = -k_f^2 \lambda_f y_1 J_0\left(k_{2rf,n} r\right)\left(A_{2,n}\, \mathrm{e}^{-\mathrm{i}k_{2x,n}\bar{x}} + B_{2,n}\, \mathrm{e}^{\mathrm{i}k_{2x,n}\bar{x}}\right)\mathrm{e}^{\mathrm{i}\omega t}, \tag{4.23}$$

and where $b < r \le b_0$,

$$u_{r,n} = -k_{2rf,n}\left(y_6 J_1\left(k_{2rf,n} r\right) + y_7 Y_1\left(k_{2rf,n} r\right)\right)\left(A_{2,n}\, \mathrm{e}^{-\mathrm{i}k_{2x,n}\bar{x}} + B_{2,n}\, \mathrm{e}^{\mathrm{i}k_{2x,n}\bar{x}}\right)\mathrm{e}^{\mathrm{i}\omega t}, \tag{4.24}$$

$$u_{x,n} = -\mathrm{i}k_{2x,n}\left(y_6 J_0\left(k_{2rf,n} r\right) + y_7 Y_0\left(k_{2rf,n} r\right)\right)\left(A_{2,n}\, \mathrm{e}^{-\mathrm{i}k_{2x,n}\bar{x}} - B_{2,n}\, \mathrm{e}^{\mathrm{i}k_{2x,n}\bar{x}}\right)\mathrm{e}^{\mathrm{i}\omega t}, \tag{4.25}$$

$$u_\theta = 0 \tag{4.26}$$

$$\tau_{r,n} = \tau_{x,n} = \tau_{\theta,n} = -k_f^2 \lambda_f \left(y_6 J_0\left(k_{2rf,n} r\right) + y_7 Y_0\left(k_{2rf,n} r\right)\right)\left(A_{2,n}\, \mathrm{e}^{-\mathrm{i}k_{2x,n}\bar{x}} + B_{2,n}\, \mathrm{e}^{\mathrm{i}k_{2x,n}\bar{x}}\right)\mathrm{e}^{\mathrm{i}\omega t}. \tag{4.27}$$

In region 2 in the solid liner, $a < r \le b$,

$$u_{r,n} = -k_{2rL,n}\left(y_2 J_1\left(k_{2rL,n}r\right) + y_3 Y_1\left(k_{2rL,n}r\right)\right)\left(A_{2,n}\,\mathrm{e}^{-\mathrm{i}k_{2x,n}\bar{x}} + B_{2,n}\,\mathrm{e}^{\mathrm{i}k_{2x,n}\bar{x}}\right)\mathrm{e}^{\mathrm{i}\omega t}\ldots$$
$$+\mathrm{i}k_{2x,n}\left(y_4 J_1\left(k_{2rT,n}r\right) + y_5 Y_1\left(k_{2rT,n}r\right)\right)\left(A_{2,n}\,\mathrm{e}^{-\mathrm{i}k_{2x,n}\bar{x}} - B_{2,n}\,\mathrm{e}^{\mathrm{i}k_{2x,n}\bar{x}}\right)\mathrm{e}^{\mathrm{i}\omega t} \quad , \quad (4.28)$$

$$u_{x,n} = -\mathrm{i}k_{2x,n}\left(y_2 J_0\left(k_{2rL,n}r\right) + y_3 Y_0\left(k_{2rL,n}r\right)\right)\left(A_{2,n}\,\mathrm{e}^{-\mathrm{i}k_{2x,n}\bar{x}} - B_{2,n}\,\mathrm{e}^{\mathrm{i}k_{2x,n}\bar{x}}\right)\mathrm{e}^{\mathrm{i}\omega t}\ldots$$
$$+k_{2rT,n}\left(y_4 J_0\left(k_{2rT,n}r\right) + y_5 Y_0\left(k_{2rT,n}r\right)\right)\left(A_{2,n}\,\mathrm{e}^{-\mathrm{i}k_{2x,n}\bar{x}} + B_{2,n}\,\mathrm{e}^{\mathrm{i}k_{2x,n}\bar{x}}\right)\mathrm{e}^{\mathrm{i}\omega t} \quad , \quad (4.29)$$

$$u_{\theta,n} = 0\,, \quad (4.30)$$

$$\tau_{r,n} = \tau_{\lambda,n} + 2\mu\left(k_{2rL,n}^2\left(y_2\left(-J_0\left(k_{2rL,n}r\right) + \frac{J_1\left(k_{2rL,n}r\right)}{k_{2rL,n}r}\right)\ldots\right.\right.$$
$$+y_3\left(-Y_0\left(k_{2rL,n}r\right) + \frac{Y_1\left(k_{2rL,n}r\right)}{k_{2rL,n}r}\right)\left(A_{2,n}\,\mathrm{e}^{-\mathrm{i}k_{2x,n}\bar{x}} + B_{2,n}\,\mathrm{e}^{\mathrm{i}k_{2x,n}\bar{x}}\right)\mathrm{e}^{\mathrm{i}\omega t}\ldots$$
$$+\mathrm{i}k_{2rT,n}k_{2x,n}\left(y_4\left(J_0\left(k_{2rT,n}r\right) - \frac{J_1\left(k_{2rT,n}r\right)}{k_{2rT,n}r}\right)\ldots\right.$$
$$\left.\left.+y_5\left(Y_0\left(k_{2rT,n}r\right) - \frac{Y_1\left(k_{2rT,n}r\right)}{k_{2rT,n}r}\right)\right)\left(A_{2,n}\,\mathrm{e}^{-\mathrm{i}k_{2x,n}\bar{x}} - B_{2,n}\,\mathrm{e}^{\mathrm{i}k_{2x,n}\bar{x}}\right)\mathrm{e}^{\mathrm{i}\omega t}\right) \quad , \quad (4.31)$$

$$\tau_{x,n} = \tau_{\lambda,n} + 2\mu\left(-k_{2x,n}^2\left(y_2 J_0\left(k_{2rL,n}r\right) + y_3 Y_0\left(k_{2rL,n}r\right)\right)\left(A_{2,n}\,\mathrm{e}^{-\mathrm{i}k_{2x,n}\bar{x}} + B_{2,n}\,\mathrm{e}^{\mathrm{i}k_{2x,n}\bar{x}}\right)\mathrm{e}^{\mathrm{i}\omega t}\ldots\right.$$
$$\left.-\mathrm{i}k_{2rT,n}k_{2x,n}\left(y_4 J_0\left(k_{2rT,n}r\right) + y_5 Y_0\left(k_{2rT,n}r\right)\right)\left(A_{2,n}\,\mathrm{e}^{-\mathrm{i}k_{2x,n}\bar{x}} - B_{2,n}\,\mathrm{e}^{\mathrm{i}k_{2x,n}\bar{x}}\right)\mathrm{e}^{\mathrm{i}\omega t}\right) \quad , \quad (4.32)$$

$$\tau_{\theta,n} = \tau_{\lambda,n} + 2\mu\left(-\frac{k_{2rL,n}}{r}\left(y_2 J_1\left(k_{2rL,n}r\right) + y_3 Y_1\left(k_{2rL,n}r\right)\right)\left(A_{2,n}\,\mathrm{e}^{-\mathrm{i}k_{2x,n}\bar{x}} + B_{2,n}\,\mathrm{e}^{\mathrm{i}k_{2x,n}\bar{x}}\right)\mathrm{e}^{\mathrm{i}\omega t}\ldots\right.$$
$$\left.+\frac{\mathrm{i}k_{2x,n}}{r}\left(y_4 J_1\left(k_{2rT,n}r\right) + y_5 Y_1\left(k_{2rT,n}r\right)\right)\left(A_{2,n}\,\mathrm{e}^{-\mathrm{i}k_{2x,n}\bar{x}} - B_{2,n}\,\mathrm{e}^{\mathrm{i}k_{2x,n}\bar{x}}\right)\mathrm{e}^{\mathrm{i}\omega t}\right) \quad , (4.33)$$

$$\tau_{\lambda,n} = -\lambda k_L^2\left(y_2 J_0\left(k_{2rL,n}r\right) + y_3 Y_0\left(k_{2rL,n}r\right)\right)\left(A_{2,n}\,\mathrm{e}^{-\mathrm{i}k_{2x,n}\bar{x}} + B_{2,n}\,\mathrm{e}^{\mathrm{i}k_{2x,n}\bar{x}}\right)\mathrm{e}^{\mathrm{i}\omega t}\,, \quad (4.34)$$

$$\tau_{rx,n} = \tau_{xr,n} = \mu\left(2\mathrm{i}k_{2rL,n}k_{2x,n}\left(y_2 J_1\left(k_{2rL,n}r\right) + y_3 Y_1\left(k_{2rL,n}r\right)\right)\ldots\right.$$
$$\left(A_{2,n}\,\mathrm{e}^{-\mathrm{i}k_{2x,n}\bar{x}} - B_{2,n}\,\mathrm{e}^{\mathrm{i}k_{2x,n}\bar{x}}\right)\mathrm{e}^{\mathrm{i}\omega t}\ldots \quad , (4.35)$$
$$\left.+\left(k_{2x,n}^2 - k_{2rT,n}^2\right)\left(y_4 J_1\left(k_{2rT,n}r\right) + y_5 Y_1\left(k_{2rT,n}r\right)\right)\left(A_{2,n}\,\mathrm{e}^{-\mathrm{i}k_{2x,n}\bar{x}} + B_{2,n}\,\mathrm{e}^{\mathrm{i}k_{2x,n}\bar{x}}\right)\mathrm{e}^{\mathrm{i}\omega t}\right)$$

$$\tau_{r\theta,n} = \tau_{\theta r,n} = \tau_{x\theta,n} = \tau_{\theta x,n} = 0\,. \tag{4.36}$$

Acoustic displacements are $u_{r,n}$, $u_{x,n}$, and $u_{\theta,n}$ in the radial, axial, and circumferential directions, respectively, for each mode n. Normal stresses in the same order are $\tau_{r,n}$, $\tau_{x,n}$, and $\tau_{\theta,n}$; they are all equal in the fluid. The nonzero shear stress in the liner is $\tau_{rx,n} = \tau_{xr,n}$.

Wavenumbers $k_{Rx,n}$ are found by solving an eigenequation in each region. In regions 1 and 3, the equation is formed by setting radial displacement to zero at the outer wall,

$$u_{r,n}\Big|_{r=r_0} = 0, \quad \text{region } 1\,, \tag{4.37}$$

$$u_{r,n}\Big|_{r=b_0} = 0, \quad \text{region } 3\,. \tag{4.38}$$

If no liner is present, the device is a simple expansion chamber, and region 2 is identical to region 3; however, in general a complex eigenequation must be solved for region 2, taking into account seven simultaneous boundary conditions. They are: continuity of radial displacement at a,

$$u_{r,n}\Big|_{r=a^-} = u_{r,n}\Big|_{r=a^+}\,, \tag{4.39}$$

continuity of normal stress at a,

$$\tau_{r,n}\Big|_{r=a^-} = \tau_{r,n}\Big|_{r=a^+}\,, \tag{4.40}$$

zero shear stress at a,

$$\tau_{rx,n}\Big|_{r=a} = 0\,, \tag{4.41}$$

zero shear stress at b,

$$\tau_{rx,n}\Big|_{r=b} = 0\,, \tag{4.42}$$

continuity of radial displacement at b,

$$u_{r,n}\Big|_{r=b^-} = u_{r,n}\Big|_{r=b^+}, \tag{4.43}$$

continuity of normal stress at *b*,

$$\tau_{r,n}\Big|_{r=b^-} = \tau_{r,n}\Big|_{r=b^+}, \tag{4.44}$$

and zero radial displacement at b_0

$$u_{r,n}\Big|_{r=b_0} = 0. \tag{4.45}$$

Combining the radial components into a matrix **X**, discarding the axial and time components, and collecting the coefficients y_1 to y_7 into a vector $\bar{\mathbf{Y}}$, Equations (4.39) through (4.45) can be represented by a multiplication of a matrix **X** by a coefficient vector $\bar{\mathbf{Y}}$,

$$\mathbf{X}\bar{\mathbf{Y}} = \bar{\mathbf{0}}, \tag{4.46}$$

where $\bar{\mathbf{0}}$ is the zero vector. The eigenequation for region 2 is thus

$$\left|\mathbf{X}\right| = 0, \tag{4.47}$$

and is solved for eigenvalues $k_{2x,n}$. For each solution, the eigenvector $\bar{\mathbf{Y}}$, determines the radial mode shapes of the displacement potentials and therefore of the derived acoustic stresses and displacements in region 2.

Equations (4.37), (4.38) and (4.47) must be solved over the frequencies of interest for the eigenvalues $k_{Rx,n}$. Equations (4.37) and (4.38) may be solved numerically, or the first several roots can be found in tables. For the more complicated Equation (4.47), various methods[14, 19, 76] can be employed to find the eigenvalue solutions. In this work, distributed roots are used as initial guesses; a Newton-Raphson method is used to find roots; duplicate roots and divergent solutions are discarded; and checks are made for missed roots using the argument principle. Since axial wavenumbers for reverse

travelling modes are the negative of positive travelling mode wavenumbers, all $k_{Rx,n}$ solutions here will refer to the positive travelling values, which lie on the positive real axis or below the real axis on the complex plane, and negative signs will be added for the reverse travelling modes.

To determine the relative modal amplitudes $A_{R,n}$ and $B_{R,n}$ for each region R and each modal index n, a mode matching technique is implemented. This is accomplished by applying several boundary conditions at the discontinuity planes $x = \{0, L_1, L_1+L, L_0\}$. At the port planes, the conditions are continuity of axial displacement and normal stress, with stress unspecified at $r > r_0$:

$$\sum_{n=0}^{\infty} u_{x,n}\Big|_{x=0^+} = \begin{cases} \sum_{n=0}^{\infty} u_{x,n}\Big|_{x=0^-}, 0 \le r \le r_0 \\ 0, r_0 < r \le b_0 \end{cases}, \tag{4.48}$$

$$\sum_{n=0}^{\infty} u_{x,n}\Big|_{x=L_0^-} = \begin{cases} \sum_{n=0}^{\infty} u_{x,n}\Big|_{x=L_0^+}, 0 \le r \le r_0 \\ 0, r_0 < r \le b_0 \end{cases}, \tag{4.49}$$

$$\sum_{n=0}^{\infty} \tau_{x,n}\Big|_{x=0^+} = \sum_{n=0}^{\infty} \tau_{x,n}\Big|_{x=0^-}, 0 \le r \le r_0, \tag{4.50}$$

$$\sum_{n=0}^{\infty} \tau_{x,n}\Big|_{x=L_0^-} = \sum_{n=0}^{\infty} \tau_{x,n}\Big|_{x=L_0^+}, 0 \le r \le r_0. \tag{4.51}$$

Axial displacement and normal stress continuity are joined by a zero shear stress condition at the liner boundaries:

$$\sum_{n=0}^{\infty} u_{x,n}\Big|_{x=L_1^+} = \sum_{n=0}^{\infty} u_{x,n}\Big|_{x=L_1^-}, 0 \le r \le b_0, \tag{4.52}$$

$$\sum_{n=0}^{\infty} u_{x,n}\Big|_{x=(L_1+L)^+} = \sum_{n=0}^{\infty} u_{x,n}\Big|_{x=(L_1+L)^-}, 0 \le r \le b_0, \tag{4.53}$$

$$\sum_{n=0}^{\infty} \tau_{x,n}\Big|_{x=L_1^+} = \sum_{n=0}^{\infty} \tau_{x,n}\Big|_{x=L_1^-}, 0 \le r \le b_0, \tag{4.54}$$

$$\sum_{n=0}^{\infty} \tau_{x,n}\Big|_{x=(L_0-L_2)^+} = \sum_{n=0}^{\infty} \tau_{x,n}\Big|_{x=(L_0-L_2)^-}, 0 \le r \le b_0, \tag{4.55}$$

$$\sum_{n=0}^{\infty} \tau_{rx,n}\Big|_{x=L_1} = 0, a < r \le b, \tag{4.56}$$

$$\sum_{n=0}^{\infty} \tau_{rx,n}\Big|_{x=L_1+L} = 0, a < r \le b. \tag{4.57}$$

Finally, assuming an anechoic termination of the downstream pipe results in all $B_{1D,n} = 0$. Because the inlet pipe has a small diameter relative to the wavelength of frequencies of concern, all non-plane modes $A_{1U,n}$ are evanescent; and over the inlet and outlet pipe lengths, such modes are sufficiently attenuated that for $n > 0$, $A_{1U,n} = 0$. The plane wave excitation is arbitrarily assigned as unity: $A_{1U,0} = 1$.

For the eigenfunctions in each region, a finite number of roots is found at each frequency, corresponding to a maximum number of modal amplitudes each of $A_{R,n}$ and $B_{R,n}$ that can be found in each region. Thus the boundary conditions listed in Equations (4.48) to (4.57) must be converted to approximate equations. This is commonly accomplished by converting them into discrete integral equations, which may be unweighted, or weighted by area or a radial eigenfunction. For air silencers with inlet and outlet extensions[26, 28], the weighting by eigenfunctions has been generally preferred, as it retains orthogonality and has been shown to have better convergence properties for that kind of device[27]. These weighted[17] as well as unweighted methods[14, 20] have been used for silencers without extensions, and for this case good convergence behavior

has been demonstrated using both methods[27]. For the present study, eigenfunction weighted integrals are used as shown below. The matching equations are:

$$\sum_{n=0}^{N-1}\int_{r=0}^{b_0} u_{x,n}\Psi_{3,p}r\mathrm{d}r\Big|_{x=0^+} = \sum_{n=0}^{N-1}\int_{r=0}^{r_0} u_{x,n}\Psi_{3,p}r\mathrm{d}r\Big|_{x=0^-}, \tag{4.58}$$

$$\sum_{n=0}^{N-1}\int_{r=0}^{b_0} u_{x,n}\Psi_{3,p}r\mathrm{d}r\Big|_{x=L_0^-} = \sum_{n=0}^{N-1}\int_{r=0}^{r_0} u_{x,n}\Psi_{3,p}r\mathrm{d}r\Big|_{x=L_0^+}, \tag{4.59}$$

$$\sum_{n=0}^{N-1}\int_{r=0}^{r_0} \tau_{x,n}\Psi_{1,p}r\mathrm{d}r\Big|_{x=0^+} = \sum_{n=0}^{N-1}\int_{r=0}^{r_0} \tau_{x,n}\Psi_{1,p}r\mathrm{d}r\Big|_{x=0^-}, \tag{4.60}$$

$$\sum_{n=0}^{N-1}\int_{r=0}^{r_0} \tau_{x,n}\Psi_{1,p}r\mathrm{d}r\Big|_{x=L_0^-} = \sum_{n=0}^{N-1}\int_{r=0}^{r_0} \tau_{x,n}\Psi_{1,p}r\mathrm{d}r\Big|_{x=L_0^+}. \tag{4.61}$$

$$\sum_{m=0}^{M-1}\int_{r=0}^{b_0} u_{x,m}\Psi_{3,p}r\mathrm{d}r\Big|_{x=L_1^+} = \sum_{n=0}^{N-1}\int_{r=0}^{b_0} u_{x,n}\Psi_{3,p}r\mathrm{d}r\Big|_{x=L_1^-}, \tag{4.62}$$

$$\sum_{n=0}^{N-1}\int_{r=0}^{b_0} u_{x,n}\Psi_{3,p}r\mathrm{d}r\Big|_{x=(L_0-L_2)^+} = \sum_{m=0}^{M-1}\int_{r=0}^{b_0} u_{x,m}\Psi_{3,p}r\mathrm{d}r\Big|_{x=(L_0-L_2)^-}, \tag{4.63}$$

$$\sum_{m=0}^{M-1}\int_{r=0}^{b_0} \tau_{x,m}\Psi_{3,p}r\mathrm{d}r\Big|_{x=L_1^+} = \sum_{n=0}^{N-1}\int_{r=0}^{b_0} \tau_{x,n}\Psi_{3,p}r\mathrm{d}r\Big|_{x=L_1^-}, \tag{4.64}$$

$$\sum_{n=0}^{N-1}\int_{r=0}^{b_0} \tau_{x,n}\Psi_{3,p}r\mathrm{d}r\Big|_{x=(L_0-L_2)^+} = \sum_{m=0}^{M-1}\int_{r=0}^{b_0} \tau_{x,m}\Psi_{3,p}r\mathrm{d}r\Big|_{x=(L_0-L_2)^-}, \tag{4.65}$$

$$\sum_{m=0}^{M-1}\int_{r=a}^{b} \tau_{rx,m}\Psi_{2,q}\mathrm{d}r\Big|_{x=L_1} = 0, \tag{4.66}$$

$$\sum_{m=0}^{M-1}\int_{r=a}^{b} \tau_{rx,m}\Psi_{2,q}\mathrm{d}r\Big|_{x=L_0-L_2} = 0, \tag{4.67}$$

$$\Psi_{1,p} = J_0\left(k_{1rf,p}^{*}r\right), \tag{4.68}$$

$$\Psi_{3,p} = J_0\left(k^*_{3rf,p} r\right), \tag{4.69}$$

$$\begin{aligned}\Psi_{2,q} = \mu^* \Big(&-2\mathrm{i} k_{2rL,q} k_{2x,q} \left(y_2 J_1\left(k_{2rL,q} r\right) + y_3 Y_1\left(k_{2rL,q} r\right)\right)\ldots \\ &+\left(k^2_{2x,q} - k^2_{2rT,q}\right)\left(y_4 J_1\left(k_{2rT,q} r\right) + y_5 Y_1\left(k_{2rT,q} r\right)\right)\Big)^*\end{aligned}, \tag{4.70}$$

where the asterisk (*) indicates the complex conjugate, p are the integers 0 to N - 1, and q are 0 to M - N - 1. Equations (4.58) to (4.67) represent $6N + 2M$ equations, to be solved for the same number of unknown modal amplitudes. If N modes are found in each region, then Equations (4.48) to (4.57) overconstrain the system, and it must be solved by weakening the boundary conditions or using an error minimization technique on the total set of equations. Nennig *et al*.[19] use both of these techniques with a similar problem; for the present problem, the extra constraints are handled by solving for $M = 2N$ modes in region 2. In this way, each constraint is solved for a set of equations weighted by the first N modes. The benefits of orthogonality are achieved with those equations weighted by $\Psi_{1,p}$ and $\Psi_{3,p}$, while the shear stress matching with $\Psi_{2,q}$ weighting does not have an orthogonality relationship. Also note that the dual conditions in Equations (4.48) and (4.49) are not explicitly satisfied, but are implicit in the weaker weighted forms of Equations (4.58) and (4.59).

In matrix form, Equations (4.58) to (4.67) are represented as

$$\mathbf{S}\bar{\mathbf{V}} = \bar{\mathbf{W}}, \tag{4.71}$$

where $\bar{\mathbf{V}}$ is the vector of unknown modal amplitudes,

$$\bar{\mathbf{V}} = \begin{bmatrix} B_{1U,0}, B_{1U,1}, \ldots B_{1U,N-1}, A_{2,0}, \ldots A_{2,M-1}, B_{2,0}, \ldots B_{2,M-1}, A_{1D,0}, \ldots A_{1D,N-1}, B_{1D,0}, \ldots B_{1D,N-1}, \\ A_{3U,0}, \ldots A_{3U,N-1}, B_{3U,0}, \ldots B_{3U,N-1}, A_{3D,0}, \ldots A_{3D,N-1}, B_{3D,0}, \ldots B_{3D,N-1} \end{bmatrix}^T, \tag{4.72}$$

$\mathbf{S}$ is the matrix of coefficients to the unknown amplitudes, and $\bar{\mathbf{W}}$ is the vector of coefficients to the known modal amplitude $A_{1U,0}$. Equation (4.71) is solved for $\bar{\mathbf{V}}$ numerically. To improve the condition number of $\mathbf{S}$, each row along with the corresponding row in $\bar{\mathbf{W}}$ is scaled so that the maximum coefficient value is unity.

Transmission loss (TL) is found from the complex wave amplitudes which may be extracted from $\bar{\mathbf{V}}$. In this simulation, the downstream termination is modeled as anechoic, so only the ratio of transmitted plane wave amplitude $A_{1D,0}$, extracted from $\bar{\mathbf{V}}$, to excitation $A_{1U,0} = 1$, is needed, resulting in the calculation

$$\mathrm{TL} = -10\log_{10}\left(\left|\frac{A_{1D,0}}{A_{1U,0}}\right|^2\right), \tag{4.73}$$

where TL represents the reduction in acoustic energy between the upstream and downstream pipe sections.

4.1.3 Finite Element Model Validation

To test the validity of the multimodal model, a 2D axisymmetric finite element (FE) model was generated and evaluated in ANSYS for a frequency range of 50 to 2000 Hz. The device is modeled as a continuous steel outer structure, a centered lossy insert, and the remainder hydraulic fluid. The dimensions of the device are L = 0.0919 m, L_0 = 0.0984 m, L_1 = 0.0032 m, L_2 = 0.0032 m, r_0 = 0.0107 m, a_0 = 0.0132 m, a = 0.0123 m, b_0 = 0.0315 m, and b = 0.0294 m. The fluid has sound speed c_f = 1400 m s^{-1} and density ρ_f = 866 kg m^{-3}. The steel casing is assigned a Young's modulus of 200 GPa, Poisson's ratio 0.29, and density 8000 kg m^{-3}. The liner properties are inherently frequency dependent, and also include damping. ANSYS allows for a complex Young's modulus but only a

real Poisson's ratio, which therefore requires λ and μ to have the same loss factor. The Lamé parameters are approximated as

$$\lambda = (33.0)\left(1+\left(0.200+\frac{0.100\,f}{1000}\right)\mathrm{i}\right) \tag{4.74}$$

$$\mu = \left(4.1+\frac{0.34\,f}{1000}\right)\left(1+\left(0.200+\frac{0.100\,f}{1000}\right)\mathrm{i}\right) \tag{4.75}$$

where f is frequency in Hz, and the results are in MPa. Additionally, ρ_s = 780.2 kg m^{-3}. This approximation of linear storage moduli and loss factors is identical in form to that used for material property estimation in Section 4, and similar in complexity to some models for viscoelastic hoses[37, 43]. The values used are similar to the values estimated from experimental data, though not identical due to the requirement of identical loss factors for λ and μ; the material model is discussed further in the Section 4.

The device is meshed entirely with tetrahedral elements FLUID89 and PLANE182, with a maximum element edge length specified for meshing; the meshed geometry is illustrated in Figure 7. In addition to the axisymmetry condition, one outer corner of the steel structure is constrained to zero displacement. Acoustic excitation is added by constraining the inlet and outlet fluid planes to a specified complex pressure amplitude. As the method of determining TL is independent of end conditions for linear systems, the choice of pressures is arbitrary. For this test the inlet is set to 0.34 MPa, and the outlet is set to zero. The length between the end planes and the expansion planes is sufficient that any evanescent waves are attenuated by several orders of magnitude, so the plane wave conditions should be acceptable to analyze transmission loss.

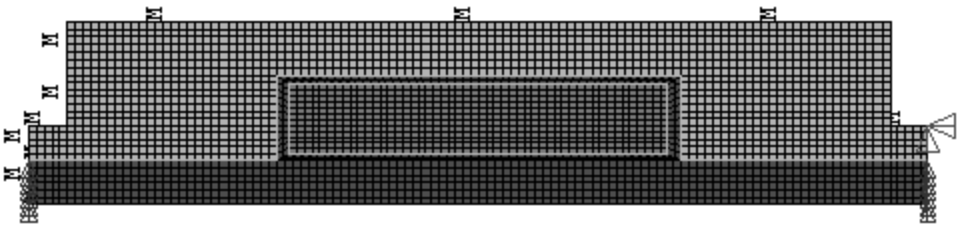

Figure 7: Finite element mesh with boundary and loading conditions. The bottom horizontal line is the axis of symmetry.

To find TL, average normal acoustic velocities q_1 and q_2 are extracted from the simulation results at the upstream and downstream boundary planes, respectively. Combined with applied pressures p_1 and p_2, these quantities are used to determine plane wave amplitudes

$$\begin{aligned} A_U &= 0.5\left(p_1 + \rho_f c_f q_1\right),\ B_U = 1 - A_U \\ A_D &= 0.5\left(p_2 + \rho_f c_f q_2\right),\ B_D = 1 - A_D \end{aligned}, \tag{4.76}$$

at the simulation boundary planes. These relate to the wave amplitudes as shown in Figure 6(b) by the modeled inlet and outlet length x_0 = 0.06m, which is the length between the end planes of the FE model and the expansion planes. The relations are

$$\begin{aligned} A_{1U,0} &= A_U e^{\mathrm{i}k_f x_0},\ B_{1U,0} = B_U e^{-\mathrm{i}k_f x_0} \\ A_{1D,0} &= A_D e^{-\mathrm{i}k_f x_0},\ B_{1D,0} = B_D e^{\mathrm{i}k_f x_0} \end{aligned}. \tag{4.77}$$

A generic TL equation can be derived from Equations (1-4) from Johnston *et al.*[72] where the end-to-end symmetry simplifications are used. In terms of wave amplitudes as described in this text, the result is

$$\mathrm{TL} = 20\log_{10}\left(\left|\frac{A_{1U,0}^2 - B_{1D,0}^2}{A_{1U,0}A_{1D,0} - B_{1U,0}B_{1D,0}}\right|\right). \tag{4.78}$$

This calculation is independent of termination impedance, and reduces to Equation (4.73) in case of an anechoic termination.

The results of the FE model are compared to those of the multimodal model with the same geometric dimensions and material properties, with the exception that the multimodal model assumes a rigid outer boundary rather than a steel casing. The multimodal model also uses unity amplitude plane wave excitation as discussed previously, but the TL calculations are theoretically equivalent so the discrepancy is inconsequential. Results for the FE and multimodal models are shown in Figure 7. Convergence is shown by using maximum element lengths of 0.002 and 0.001 for the FE model, and using $N = 5$, $M = 10$ and $N = 10$, $M = 20$ modes for the multimodal model. Results are generally close even for the lower number of modes and larger mesh sizes, and the additional refinements show that both models have converged upon a solution. In order to quantify the difference between the models, the root mean squared error (RMSE) in TL is calculated by the formula

$$\mathrm{RMSE}\left(\mathrm{TL}\right) = \left(\sum_{i=1}^{N_p} \frac{\left(\mathrm{TL}_{e,i} - \mathrm{TL}_{m,i}\right)^2}{N_p} \right)^{\frac{1}{2}}, \tag{4.79}$$

where $\mathrm{TL}_{e,i}$ is the TL for each reference data point i, in this case of the 0.001 m element length FE model; $\mathrm{TL}_{m,i}$ is the TL of each other model corresponding to the same frequency; and N_p is the number of data points. Thus RMSE between the two FE models is 0.06 dB, while for the $N = 5$, $M = 10$ and $N = 10$, $M = 20$ multimodal models versus the reference FE model it is 0.33 and 0.14 dB, respectively. As both versions of the multimodal model give very similar results, $N = 5$ and $M = 10$ are chosen as the default number of solution modes for the remaining results in this chapter and following.

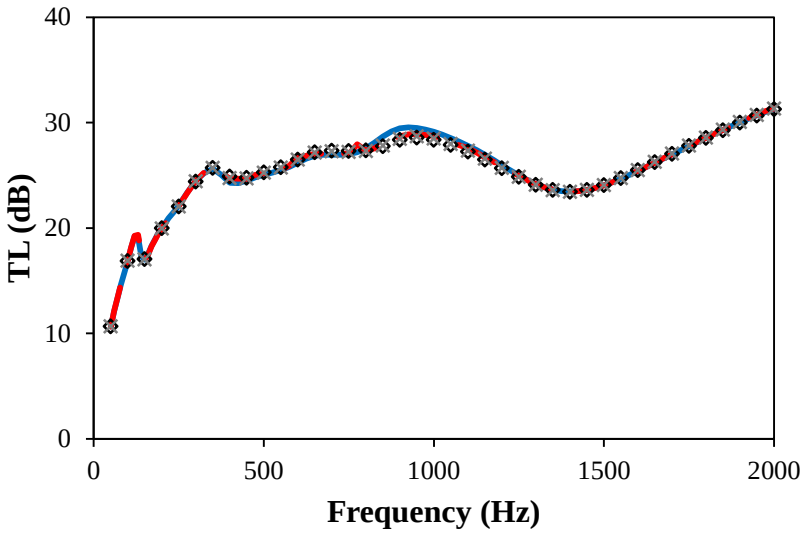

Figure 8: Predicted transmission loss from FE and multimodal models: ▬ Multimodal model, N = 5, M = 10; ▬ ▬ Multimodal model, N = 10, M = 20; ◇ FE model, max element length 0.002 m; × FE model, max element length 0.001 m.

4.2 Experiment

In order to validate the analytical model for devices with non-rigid liners, a prototype silencer was built and tested. The suppressor dimensions are r_0 = 0.0107 m, a_0 = 0.0132 m, b_0 = 0.0315 m, and L_0 = 0.0984 m. For this experiment, the main frequency range of interest was 0 to 2000 Hz. For additional validation, a half-length prototype device was constructed using the same shell, where the liner had length L_0 = 0.0492, and the remainder of the expansion area was filled with a steel plug with an outer radius of b_0 and inner radius of r_0. These data were filtered by removing data with $e_e > 0.03$.

4.3 Experimental validation

The multimodal model is validated against experimental data for a lined prototype suppressor. To determine a_0, consideration must be made for the compression of the liner under static pressure P_s = 2.1 MPa. To determine the compressed liner dimensions, the liner was pressurized in a chamber with a viewport, and the change in inner radius was

determined using digital photographs. The outer radius and length changes were assumed to be proportional to the inner radius change. The dimensions used in the FE model are based on this estimate, and thus the dimensions are the same as in Section 4.1.3. Likewise, it was assumed initially that the liner was centered axially, that is, $L_1 = L_2 =$ 0.0032 m. After testing, the liner was cut in half axially, and tests were repeated for this half-length liner, with the resulting empty space filled by an annular steel plug. For the half-length test, new lengths are $L_0 = 0.0492$ m, $L = 0.0460$ m, and $L_1 = L_2 = 0.0016$ m. All other dimensions are equal. The fluid temperature for the tests was approximately 35 C.

The liner is composed of a urethane matrix with an engineered microstructure, and its properties depend on temperature, pressure, and frequency. Since the manufacturer could not provide data useful for the operating conditions of interest, material properties have been estimated based on a match to experimental data. Ideally, the liner properties would be characterized by a set of Maxwell or Kelvin-Voigt elements, but for practical considerations and with limited data, considerable simplifications are often made. For example, in characterizing viscoelastic hoses, viscoelastic properties are sometimes approximated as constant[43] or varying linearly with frequency[37]. Thus for a frequency range of 0 to 4000 Hz, it is assumed that the storage modulus and loss factor of the suppressor liner's viscoelastic moduli can be approximated as a linear function of frequency. A material property estimation procedure was performed to estimate λ and μ where the resulting values are of the form

$$\lambda = \left(\alpha_1 + \frac{\alpha_2 f}{1000}\right)\left(1 + \left(\alpha_3 + \frac{\alpha_4 f}{1000}\right)\mathrm{i}\right), \mu = \left(\alpha_5 + \frac{\alpha_6 f}{1000}\right)\left(1 + \left(\alpha_7 + \frac{\alpha_8 f}{1000}\right)\mathrm{i}\right), \quad (4.80)$$

with frequency f in Hz and λ and μ in MPa. This was accomplished by finding parameters α_1 to α_8 that minimize RMSE versus experimental data. Parameter limits are shown in Table 2, along with the best solution. Additional constraint equations ensured damping would not become negative below 4000 Hz,

$$-\alpha_7 - 4\alpha_8 < 0, \tag{4.81}$$

$$-\alpha_3 - 4\alpha_4 < 0 \tag{4.82}$$

A multi-dimensional simulated annealing optimization method was used for the material property estimation, utilizing a freely available implementation designed for the free software package GNU Octave. Maximum and minimum temperature settings were handled automatically by the algorithm; two iterations were used between step size reductions; three size reductions were used between temperature reductions; and a temperature reduction factor of 0.2 was employed. The objective function to be minimized was RMSE for the range 0-2000 Hz, since most hydraulic noise is found in this range, and higher frequency experimental data were likely more prone to error. In this case $TL_{e,i}$ from Equation (4.79) is the experimental value. This material property estimation was performed for both the full and half-length suppressors. The resulting parameters are summarized in Table 2, while the corresponding objective function results are in Table 3. Each set of solution parameters is compared to both the full-length and the half-length suppressor experimental results. As expected, the property estimation results give the lowest RMSE for their respective lengths; they also produce the highest RMSE for the other length. A "compromise" solution provides a middle value of RMSE for each length. The compromise solution is an educated guess based on the full-length and half-

length solution values, but also gives lower error for both test conditions than the simple arithmetic average of α_1 through α_8.

Table 2: Material property estimation limits and solutions

Parameter	Min value	Max value	Solution (full-length)	Solution (half-length)	Compromise solution
α_1	20.00	62.00	24.59	32.97	33.00
α_2	0.00	15.00	4.39	0.00	0.00
α_3	0.050	0.600	0.053	0.570	0.05
α_4	-0.080	0.200	0.070	-0.075	0.07
α_5	4.00	8.00	4.11	4.00	4.10
α_6	0.00	2.00	0.34	0.56	0.34
α_7	0.050	0.600	0.581	0.582	0.600
α_8	-0.080	0.200	0.195	0.200	0.200

Table 3: Root mean squared error for various conditions

Experimental data set (0-2000 Hz)	RMSE, full-length estimated properties	RMSE, half-length estimated properties	RMSE, compromise solution
Full-length suppressor	0.40 dB	3.26 dB	1.33 dB
Half-length suppressor	2.42 dB	1.49 dB	1.69 dB

In comparing the property estimation solutions, it can be seen from Table 2 and Equation (4.80) that both the full-length and half-length liner solutions find approximately identical values for μ near the imposed bounds, as well as the same storage modulus for λ around 2000 Hz. The solution for the half-length liner has a slightly higher λ storage modulus at low frequencies, and higher λ damping than the solution for the full-length liner. While this discrepancy again emphasizes the approximate nature of the property estimation scheme, a sensitivity analysis for the analysis parameters may provide some additional insight. Since the objective function is not smooth, a gradient analysis at a solution parameter vector is not meaningful. Instead, eight additional

simulations are run; in these, all α_i are set equal to the full-length solution values except one, α_j, which is set to the arithmetic mean of the full-length and half-length for j = 1 to 8. Sensitivity measures $f_{j,\text{full}}$ and $f_{j,\text{half}}$ are defined as

$$f_{j,\text{full}} = \left| \frac{\text{RMSE}_0(\text{full}) - \text{RMSE}_j(\text{full})}{\left(\frac{\alpha_0 - \alpha_j}{\alpha_0} \right)} \right|, \quad f_{j,\text{half}} = \left| \frac{\text{RMSE}_0(\text{half}) - \text{RMSE}_j(\text{half})}{\left(\frac{\alpha_0 - \alpha_j}{\alpha_0} \right)} \right|. \quad (4.83)$$

Here RMSE_0(full) is the RMSE of the full-length solution parameter vector, on the full-length model and experiment; RMSE_0(half) is the RMSE still of the full-length solution vector, but on the half-length model and experimental values; RMSEj(full) and RMSEj(half) are the RMSE of the modified parameter vector for the full and half-length cases. Similarly, α_0 is the nominal full-length parameter of index j, while α_j is the modified value. Thus, $f_{j,\text{full}}$ and $f_{j,\text{half}}$ define the change in RMSE of the full and half-length tests for the modified parameter vector versus the full-length solution vector, divided by the fractional change in the single parameter α_j versus the nominal full-length solution parameter. These results are summarized in Table 4, and illustrated graphically in Figure 9. It is seen that sensitivity is generally much higher with respect to the full-length test than the half-length test. This is an expected result, given the noisiness of the half-length experimental data, as shown further below. However, in the cases of α_1 and α_7, both sensitivity values are high, indicating high certainty of those two results. In the case of α_7, the solution values are nearly identical for the full and half-length tests. However, for α_1, the results are somewhat different, even though solution certainty is high for both tests. This suggests that an unknown difference in test conditions may have occurred, or that a flaw or approximation in the model has caused this difference. In

either case, the real part of λ converges in both results around 2000 Hz, so it remains only to select the best α_1, and adjust α_2 to give the common 2000 Hz value. For the compromise solution, it is found that the half-length results for α_1 and α_2 give reasonably good results for both length cases; the other values are chosen based on the full-length results. As a further argument, the sensitivity study was repeated using the half-length solution parameter vector as the nominal values; results shown graphically in Figure 10 confirm the sensitivity trends just discussed.

Table 4: Values for material property estimation sensitivity study

Parameter	α_j	$f_{j,\text{full}}$	$f_{j,\text{half}}$
α_1	28.78	4.25	2.81
α_2	2.19	1.15	0.18
α_3	0.312	0.44	0.06
α_4	-0.003	1.01	0.02
α_5	4.05	0.22	0.04
α_6	0.45	0.02	0.00
α_7	0.581	2.57	1.32
α_8	0.197	0.20	0.12

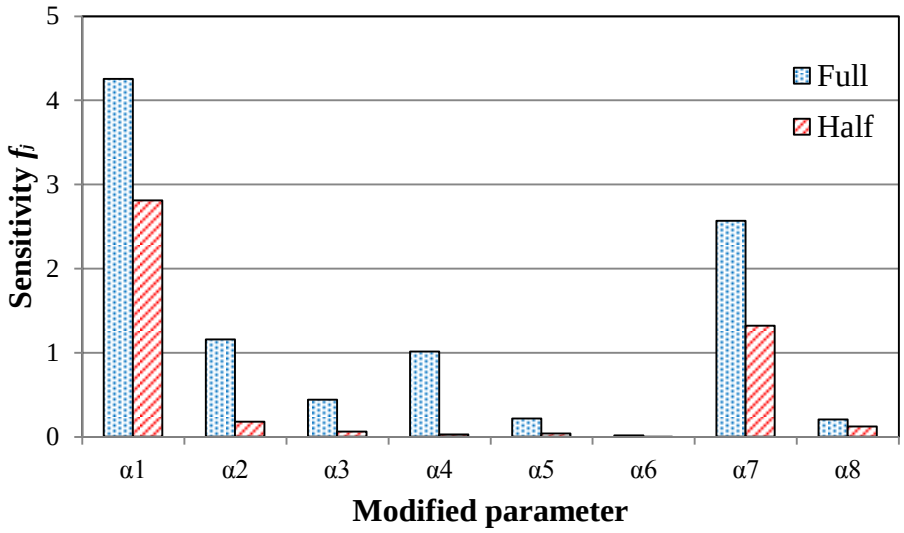

Figure 9: Sensitivity results for full and half-length tests over parameters α_j. Results are relative to the full-length solution parameter vector.

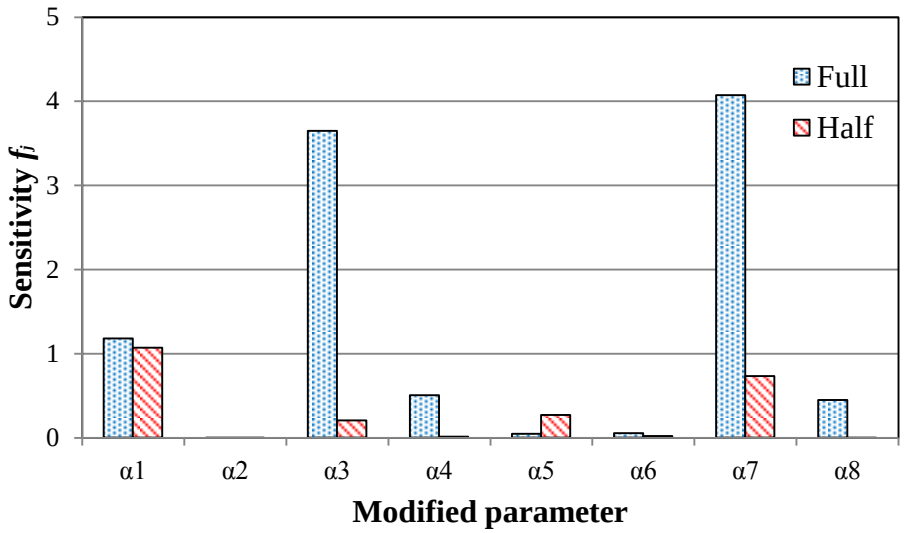

Figure 10: Sensitivity results for full and half-length tests over parameters α_j. Results are relative to the half-length solution parameter vector.

While independent property measurements are currently not available, approximate material property estimation bounds on properties are determined based on available manufacturer data and from the tests used to estimate static compression of the liners. Additionally, CES EduPack[77] is a software package which provides property ranges for many types of materials; comparing estimated properties to CES estimates of shear and bulk modulus for polyurethane rubbers and closed cell foams gives some additional confidence in the estimated material property values. For the foams, CES gives the minimum λ and μ as about 0.26 and 0.10 MPa, respectively, while for the neat polyurethanes the maximum values are about 2000 and 10 MPa. The analysis limits fall within these bounds for the static case; in general it is assumed that the values may be somewhat larger for dynamic properties. The compromise solution values of λ and μ are

$$\lambda = (33.00)\left(1+\left(0.050+\frac{0.070\,f}{1000}\right)\mathrm{i}\right), \tag{4.84}$$

$$\mu = \left(4.10 + \frac{0.34\,f}{1000}\right)\left(1 + \left(0.600 + \frac{0.200\,f}{1000}\right)\mathrm{i}\right). \tag{4.85}$$

The real and imaginary parts (storage and loss modulus) of the compromise solution are plotted over the analysis frequency range in Figure 11. At all modeled frequencies, the λ and μ storage moduli are well within the aforementioned ranges. While the accuracy of the estimated properties cannot be quantitatively determined, it can be concluded that the estimates fall in quite realistic ranges. It should also be stressed that the primary purpose of this study is model development, and that the material property estimation is a necessary supporting task. Reference values are not available for the loss moduli of λ and μ, but the estimated values are plotted in Figure 11.

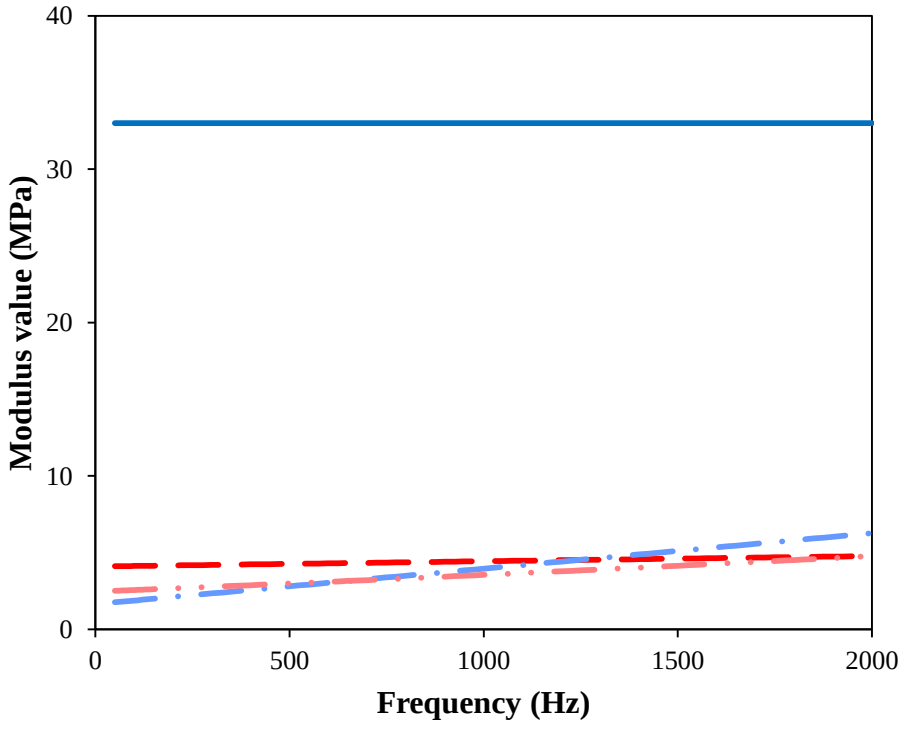

Figure 11: Material storage moduli from compromise solution. real(λ); real(μ); imag(λ), imag(μ).

In Figure 12, the modeled TL predictions are compared to experimental data of the suppressor with the full-length liner at 2.8 MPa (400 psi) mean pressure. Because the material property estimation procedure is very sensitive to experimental error, the data used for objective function calculation has been filtered by removing data points where $e_e > 0.03$. While this removes many experimental artifacts, it may also remove more legitimate features of the data, and consequently some error is expected in the estimated material properties. For clarity in this and other figures, a further reduced set of experimental data is shown, which keeps only one out of ten experimental points; however, this reduced data set is not used for the material property estimation or other data analysis purposes. The full-length liner solution matches generally well over the analysis frequency range, including the small resonance peak around 135 Hz. The half-length liner solution under-predicts TL slightly in the lower frequencies, and over-predicts above about 800 Hz. The compromise solution under-predicts slightly at the lower frequencies as well, but matches closely to the measured TL above about 1000 Hz.

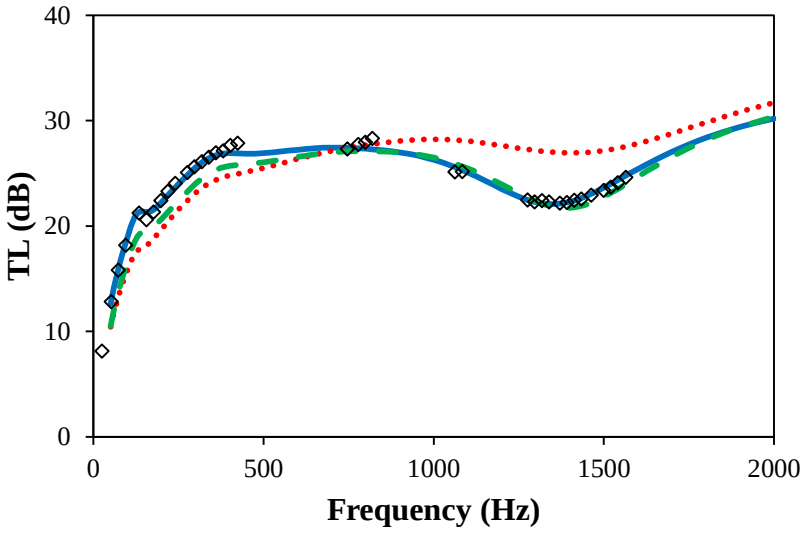

Figure 12: Full-length liner experimental suppressor TL compared to model predicted TL with estimated material properties. ◇ Reduced experimental data; — Model, full-length estimated properties; ▪ ▪ Model, half-length estimated properties; — — Model, compromise properties.

In Figure 13, the TL predictions are compared to the half-length suppressor data. As with the full-length data, TL filtering has been applied for analysis purposes. Given the relative smoothness of the full-length liner data, it is not immediately evident why this test has a much less smooth TL curve than the full-length suppressor test, though the unmodeled dynamics of the steel plug may be a contributing factor. All three solutions follow a roughly average value of the experimental TL above about 1000 Hz, and display a slight resonance peak around 170 Hz which is present in the data. However, the full-length liner solution somewhat over-predicts TL at the lower frequencies, as does the compromise solution to a lesser extent. None of the solutions replicates the sharper TL features in the higher frequencies.

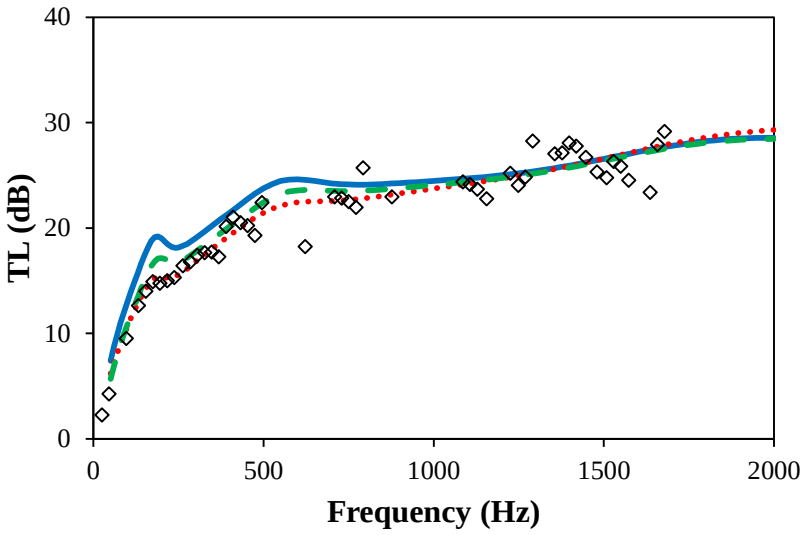

Figure 13: Half-length experimental suppressor TL compared to model predicted TL with estimated material properties. ◇ Reduced experimental data; ▬ Model, full-length estimated properties; ▪ ▪ Model, half-length estimated properties; ▬ ▬ Model, compromise properties.

Due to the imprecise estimate of material properties, the ability to experimentally validate the model is somewhat limited. The compromise solution models the full-length and half-length TL well in an average sense, but misses what appear to be resonance peaks in the half-length device as low as about 400 Hz. The validation against the FE model shows that for the given assumptions about the boundary conditions, the multimodal model is quite accurate. However, with the estimated material properties, and particularly the high loss factor for μ, the model does not predict resonance peaks such as are seen in the half-length TL data. It is therefore unclear whether the difference between model and experiment is due to experimental error or artifacts; over-simplified boundary conditions such as ignoring any shear effects in the hydraulic fluid; inaccurate material property estimates; inaccurate assumptions about the arrangement of the internal device geometry; or another unknown cause.

Geometric positioning sensitivity can be examined to some extent. To test the dependence of the results on the distribution of the axial gap between L_1 and L_2, two additional sets of simulations are run for the full-length device using the compromise solution parameters. In the first, the gap lengths are set to a L_1 = 0.0049 m, L_2 = 0.0016 m and L_2 = 0.0049 m, L_1 = 0.0016 m; the RMSE between these and the version presented above is less than 0.14 dB, with a maximum difference of less than 0.28 dB. In the second set of simulations, L_1 = 0.0065 m, L_2 = 0, and L_2 = 0.0065 m, L_1 = 0. To perform these simulations the boundary conditions must be modified by combining those sets of equations from (4.58) to (4.65) which refer to the same interface, effectively removing the region 3 interface. The results for these cases are still similar, with a maximum deviation of 2.06 dB and RMSE of less than 0.90 over the range of 50 to 2000 Hz. These close matches indicate that the distribution of the axial gaps between L_1 and L_2 is not significant to the results of this study. Since the modeling method depends on axisymmetry, the validity of the assumption that the liner stays radially centered cannot be tested using the current multimodal method. 3D finite element models may be used in the future to test sensitivity to radial misalignment, but it is expected that the flow of hydraulic fluid through the liner annulus will keep the liner somewhat centered about the silencer ports. Alternatively, the liner could be mechanically constrained to remain axially centered.

CHAPTER 5

SYNTACTIC FOAM MODELING

The goal of this chapter is to investigate the material properties of various liners based on their physical composition, and to correlate these properties to TL performance. Several additional prototype liners have been produced for the suppressor discussed in Chapter 4; while more information is available on the composition of the new liners, it is still incomplete, as is the set of material property data. A model to estimate certain material properties is developed, and estimates are further refined using available experimental data.

5.1 Material composition

To begin, the various liner composites are introduced, along with some known or directly measured properties. The liners consist of three different host polymers, to which there are two different varieties of microspheres which may be added. The host polymers shall be labeled MA, MB, and MC, and the added microspheres are labeled 1 and 2. A composite consisting of polymer MA mixed with sphere variety 1 shall be labeled MA1, and so forth. The microsphere nominal radius and density, as well as the polymer and composite material densities, are listed in Table 5 and Table 6. The material used for validation in Chapter 4 was initially produced for model and concept validation purposes, and the manufacturer did not provide specific composition information. It is not analyzed in this chapter, as the newer materials with more complete information are more suitable for the further analysis. Additionally, the composite corresponding to MA2 was not created and is thus not included in the results.

Table 5: Microsphere nominal properties

Sphere type	Product name	Nominal density (kg m^{-3})	Nominal radius (μm)
1	091 DE 80 d30	30	40
2	461 DET 20 d70	70	10

Table 6: Neat polymer and composite densities

Material	Measured density (kg m^{-3})
MA	1051.7
MA1	626.2
MB	1105.0
MB1	643.7
MB2	693.5
MC	1135.8
MC1	543.7
MC2	556.1

The three polymers are designed by the manufacturer to have significantly different shear characteristics. The complex shear modulus μ has been found by the manufacturer at a variety of frequencies and temperatures for composites MA1, MB1, and MC1. However, no such measurements have been performed at elevated pressures, nor at all for materials MB2 or MC2. Table 7 displays some characteristic properties of the sphere 1 composites at temperatures and frequencies representing the range of interest for TL testing. For the frequency values, 1 Hz is taken as representative of low frequency performance, and 1000 Hz is used as a representative high frequency value. The peak loss factor frequency is the approximate frequency at which the loss factor, $\mathrm{Im}(\mu)/\mathrm{Re}(\mu)$, is greatest, and is also indicative of the frequency range at which $\mathrm{Re}(\mu)$ transitions from low to high values.

Table 7: Selected shear modulus properties of composites materials

Material	Temperature (C)	Re(μ) 1 Hz (MPa)	Re(μ) 1000 Hz (MPa)	Peak loss factor frequency (Hz)
MA1	20	3.7	4.8	10^5
MA1	45	3.6	4.0	10^6
MB1	20	3.2	16	400
MB1	45	2.8	3.8	70000
MC1	20	10	80	1.5
MC1	45	2.7	7.8	3000

Notably, the loss factor peak moves from very high frequencies with MA1 to very low with MC1, and MC1 at 20C exhibits a shear modulus much higher than any of the other materials or conditions. Liner TL performance predictions in Section 5.3 directly utilize the available μ values; estimating μ for MB2 and MC2 is discussed further below.

5.2 Static material properties

5.2.1 Theory

In compressible syntactic foams, it is expected that the buckling of microspheres will be the dominant factor in determining the bulk modulus of the composite material, over the range of pressures at which buckling occurs. A model is developed which seeks to describe and predict liner compressibility under static pressure. The model in this section is derived with respect to the material bulk modulus *K*, but will later be applied to λ, under the assumption that $\lambda \approx K$ for $\mu/\lambda \ll 1$.

As with the liner in Chapter 4, the various liners were subjected to a range of hydrostatic pressures, and the internal hole radius *a* was estimated based on digital photographs. Assuming equal strain in all directions, the change in liner volume *V* from its unpressurized value V_0 can be determined based on the cube of the change of any linear dimension. In this case the change of *a* versus unpressurized a_0 is used,

$$\left(\frac{a}{a_0}\right)^3 = \frac{V}{V_0}. \tag{5.1}$$

Theoretically, the axial versus radial compression for a thick cylinder depends on Poisson's ratio; but without knowing Poisson's ratio *a priori*, and expecting it to potentially change with hydrostatic pressure, this is a usable first estimate. Using the relation of Equation (5.1), the radial compression of the liner can be determined from the change in overall volume; this volume change in turn can be predicted based on the static bulk modulus.

A first approximation gives the composite bulk modulus in relation to the bulk moduli and volume fractions of the constituent parts,

$$\frac{V_T}{K_T} = \sum_i \frac{V_i}{K_i}; \tag{5.2}$$

and total volume is found as

$$\frac{V_T}{V_{T0}} = \sum_i \frac{V_i}{V_{T0}} = \sum_i F_{i0} \frac{V_i}{V_{i0}}, \tag{5.3}$$

$$F_i = \frac{V_{i0}}{V_{T0}}, \tag{5.4}$$

for total volume V_T, composite bulk modulus K_T, volumes and bulk moduli V_i and K_i for each of the constituent elements, unpressurized volumes V_{T0} and V_{i0}, and unpressurized volume fraction F_{i0}. The four constituent elements considered in this model are the matrix polymer, unbuckled spheres, buckled spheres, and gas bubbles. Trivett *et al.*[67] note that the microspheres have a high bulk modulus below the critical buckling pressure P_{cr}, but above the pressure

$$P_{cr} = \frac{2Et^2}{r^2\left(3\left(1-\nu^2\right)\right)^{\frac{1}{2}}} \tag{5.5}$$

they act approximately as gas bubbles (here E, ν, t and r are the sphere Young's modulus, Poisson's ratio, thickness, and radius). Thus the buckled spheres as well as the actual gas bubbles are assumed to behave like ideal gases for syntactic foam compliance. Equation (5.3) then becomes

$$\frac{V_T}{V_{T0}} = F_{P0}\mathrm{e}^{-\frac{P_s}{K_P}} + F_{G0}\left(\frac{P_{atm}}{P_{tot}}\right) + F_{U0}\left(G_U\mathrm{e}^{-\frac{P_s}{K_U}} + G_B F_H\mathrm{e}^{-\frac{P_s}{K_H}} + G_B\left(1-F_H\right)\left(\frac{P_{atm}}{P_{tot}}\right)\right) \tag{5.6}$$

$$F_{P0} = \frac{V_{P0}}{V_{T0}},\ F_{G0} = \frac{V_{G0}}{V_{T0}},\ F_{U0} = \frac{V_{U0}}{V_{T0}}, \tag{5.7}$$

$$G_U + G_B = 1, \tag{5.8}$$

$$P_s = P_{tot} - P_{atm}, \tag{5.9}$$

where subscripts $P0$,$U0$, and $G0$ indicate polymer, unbuckled spheres, and gas bubbles, respectively, for the unpressurized state; K_P and K_U are likewise the bulk moduli of the polymer and unbuckled spheres. G_U and G_B represent the fraction of the original volume of microspheres that remain unbuckled or are buckled at a given pressure, such that their sum is always unity, per Equation (5.8). F_H represents the volume fraction of the microspheres that composes the outer shell, and which is characterized by a bulk modulus K_H once a microsphere has bucked. P_{tot} and P_{atm} are the total system pressure and atmospheric pressure; and P_s is system gauge pressure, defined in Equation (5.9). Equations (5.1) and (5.6) may be combined to find inner radius a in terms of pressure,

$$a = a_0\left(F_{P0}\mathrm{e}^{-\frac{P_s}{K_P}} + F_{G0}\left(\frac{P_{atm}}{P_{tot}}\right) + F_{U0}\left(G_U\mathrm{e}^{-\frac{P_s}{K_U}} + G_B F_H\mathrm{e}^{-\frac{P_s}{K_H}} + G_B\left(1-F_H\right)\left(\frac{P_{atm}}{P_{tot}}\right)\right)\right)^{\frac{1}{3}}, \tag{5.10}$$

once G_U and G_B are known.

To determine G_U and G_B, the properties of the microspheres must be further examined. Although each type has a nominal radius as listed in Table 5, the microspheres actually exhibit a great deal of variation. Size variation data are not available for the microsphere types used in this study, but a technical bulletin for a similar product is provided in Appendix A; the size distribution covers approximately an order of magnitude. For the product in Appendix A, the logarithm of the microsphere radii is approximated as a Gaussian distribution with a standard deviation of 0.1639; in this model, a similar distribution is assumed, with the log-mean value given in Table 5, and with a standard deviation σ_s to be determined. Once σ_s is known, this approximation can provide values for r in Equation (5.5), but values for E and v are not precisely known, and t of the microspheres could vary considerably over the size distribution. To generalize the microsphere properties, let it be assumed that P_{cr0} is the buckling pressure corresponding to the nominal radius r_0 of the spheres. If each sphere begins with the same amount of material but is expanded to a different final size, it is then approximately true that

$$t \propto r^{-2}. \tag{5.11}$$

Substituting this result into Equation (5.5), it follows that

$$P_{cr} \propto r^{-6}, \tag{5.12}$$

$$P_{cr} = P_{cr0}\left(\frac{r_0}{r}\right)^6. \tag{5.13}$$

Thus, the smallest sphere radius r that will buckle for a given pressure P_s is

$$r = r_0\left(\frac{P_{cr0}}{P_s}\right)^{\frac{1}{6}}. \tag{5.14}$$

Using a Gaussian distribution described above, the (unpressurized) volume fraction of microspheres with a smaller radius—and which are therefore unbuckled—is

$$G_U = \frac{1}{2}\left(1+\operatorname{erf}\left(\frac{\frac{1}{6}\log_{10}\left(\frac{P_{cr0}}{P_s}\right)}{\sqrt{2\left(\sigma_s^2\right)}}\right)\right), \tag{5.15}$$

and G_B is found simply through Equation (5.8). Equation (5.15) is convenient because it allows the creation of a model which is dependent explicitly on the buckling properties of the microspheres, which can be deduced from pressurization tests, rather than on their detailed composition and geometry.

Some important assumptions are made in this model. First, it is assumed that the host matrix polymer does not significantly affect the buckling behavior of the microspheres. Since the liners are loaded hydrostatically, this may be a reasonable assumption, especially if the liner stiffness is relatively low. Additionally, no effect of temperature on the microsphere shell properties is considered. It is also assumed that $\log_{10}(P_{cr})$ has a Gaussian distribution. These assumptions are made largely due to the limitations of available data, and further testing to verify or refine these modeling assumptions could be beneficial. However, at present the model as presented is still useful, as it allows for some initial predictions of the composite material properties to be made. These assumptions are also reassessed based on the results of the following sections.

5.2.2 Experiment and analysis

The model developed in Section 5.2.1 is used to interpret the results of experimental compression tests for all the composites considered in this chapter.

Experimental values of inner radius a of the liners are collected at various static pressures by measuring the size of a on digital photographs, as discussed in Section 3.4. By performing an inverse analysis and fitting a curve to these experimental data sets, the various parameters of the model can be estimated. The measurements can also be directly employed to estimate K of the liners, but as the experimental data are noticeably not smooth, the model and its resultant smooth curve will allow for better K estimation as well. This curve can be provided using Equation (5.10), along with Equations (5.8) and (5.15). The model fit requires values for F_{P0}, F_{G0}, and F_{U0} for each composite, K_P for each polymer base, and P_{cr0}, K_U, K_H, and F_H for each type of microsphere. While some of these parameters can be estimated using an error minimization technique, trying to find all the parameters in such a manner results in a very poorly conditioned problem. To simplify, several assumptions are made. First, it is assumed that F_{G0} is 0 for all syntactic foams except MC1, which contains some noticeable macro-bubbles. This simplification means that F_{P0} and F_{U0} can be found using the polymer, composite, and microsphere densities found in Table 5 and Table 6. The second assumption is that $K_U = K_P = K_H$ for each base polymer. This simplification is justified if the majority of the compression is due to gas compression in the collapsing microspheres, and thus the intact spheres, shells of the collapsed spheres, and the host polymer appear rigid in comparison. Specifically, if these "harder" elements are contributing significantly to liner compression, it means that the liner is too stiff to provide much noise reduction to the system at that pressure, making the breakdown of this assumption rather unimportant.

Using these assumptions, a simulated annealing optimization was performed to produce a curve fit to all the composite pressure tests. The curve fit objective was

minimization of RMSE between the experimental and model inner radius a of the liner, calculated in the same manner as Equation (4.79); and the results provided input parameters for the theoretical model. In an ideal scenario, a single coupled analysis could be performed, in which parameters are coupled between all liners that share a common base polymer or variety of microspheres. However, a problem with this approach is illustrated in Table 8. The table presents two methods for calculating $F_{U0.}$ The first (density) method uses the polymer, microsphere, and composite densities (ρ_P, ρ_U, ρ_C) presented in Table 5 and Table 6, using the equation

$$F_{U0} = \frac{1}{\rho_U}\left(\rho_C - \rho_P F_{P0} - \rho_G F_{G0}\right), \tag{5.16}$$

where ρ_G is air density, and it is naively assumed that $F_{G0} = 0$. The second (experimental) method assumes that the entirety of the liner compression is due to collapsing microspheres, naively assuming $F_H = 0$,

$$F_{U0} = 1 - \left(\frac{a_f}{a_0}\right)^3, \tag{5.17}$$

where a_f is the final compressed radius. If the ratio between these two values were constant for a given type of microsphere, the difference could be accounted for with a non-zero F_H. However, this is not the case; in actuality, the values vary considerably. Since the ratios for MA1 and MB1 are close to unity while that for MC1 is not, it is theorized that for the former two, the host polymer did not significantly affect microsphere buckling. This would also suggest that MB likewise does not significantly affect buckling for MB2, and that the ratio for MB2 may be addressed by a non-zero F_H. For MC1, the presence of macrobubbles in the liner contradicts the assumption of $F_{G0} = 0$ in Equation (5.16), so it is more difficult to quantify whether or how much MC affects

microsphere performance. Consequently, MA1, MB1, and MB2 are combined into a single curve-fitting analysis, while MC1 and MC2 are treated separately.

Table 8: Microsphere volume (F_{U0}) calculations

Calculation method	MA1	MB1	MC1	MB2	MC2
Density	0.42	0.43	0.54	0.40	0.54
Experimental	0.41	0.40	0.41	0.27	0.42
Ratio	0.97	0.92	0.76	0.68	0.77

The parameter bounds and results for the MA1, MB1, and MB2 curve fit are shown in Table 9; for this analysis, F_{U0} was set by the density method as displayed in Table 8, all $F_{G0} = 0$, and all $K_U = K_H = K_P$. The resulting radial compression curves are shown with experimental data in Figure 14 through Figure 16. These results correspond well with expectations: the type 1 microspheres have a lower critical pressure than type 2, resulting in more compression at lower pressure, as seen in the figures; for MB2 in Figure 16, the relatively flat slope at zero pressure is indicative of the type 2 microspheres beginning to buckle at an elevated pressure, as expected. In addition, type 1 spheres have a larger standard deviation than type 2, which results in a more gradual compression curve, as seen in the experimental data; they have a lower F_H according to the Table 9 results, which corresponds to their lower density given in Table 5.

Table 9: MA1, MB1, MB2 curve fit parameters and results

Parameter	Lower bound	Upper bound	Result
MA K_P (MPa)	1	1000000	216
MB K_P (MPa)	1	1000000	1037
Sphere 1 P_{cr0} (MPa)	0.001	100	0.28
Sphere 2 P_{cr0} (MPa)	0.001	100	1.26
Sphere 1 σ_s	0.01	0.3	0.152
Sphere 2 σ_s	0.01	0.3	0.043
Sphere 1 F_H	0	0.5	0.070
Sphere 2 F_H	0	0.5	0.322

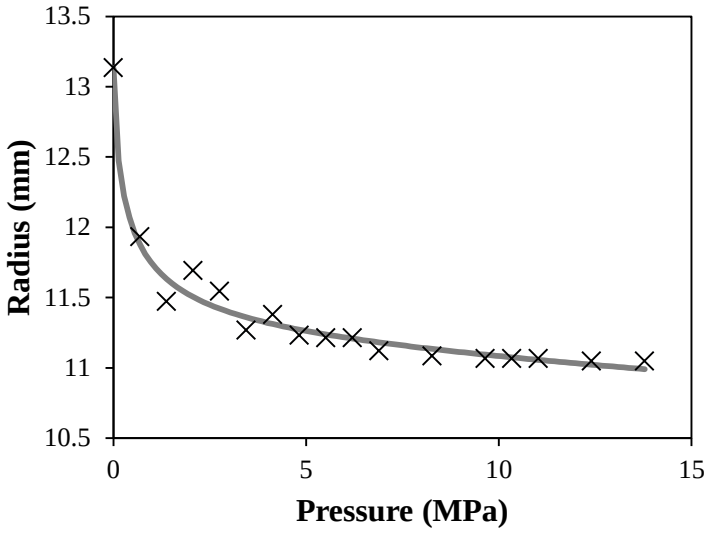

Figure 14: MA1 compression test. × Experimental data; ▬ Model. See Table 9 for model parameters.

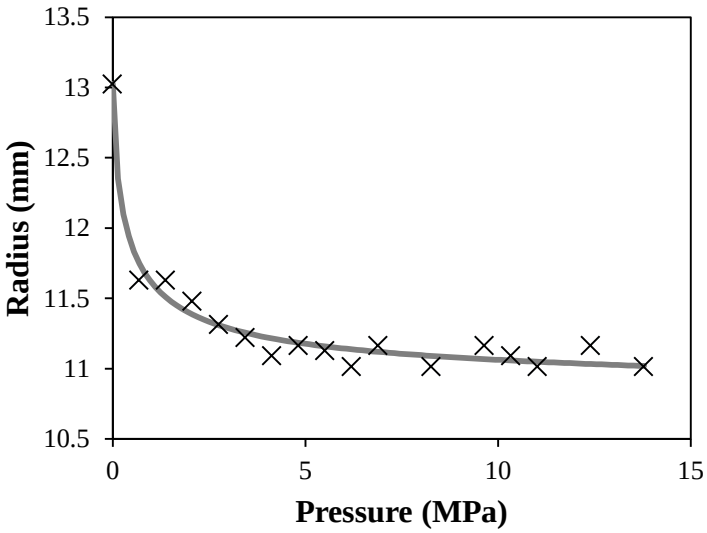

Figure 15: MB1 compression test. × Experimental data; — Model. See Table 9 for model parameters.

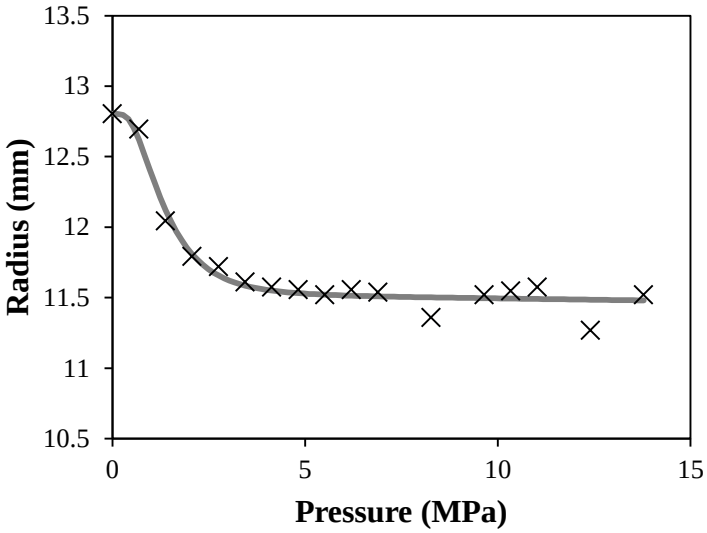

Figure 16: MB2 compression test. × Experimental data; — Model. See Table 9 for model parameters.

Using these results, additional curve fitting analyses were performed to characterize MC1 and MC2. The results are shown in Table 10 and Table 11, respectively; F_{G0_max} indicates the maximum value of F_{G0} which still satisfies Equation (5.16), and the resulting F_{G0} value is 0.268. Gray cells in both tables indicate tighter

restraints based on the values found in Table 9. Compression curves are shown in Figure 17 and Figure 18. The results from the MC1 analysis are not thought to necessarily represent the real material composition: F_{G0} and F_H for MC1 both seem unreasonably high. The MC2 results all appear reasonable, though it characterizes the type 2 spheres much differently from the optimization with MB1. However, the results clearly match the experimental trends in both cases, so it appears that the discrepancy lies in the model not accurately representing some aspect of the actual material. The error possibilities include incorrect composition records, significant effects of the matrix polymer on microsphere buckling pressure, and temperature effects on the matrix polymer or composite (i.e., because the liner is heating during testing, and the MC composites are the most temperature sensitive around the testing temperatures). Some error could possibly be reduced by taking an average of multiple measurements. Additionally, multiple tests might give some insight into potential sample degradation with use; however, this has not yet been studied.

Table 10: MC1 curve fit parameters and results. Highlighted cells indicate constraints based on results shown in Table 9.

Parameter	Lower bound	Upper bound	Result
MC K_P (MPa)	1	1000000	5109
Sphere 1 P_{cr0} (MPa)	0.280	0.281	0.280
F_{G0}/F_{G0_max}	0	1	0.514
Sphere 1 σ_s	0.150	0.160	0.150
Sphere 1 F_H	0	0.5	0.5

Table 11: MC2 curve fit parameters and results. Highlighted cells indicate constraints based on results shown in Table 9.

Parameter	Lower bound	Upper bound	Result
MC K_P (MPa)	1	1000000	419
Sphere 2 P_{cr0} (MPa)	0.001	100	0.67
Sphere 2 σ_s	0.01	0.3	0.011
Sphere 2 F_H	0.25	0.35	0.25

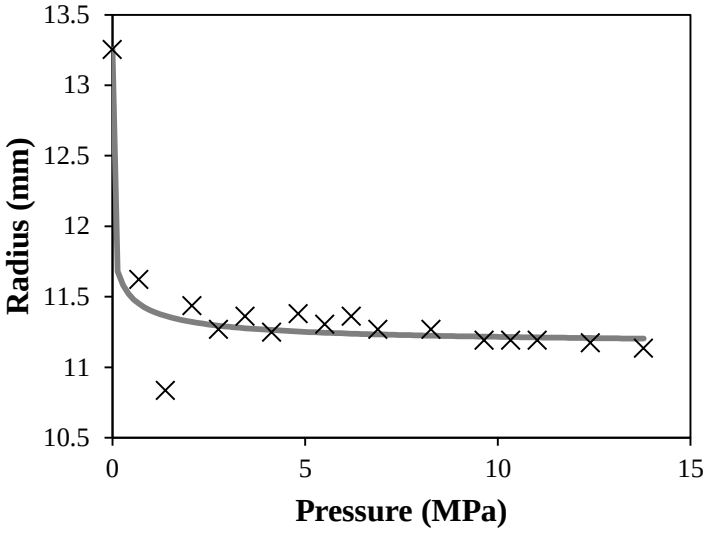

Figure 17: MC1 compression test. × Experimental data; — Model.

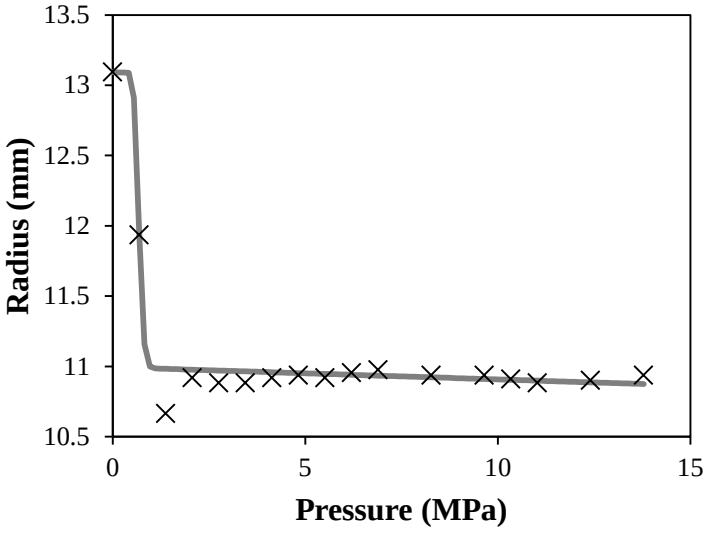

Figure 18: MC2 compression test. × Experimental data; — Model.

5.3 Dynamic properties and transmission loss

While static properties are needed to determine liner compression, dynamic material properties must still be determined in order to predict device TL. To this end, simulated annealing optimization procedures are performed for each material, similar to the process of Chapter 4. However, in this case, the material manufacturer produced master curves for μ of several of the materials at atmospheric pressure, so only λ is found with the property estimation analysis. Values for μ are available for all the neat polymers and composites except MB2 and MC2; additionally, no data are available for the pressurized materials. Values for μ are therefore assumed not to change with pressure, and two attempts are made to estimate μ for MB2 and MC2. In the first case (v1), it is assumed that μ is equal to that for the sphere 1 composites, MB1 and MC1. In the second case (v2), it is assumed that μ falls between the sphere 1 composite and the neat polymer values. In this case, μ is estimated as a weighted average of 2/3 μ of MB1 or MC1, and 1/3 μ of MB or MC. The validity of each of these assumptions is discussed hereafter. To estimate λ, parameters α_1 through α_4 are found, similar to Equation (4.80), defining λ as

$$\lambda = \left(\alpha_1 + \frac{\alpha_2 f}{1000} \right) \left(1 + \left(\alpha_3 + \frac{\alpha_4 f}{1000} \right) \mathrm{i} \right). \tag{5.18}$$

Analyses are performed for each composite at system pressures of 2.8 MPa and 6.9 MPa, and at least two temperatures. This number is doubled for MB2 and MC2, since they have two estimates of μ. Initial parameter limits for α_1, the static value of λ, were estimated using finite difference approximations for bulk modulus based on the compression test models in Section 5.2.2, in the form of

$$\lambda \approx K \approx -a_{\mathrm{avg}}^3 \frac{\Delta P}{\Delta\left(a^3\right)}; \tag{5.19}$$

limits on α_2 were chosen arbitrarily as a fraction of the estimated α_1 value. For both α_1 and α_2, limits were manually expanded, using several property estimation runs if necessary, to ensure that results were comfortably far from the parameter bounds, especially for α_1. Limits on α_3 were set at 0.001 to 0.6, and α_4 limits were -0.3 to 0.3. Notably, these limits are independent of test temperature, since temperature was not recorded for the compression tests. The 2.8 MPa analysis was performed from 0 to 2000 Hz, while for the 4.8 MPa data, the upper range was extended to 3000 Hz, and at 6.9 MPa, 4000 Hz is the upper limit.

The material property estimation results are shown in Table 12, along with static K as calculated from the compression tests, and the ratio of K to α_1, which is the static value of λ in this analysis. The ratio column has darkened cells where the values are greater than 1.15 or less than 0.85; that is, when error is above 15%. Analysis results are shown for two or three test temperatures. Temperatures vary between test conditions due to the lack of a precise temperature control mechanism on the test rig, but enough data sets are available at similar temperatures that useful comparisons can be made.

Table 12: Dynamic material property estimation results. Highlighted cells indicate that K/α_1 deviates from unity by more than 0.15.

Material	Pressure (MPa)	Measured temp (C)	α_1	α_2	α_3	α_4	K estimate (MPa)	K/α_1
MA1	2.8	26	20.2	8.0	0.53	-0.11	37.3	1.85
MA1	2.8	53	32.5	0.0	0.13	-0.02	37.3	1.15
MA1	6.9	32	201	23.6	0.50	-0.07	101	0.50
MA1	6.9	53	274	19	0.14	-0.02	101	0.37
MB1	2.8	26	43.1	12.0	0.60	0.30	41.4	0.96
MB1	2.8	48	48.9	12.0	0.15	0.06	41.4	0.85
MB1	4.8	49	249	30.0	0.29	-0.07	92.2	0.37
MB1	6.9	32	380	50.0	0.21	0.29	155	0.41
MB1	6.9	49	756	47.6	0.31	0.30	155	0.21
MB2 v1	2.8	45	30.4	12.0	0.18	0.15	26.4	0.87

Table 12 Continued

Material	Pressure (MPa)	Measured temp (C)	α_1	α_2	α_3	α_4	K estimate (MPa)	K/α_1
MB2 v1	2.8	51	27.0	9.6	0.23	0.03	26.4	0.98
MB2 v1	2.8	60	28.2	5.6	0.22	-0.06	26.4	0.94
MB2 v1	4.8	50	138	19.6	0.14	0.01	194	1.41
MB2 v1	6.9	45	448	120	0.12	0.30	617	1.38
MB2 v1	6.9	51	438	61.6	0.26	-0.06	617	1.41
MB2 v1	6.9	62	486	2.6	0.23	-0.06	617	1.27
MB2 v2	2.8	45	29.9	12.0	0.40	-0.01	26.4	0.88
MB2 v2	2.8	51	28.1	9.44	0.06	0.14	26.4	0.94
MB2 v2	2.8	60	28.5	5.3	0.01	0.08	26.4	0.93
MB2 v2	4.8	50	135	26.7	0.22	-0.04	194	1.44
MB2 v2	6.9	45	449	120	0.12	0.30	617	1.37
MB2 v2	6.9	51	393	106	0.27	-0.07	617	1.57
MB2 v2	6.9	62	450	13.3	0.12	-0.00	617	1.37
MC1	2.8	26	165	50.0	0.19	-0.04	122	0.74
MC1	2.8	41	75.9	80.0	0.60	0.30	122	1.61
MC1	2.8	49	53.6	12.0	0.22	0.01	122	2.28
MC1	4.8	29	418	179	0.44	0.17	286	0.68
MC1	4.8	42	193	174	0.43	0.14	286	1.48
MC1	4.8	49	138	100	0.40	-0.10	286	2.07
MC1	6.9	32	702	97.6	0.55	0.29	500	0.71
MC1	6.9	44	463	99.3	0.57	0.29	500	1.08
MC1	6.9	50	408	100	0.32	0.30	500	1.23
MC2 v1	2.8	26	124	25.0	0.60	0.30	418	3.37
MC2 v1	2.8	44	36.9	62.4	0.60	-0.03	418	11.33
MC2 v1	2.8	52	33.5	12.0	0.13	0.16	418	12.48
MC2 v1	4.8	30	398	138	0.59	0.02	419	1.05
MC2 v1	4.8	45	162	99	0.53	0.28	419	2.59
MC2 v1	4.8	52	167	29.9	0.20	-0.05	419	2.51
MC2 v1	6.9	33	750	1.6	0.60	0.26	419	0.56
MC2 v1	6.9	46	490	62.4	0.58	0.01	419	0.86
MC2 v1	6.9	53	454	90.7	0.27	0.05	419	0.92
MC2 v2	2.8	26	117	23.1	0.60	0.30	418	3.57
MC2 v2	2.8	44	36.7	67.4	0.60	-0.13	418	11.39
MC2 v2	2.8	52	34.3	12.0	0.06	0.20	418	12.90
MC2 v2	4.8	30	418	87.6	0.60	0.14	419	1.00
MC2 v2	4.8	45	165	124	0.34	0.22	419	2.54
MC2 v2	4.8	52	124	85.1	0.19	-0.00	419	3.38
MC2 v2	6.9	33	754	0.2	0.60	0.25	419	0.56
MC2 v2	6.9	46	465	108	0.60	0.19	419	0.90
MC2 v2	6.9	53	441	99.8	0.31	0.28	419	0.95

At first glance, it appears that the bulk modulus estimates are not very accurate; out of 50 analysis conditions, only 16 have errors less than 15%. However, given the rough nature of the approximation, and the fact that *K* estimates do not account for temperature variations, this is not necessarily a bad start. If only the 20 combinations of material and pressure are considered, 11 have a *K* prediction with less than 15% error at one or more temperatures, or have a *K* prediction that falls between the α_1 values for different temperatures. The remaining poor predictions fall into two categories. First are the values for MA1, MB1, and MB2 at the higher pressure values of 4.8 and 6.9 MPa. In these cases, the slope of the compression curve is small. Since the *K* estimate is related to the inverse of the slope, any small deviation in the slope will be compounded in the *K* calculation; and given the noisy nature of the experimental data, errors in the "true" slope estimate are expected. The second category includes the 2.8 MPa tests for MC2, with both versions v1 and v2. These errors are perhaps reflective of the general difficulty in fitting the compression curve parameters for that material, as well as the significant variation in α_1 that is seen with varying temperatures. Altogether, the *K* estimates from the compression curves provide a suitable starting place for estimating material properties, but for very accurate results, the compression curves will need to be given with temperature dependence as well as pressure, and a measurement technique which produces less noisy data might be required as well.

One addition piece of commentary is warranted for Table 12. For MB2 and MC2, the differences in α_1 and α_2 are minimal between v1 and v2, thus indicating that λ estimation is relatively insensitive to variations in μ in those cases. For MB2, however, there are some notable differences at the lower pressure value (2.8 MPa) in α_3 and α_4,

which relate to material damping; further investigation of material property sensitivity is warranted.

The figures below correlate some of the results of the material property estimation process with TL performance of the lined suppressors at different temperatures and pressures. As in Chapter 4, experimental data only show one out of every ten points, even though all points are used for analysis. For each material, the general trend is an increasing modulus with increasing pressure. This result is seen in the TL performance as a lower TL peak, shifted to a higher frequency, as pressure increases, as demonstrated in Figure 19 to Figure 21 for MA1, MB1, and MC1. This result also agrees with the collapsing sphere model, where at higher pressures a higher fraction of the microspheres have buckled, resulting in a higher bulk modulus. Some temperature variation is present in these data sets, but its effects here are minor compared to the pressure difference.

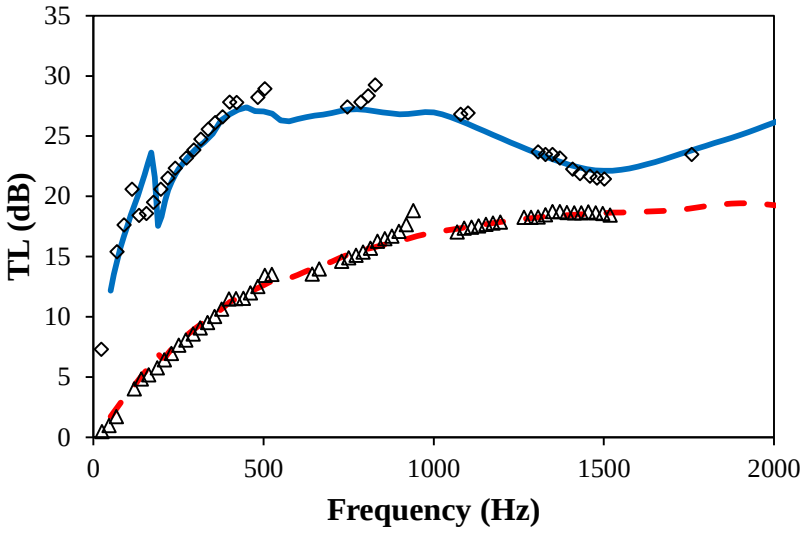

Figure 19: MA1 model and experimental TL at varying pressure and similar temperatures. ◇ Reduced experimental data and — Best fit model, 2.8 MPa, 26C; △ Reduced experimental data and - - Best fit model, 6.9 MPa, 32C.

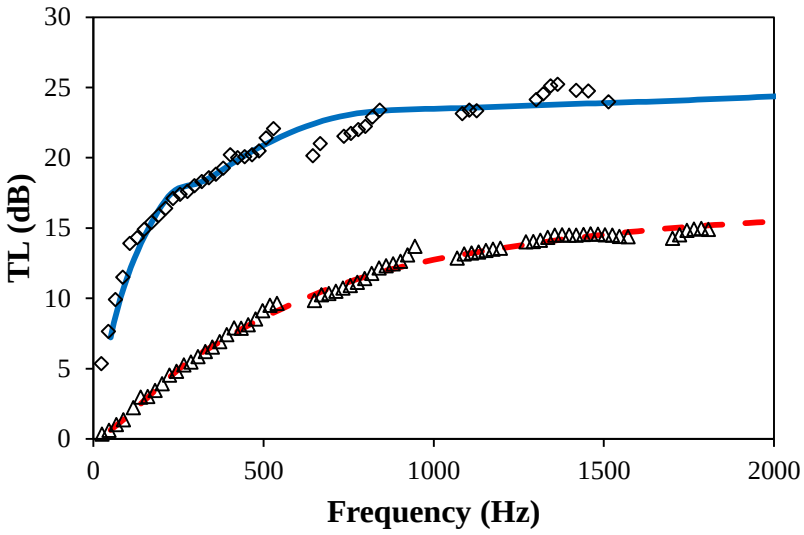

Figure 20: MB1 model and experimental TL at varying pressure and similar temperatures. ◇ Reduced experimental data and — Best fit model, 2.8 MPa, 26C; △ Reduced experimental data and - - Best fit model, 6.9 MPa, 32C.

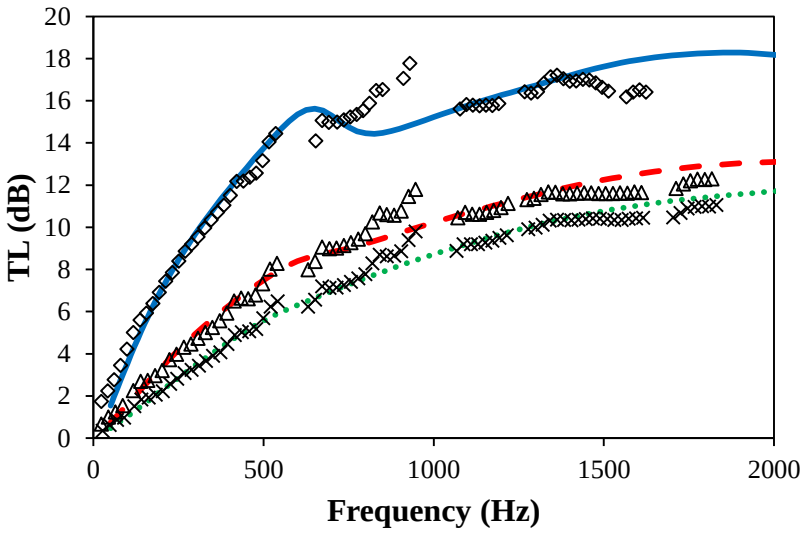

Figure 21: MC1 model and esperimental TL at varying pressure and similar temperatures. ◇ Reduced experimental data and — Best fit model, 2.8 MPa, 26C; △ Reduced experimental data and - - Best fit model, 4.8 MPa, 29C; × Reduced experimental data and ▪ ▪ Best fit model, 6.9 MPa, 32C.

Compared to pressure, a more complex behavior is expected with increasing temperature. As temperature increases, both the host material and the microsphere shells

may soften. If the host polymer does not significantly affect microsphere buckling, then the net result is increased buckling at lower pressures. This will cause a slightly lower bulk modulus at low pressures (generally below the pressures of interest for this study) and a correspondingly higher bulk modulus at higher pressures. This is shown in Figure 22 to Figure 25 for MA and MB. Conversely, it is theorized that the high stiffness of MC serves to impede microsphere buckling at low temperatures, resulting in an overall higher material bulk modulus. However, as temperature increases and MC becomes considerably softer, more microspheres are able to buckle, and the overall bulk modulus decreases. This is shown in Figure 26 and Figure 27. In the figures below, the initial slope of the TL curve is indicative of the static bulk modulus at that test condition. It can be seen that these values are very similar between temperatures for MA1, and for MB1 at 2.8 MPa. However, even if the storage modulus is relatively unchanged, the temperature difference may still significantly affect damping. This effect can be observed by noting the significant change in the higher frequency TL dips; the more pronounced dips at higher frequencies are indicative of lower damping at higher temperatures for MA1, which is corroborated by the material property estimates in Table 12.

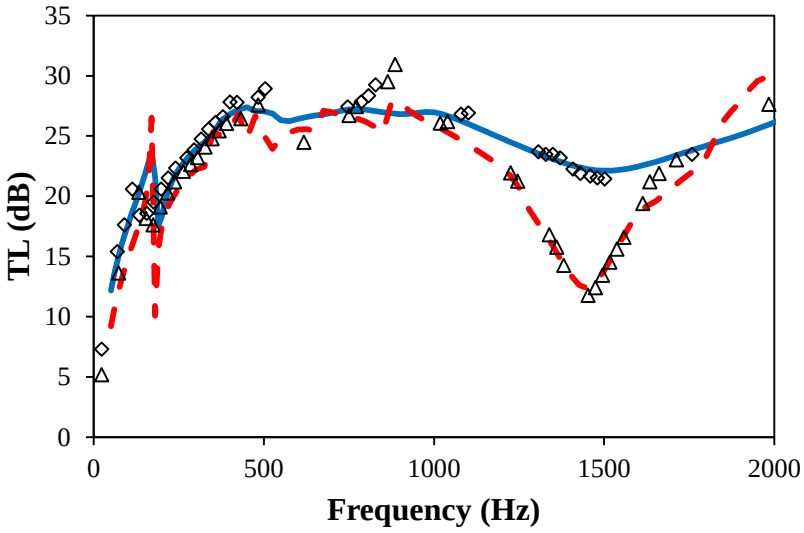

Figure 22: MA1 model and experimental TL at 2.8 MPa and varying temperature. ◇ Reduced experimental data and — Best fit model, 26C; △ Reduced experimental data and – – Best fit model, 53C.

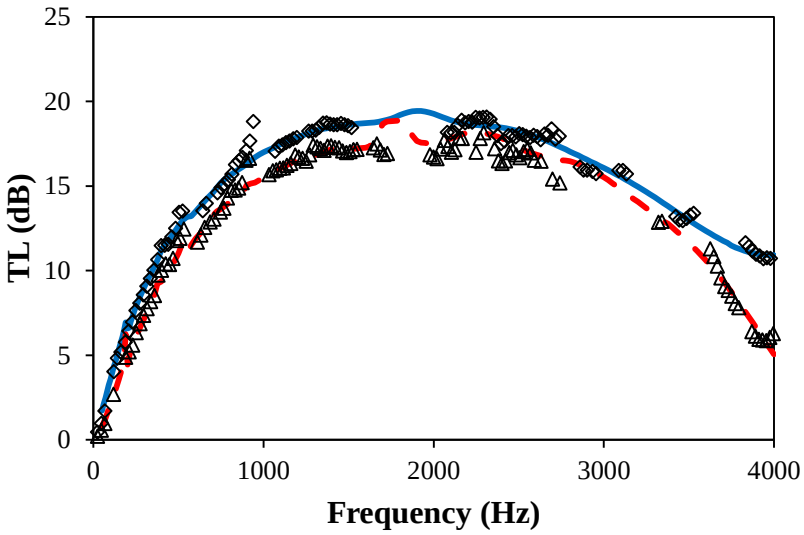

Figure 23: MA1 model and experimental TL at 6.9 MPa and varying temperature. ◇ Reduced experimental data and — Best fit model, 32C; △ Reduced experimental data and – – Best fit model, 53C.

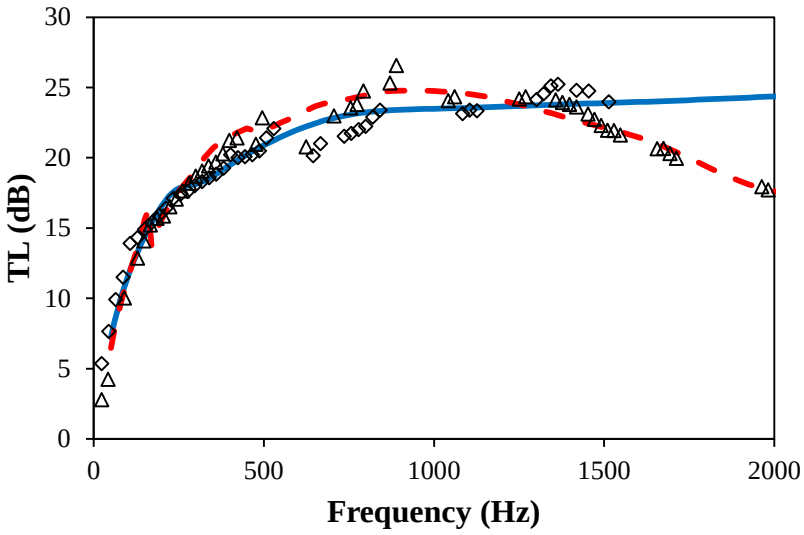

Figure 24: MB1 model and experimental TL at 2.8 MPa and varying temperature. ◇ Reduced experimental data and — Best fit model, 26C; △ Reduced experimental data and — — Best fit model, 48C.

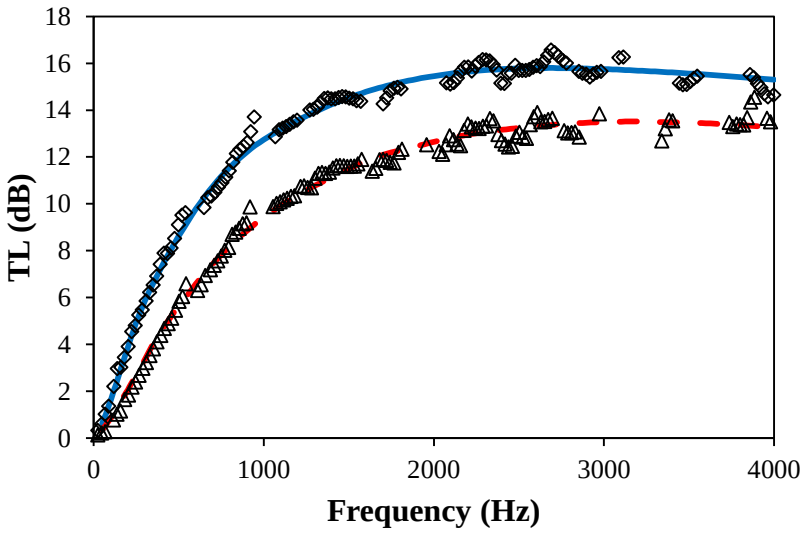

Figure 25: MB1 model and experimental TL at 6.9 MPa and varying temperature. ◇ Reduced experimental data and — Best fit model, 32C; △ Reduced experimental data and — — Best fit model, 49C.

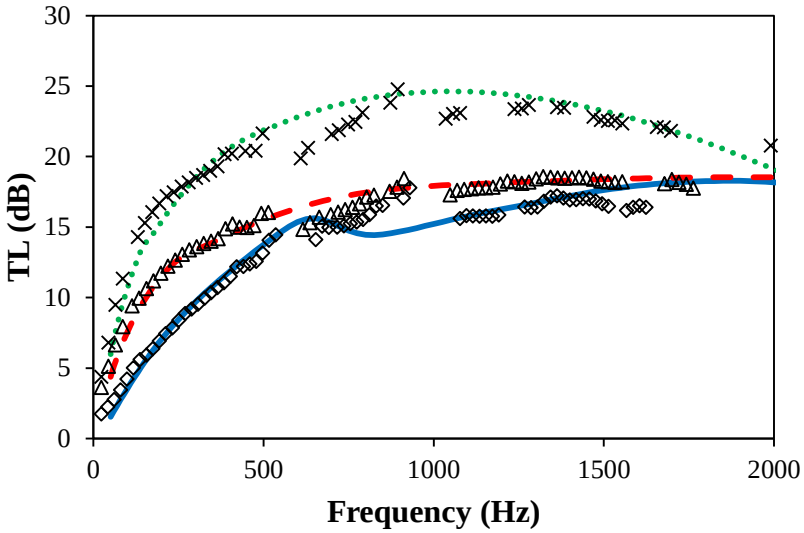

Figure 26: MC1 model and experimental TL at 2.8 MPa and varying temperature. ◇ Reduced experimental data and — Best fit model, 26C; △ Reduced experimental data and — — Best fit model, 41C; × Reduced experimental data and ▪ ▪ Best fit model, 49C.

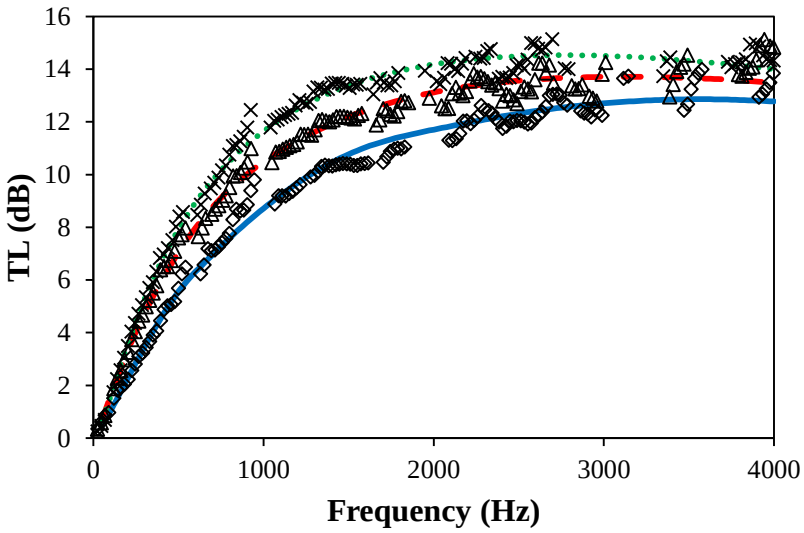

Figure 27: MC1 model and experimental TL at 6.9 MPa and varying temperature. ◇ Reduced experimental data and — Best fit model, 32C; △ Reduced experimental data and — — Best fit model, 44C; × Reduced experimental data and ▪ ▪ Best fit model, 50C.

In addition to noting the effects of temperature and pressure, it is helpful to understand how the different microspheres affect material properties and therefore TL results. In MB, there is a noticeable difference at both the low and high pressures of

interest, 2.8 and 6.9 MPa, as shown in Figure 28 and Figure 29. In both cases, the test pressures are above P_{cr0}, and the smaller spheres of type 2 produce a lower bulk modulus, resulting in higher TL at low frequencies as shown. These results also provide an opportunity to revisit the two estimates for μ that were earlier attempted. In both cases, the difference in TL between the two μ estimates is noticeable but not large. At 2.8 MPa, both MB2 models also show a low frequency resonance around 130 Hz which is offset from the experimental resonance at about 170 Hz; however, not enough information is available to fully determine whether this is due to a poor μ estimation or some other cause.

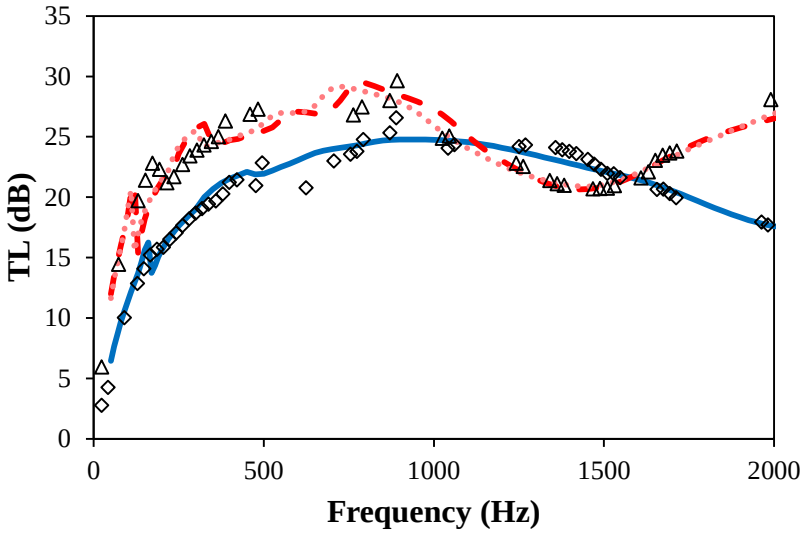

Figure 28: MB model and experimental TL data to compare microsphere types at 2.8 MPa pressure and similar temperatures. ◇ MB1 reduced experimental data and — Best fit model, 48C; △ MB2 reduced experimental data, — — Best fit model v1, and ▪ ▪ Best fit model v2, 51C.

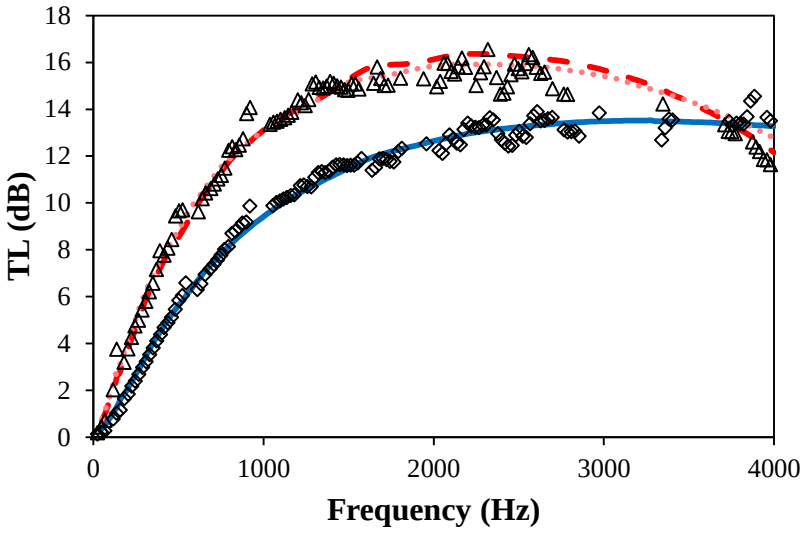

Figure 29: MB model and experimental TL data to compare microsphere types at 6.9 MPa pressure and similar temperatures.◇ MB1 reduced experimental data and ▬ Best fit model, 49C; △ MB2 reduced experimental data, ▬ ▬ Best fit model v1, and ▪ ▪ Best fit model v2, 51C.

Similar to the comparison for MB, MC can also be examined with the two different types of microspheres. In this case, shown in Figure 30 through Figure 33, the results are very similar for both high and low temperatures and pressures. The reason for this is uncertain at this time; it appears that the host polymer dominates the TL response of this liner, to the detriment of any particular microspheres contained therein. In this case, like MB, the two μ estimates provide similar but not identical results.

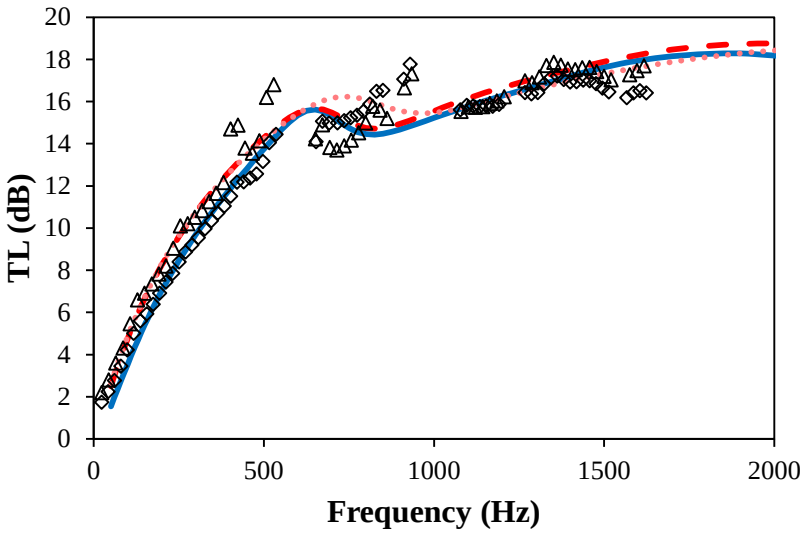

Figure 30: MC model and experimental TL data to compare microsphere types at 2.8 MPa pressure and similar low temperatures. ◇ MC1 reduced experimental data and — Best fit model, 26C; △ MC2 reduced experimental data, — — Best fit model v1, and ▪ ▪ Best fit model v2, 26C.

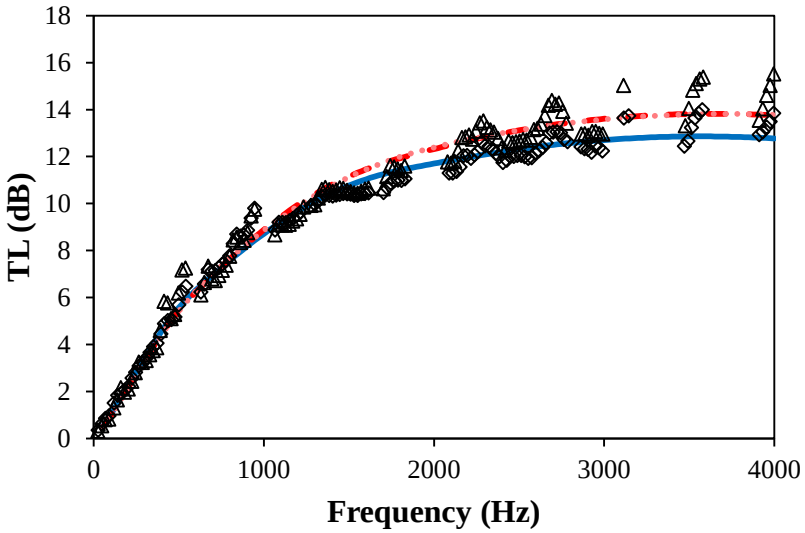

Figure 31: MC model and experimental TL data to compare microsphere types at 6.9 MPa pressure and similar low temperatures. ◇ MC1 reduced experimental data and — Best fit model, 32C; △ MC2 reduced experimental data, — — Best fit model v1, and ▪ ▪ Best fit model v2, 33C.

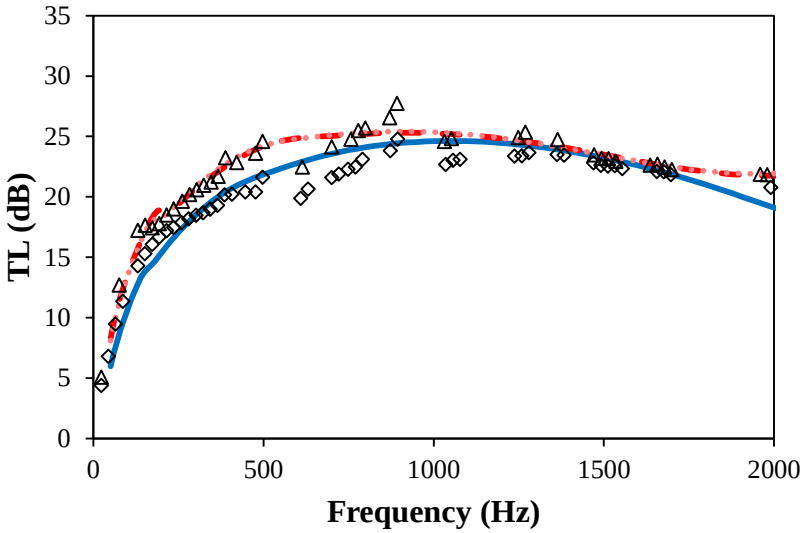

Figure 32: MC model and experimental TL data to compare microsphere types at 2.8 MPa pressure and similar high temperatures. ◇ MC1 reduced experimental data and — Best fit model, 49C; △ MC2 reduced experimental data, — — Best fit model v1, and ▪ ▪ Best fit model v2, 52C.

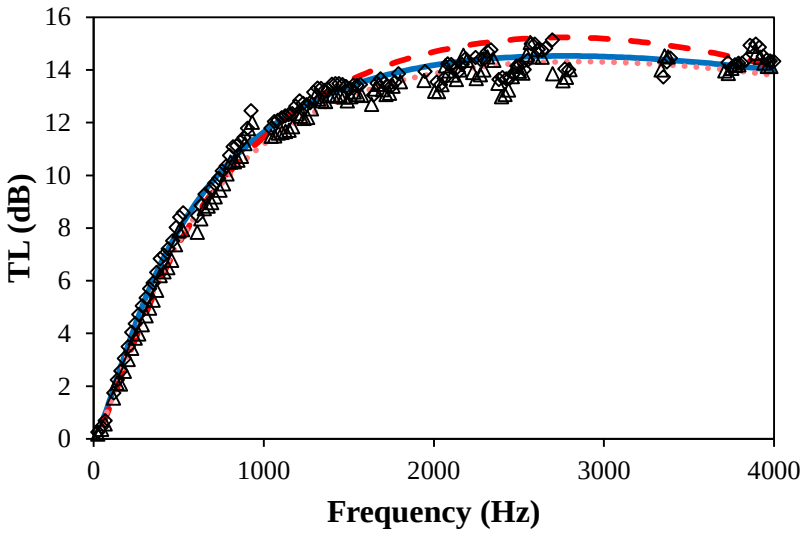

Figure 33: MC model and experimental TL data to compare microsphere types at 6.9 MPa pressure and similar high temperatures. ◇ MC1 reduced experimental data and — Best fit model, 50C; △ MC2 reduced experimental data, — — Best fit model v1, and ▪ ▪ Best fit model v2, 53C.

To further illustrate the effect of the matrix polymer, a comparison at a few different test conditions is shown for MA1, MB1, and MC1 in Figure 34 though Figure

37 below. Notably, MA1 gives the best TL performance at lower frequencies for all cases. MC1 has the worst performance at lower temperatures, but is comparable to MB1 at the higher test temperatures.

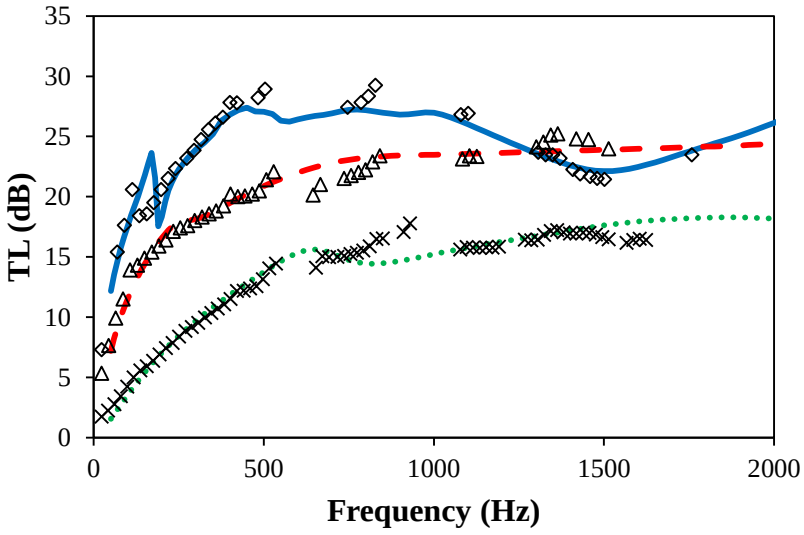

Figure 34: TL comparison between three host polymers containing type 1 microspheres at 2.8 MPa and low temperature. ◇ MA1 reduced experimental data and ▬ Best fit model, 26C; △ MB1 reduced experimental data and ▬ ▬ Best fit model, 26C; × MC1 reduced experimental data and ▪ ▪ Best fit model, 2.8 MPa, 26C.

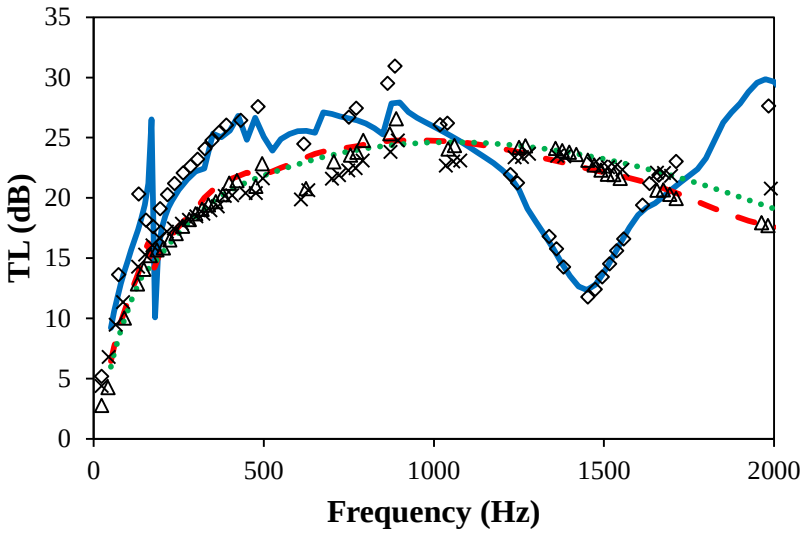

Figure 35: TL comparison between three host polymers containing type 1 microspheres at 2.8 MPa and high temperature. ◇ MA1 reduced experimental data and ▬ Best fit model, 53C; △ MB1 reduced experimental data and ▬ ▬ Best fit model, 48C; × MC1 reduced experimental data and ▪ ▪ Best fit model, 49C.

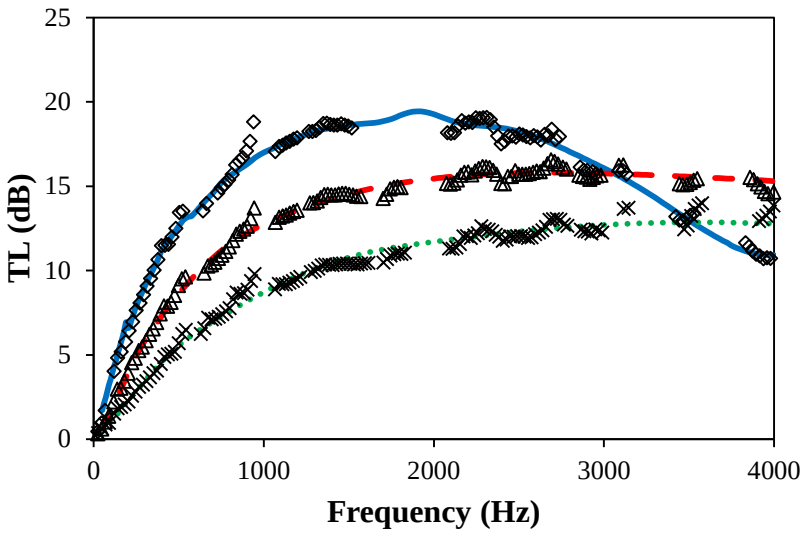

Figure 36: TL comparison between three host polymers containing type 1 microspheres at 6.9 MPa and low temperature.◇ MA1 reduced experimental data and ▬ Best fit model, 32C; △ MB1 reduced experimental data and ▬ ▬ Best fit model, 32C; × MC1 reduced experimental data and ▪ ▪ Best fit model, 32C.

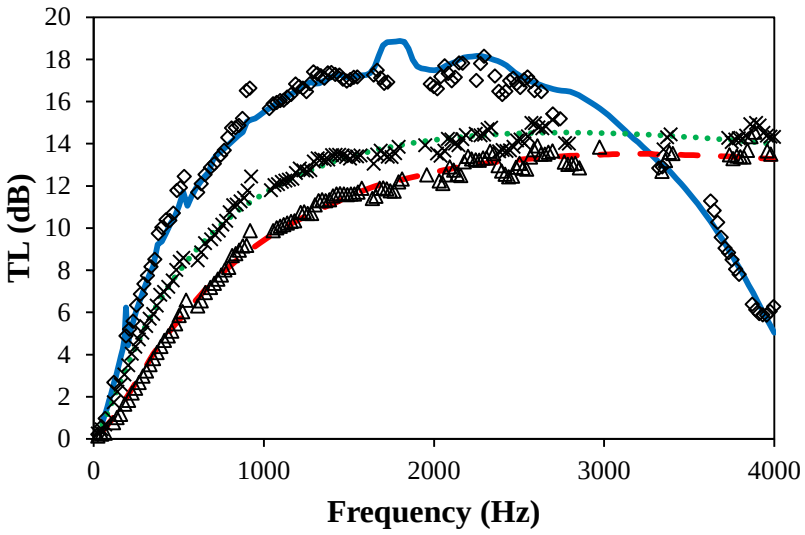

Figure 37: TL comparison between three host polymers containing type 1 microspheres at 6.9 MPa and high temperature. ◇ MA1 reduced experimental data and ▬ Best fit model, 53C; △ MB1 reduced experimental data and ▬ ▬ Best fit model, 49C; × MC1 reduced experimental data and ▪ ▪ Best fit model, 50C.

In addition to the specific comparisons made above, some mention is warranted of the general TL fit between best-fit models and the experimental data. The models reflect the overall TL trend found experimentally, and in some cases indicate low frequency resonances close to what is experimentally found (for example, MA1 in Figure 22). Above about 500 Hz, discrepancies generally appear, in which the models are much smoother than experimental local TL variations, or indicate local resonances which do not align well with experimental data. These discrepancies may be attributed, at least in part, to two obvious causes. First, confidence in the experimental results is lower at these higher frequencies (see Figure 3), so the results may be partly due to artifacts which are not completely removed from the data. Additionally, cumulative errors from the λ linear material property model will be more evident at higher frequencies; and as pressure increases, the μ estimates also likely diverge further from their true values.

5.4 Model sensitivity studies

In order to better understand the accuracy of the material property estimates in Section 5.3, a sensitivity study was performed on the obtained estimates. Because RMSE is not a very smooth function of the viscoelastic moduli, and because the modulus values are only analyzed with respect to λ, a small differential approach to sensitivity testing is not reliable. Instead, sensitivity is tested by effecting a large relative changes in one modulus, while keeping another modulus constant. By changing which modulus is kept constant, the relative sensitivity to changes in each modulus can be estimated. For these tests, λ and μ are modified, with either the other Lamé parameter or K held constant. The results are shown in Table 13 for multiplication factors of 0.5 and 2 for μ, and in Table 14 for a multiplication factor of 0.5 for λ. 2λ is not used since for invariant K, it would generally cause μ to assume negative values, which is non-physical. In these tables, only values for the lowest and highest temperatures at 2.8 and 6.9 MPa pressure are used. Additionally, in Table 13 one entry is omitted, since in the invariant K case, the λ loss modulus would fall below zero, which is again non-physical.

Table 13: Sensitivity study results, varying μ. Shaded cells show where RMSE change is higher with invariant K than invariant λ.

Material	Pressure (MPa)	Measured temp (C)	Nominal RMSE (dB)	μ multiplier	Change (dB) in RMSE, invariant λ	Change (dB) in RMSE, invariant K
MA1	2.8	26	1.36	0.5	-0.07	-0.17
				2	1.39	1.30
MA1	2.8	53	1.72	0.5	0.05	-0.23
				2	1.81	1.39
MA1	6.9	32	0.42	0.5	0.02	0.01
				2	0.11	0.11
MA1	6.9	53	0.58	0.5	0.05	0.05
				2	0.25	0.24
MB1	2.8	26	0.83	0.5	0.22	0.05
				2	0.37	0.23
MB1	2.8	48	0.77	0.5	0.03	-0.03
				2	0.21	0.23
MB1	6.9	32	0.33	0.5	0.01	0.00
				2	0.06	0.02
MB1	6.9	49	0.35	0.5	-0.01	-0.01
				2	0.00	0.00
MB2 v1	2.8	45	1.17	0.5	-0.18	-0.24
				2	0.50	0.46
MB2 v1	2.8	60	1.67	0.5	-0.13	-0.21
MB2 v1	6.9	45	0.38	0.5	-0.01	-0.01
				2	0.01	0.01
MB2 v1	6.9	62	1.05	0.5	-0.08	-0.08
				2	0.02	0.02
MC1	2.8	26	0.82	0.5	0.35	0.15
				2	0.04	0.06
MC1	2.8	49	1.14	0.5	0.08	0.07
				2	-0.13	-0.15
MC1	6.9	32	0.43	0.5	0.00	-0.00
				2	0.05	0.04
MC1	6.9	50	0.35	0.5	-0.00	-0.00
				2	0.00	0.00
MC2 v1	2.8	26	0.82	0.5	0.48	0.29
				2	0.94	0.76
MC2 v1	2.8	52	0.73	0.5	0.11	0.06
				2	0.32	0.32
MC2 v1	6.9	33	0.62	0.5	0.01	0.00
				2	0.02	0.01
MC2 v1	6.9	53	0.73	0.5	0.03	0.02
				2	-0.05	-0.03

Table 14: Sensitivity study results, varying λ. Shaded cells show where RMSE change is higher with invariant K than invariant μ.

Material	Pressure (MPa)	Measured temp (C)	Nominal RMSE (dB)	λ multiplier	Change (dB) in RMSE, invariant μ	Change (dB) in RMSE, invariant K
MA1	2.8	26	1.36	0.5	3.54	1.41
MA1	2.8	53	1.72	0.5	6.95	2.52
MA1	6.9	32	0.42	0.5	3.92	1.24
MA1	6.9	53	0.58	0.5	4.23	3.38
MB1	2.8	26	0.83	0.5	2.93	0.73
MB1	2.8	48	0.77	0.5	3.80	2.09
MB1	6.9	32	0.33	0.5	3.12	1.15
MB1	6.9	49	0.35	0.5	2.90	0.49
MB2 v1	2.8	45	1.17	0.5	3.07	3.10
MB2 v1	2.8	60	1.67	0.5	5.74	4.07
MB2 v1	6.9	45	0.38	0.5	3.42	1.69
MB2 v1	6.9	62	1.05	0.5	2.81	2.43
MC1	2.8	26	0.82	0.5	2.64	2.68
MC1	2.8	49	1.14	0.5	2.74	1.36
MC1	6.9	32	0.43	0.5	2.44	0.38
MC1	6.9	50	0.35	0.5	3.26	0.61
MC2 v1	2.8	26	0.82	0.5	2.32	0.73
MC2 v1	2.8	52	0.73	0.5	3.04	1.73
MC2 v1	6.9	33	0.62	0.5	2.35	0.39
MC2 v1	6.9	53	0.73	0.5	2.96	1.00

Several interesting conclusions can be reached from these two tables. First considering Table 13, it may be noted that in several cases, changing μ actually decreases the root mean squared error. Since μ is estimated from manufacturer's data at different conditions, this is to be expected. Looking at the difference between invariant λ and K, it is seen that except in three of 39 cases (shaded), RMSE increases more with constant λ than with constant K. Moreover, in each of those three cases, the difference is only in hundredths of decibels. Due to the small values of μ relative to λ, λ is approximately equal to K, and this relation has been employed previously in this chapter. In spite of this

near equality, however, the overall result of Table 13 is to show that RMSE stays more constant with invariant K, and that the transmission loss is therefore more sensitive in general to K than to λ. In Table 14, the situation is much the same, but even more dramatically so. In only two of 20 cases (again shaded) are RMSE increases greater with invariant K than with invariant μ, and again in these cases the difference is only in hundredths of decibels. However, in the majority of the remaining cases, the RMSE change of invariant K is more than one decibel lower than that of invariant μ; thus, RMSE is more sensitive to K than to μ.

In Sections 5.2 and 5.3, many aspects of the material model were developed using K. Since K is now shown to be more influential in simulation results than either λ or μ, some simplifications may be possible for the acoustic model presented in Chapter 4. These implications are further explored in Chapter 6.

5.5 Summary

While many improvements can be made, the material model developed in this chapter provides many insights into syntactic foam behavior. The microsphere buckling model helps to quantify liner compression and λ or K variation with pressure, and gives a rough indication of how compression is related to material composition. Best-fit model predictions are correlated with the buckling model for four materials at the lowest pressure considered (2.9 MPa), and are able to match the major TL trends in most experimental data sets. Results from the different matrix polymers show how the polymer choice can significantly affect the composite performance. Pressure and temperature studies show how both the storage and loss moduli can show significant variation under

different conditions; and a sensitivity study indicates the dominance of the material bulk modulus for prediction of transmission loss performance.

CHAPTER 6

MODEL SIMPLIFICATION AND LINER OPTIMIZATION

6.1 Overview

In this chapter, the merits of two model simplifications are considered, and one such simplified model is used in an optimization procedure to design a syntactic foam lined suppressor suitable for use in a mobile hydraulic excavator. The simplified models allow for much faster device simulations, and in one case require the use of only a single viscoelastic modulus, further simplifying the design parameters. The optimization gives a practical application of the model (simplified or otherwise) for use in common mechanical machinery, in such a way as to make comparisons to competing technologies easier. The first set of optimization results are also validated against the original model, to ensure that that the employed simplified model does not significantly alter the device predictions.

6.2 Model simplifications

In section 5.4, it is argued that bulk modulus K is more relevant to transmission loss predictions of the prototype noise suppressor than either of the Lamé parameters λ or μ. If this is true, then it is possible that some simplifications can be made to the model without significantly changing the simulation results. Two simplifications are discussed below, followed by a critical evaluation.

6.2.1 Bulk modulus model

This first simplification attempts to make the suppressor model dependent only on a single viscoelastic parameter. All reference to μ is removed, and λ is replaced by K in

the model in Chapter 4. For comparisons to estimated parameters found in Chapter 5, the moduli are converted by setting

$$K = \lambda + \frac{2}{3}\mu, \tag{6.1}$$

$$\mu_{\text{new}} = 0, \quad \lambda_{\text{new}} = K. \tag{6.2}$$

This simplification sets vector potential $\vec{\psi}$ to zero automatically. This means that the model does not calculate shear stress or shear wave propagation in the liner, so in Equations (4.28) through (4.35), all terms containing μ, k_T, or $k_{2rT,n}$ are identically zero. Additionally, the shear stress boundary conditions expressed in Equations (4.41), (4.42), (4.66), and (4.67) are inapplicable to the simplified model. Consequently, the number of modes found in region 2 can now be equal to the number found in regions 1 and 3; that is,

$$M = N, \tag{6.3}$$

thus avoiding the problem of having more unknown modal amplitudes than constraint equations.

6.2.2 Non-shear model

In this second simplification, again only longitudinal waves are considered, but this is accomplished without removing the shear modulus entirely. The motivation behind this model is that the inclusion of two moduli might better represent more of the experimental TL resonances than just a single modulus. Physically, this gives a more accurate accounting of longitudinal waves than the bulk modulus model, since μ does affect the radial longitudinal wave stress in Equation (4.31). However, by ignoring interactions with shear waves, this model may still produce some inaccuracies. To implement this model, $\vec{\psi}$ is directly set to zero, but λ and μ are unchanged, so the model

results are still a function of two elastic moduli. Thus, in the normal stress Equations (4.31) through (4.33), the terms containing μ but not shear wavenumbers k_T, or $k_{2rT,n}$ are kept. As in the previous simplification, all terms containing shear wavenumbers are removed, as is the same list of equations involving shear boundary conditions; and Equation (6.3) is employed for this simplification as well.

6.2.3 Evaluation of model simplifications

In this section, the two simplified models just described are evaluated to determine their accuracy compared to the nominal simulation results. The bulk modulus model in Section 6.2.1 and the non-shear model in Section 6.2.2 will be compared to the non-simplified model, which will be referred to as the original model. Table 15 shows the RMSE versus experiment for each of the three models. In the case of the original model, the results for selected test cases are simply repeated from Chapter 5; the other models are run for the same test cases, and where RMSE improves over the original model, the cell is shaded gray.

Table 15: Evaluation of simplified models. Shaded cells indicate lower RMSE than the original model.

Material	Pressure (MPa)	Measured temp (C)	RMSE (dB) for model:		
			Original	Bulk modulus	Non-shear
MA1	2.8	26	1.36	1.19	2.09
MA1	2.8	53	1.72	1.54	2.93
MA1	6.9	32	0.42	0.44	0.46
MA1	6.9	53	0.58	0.58	0.59
MB1	2.8	26	0.83	1.22	0.81
MB1	2.8	48	0.77	0.76	0.86
MB1	6.9	32	0.33	0.33	0.32
MB1	6.9	49	0.35	0.34	0.35
MB2 v1	2.8	45	1.17	0.99	1.56
MB2 v1	2.8	60	1.67	1.25	2.29
MB2 v1	6.9	45	0.38	0.37	0.38
MB2 v1	6.9	62	1.05	0.96	0.95
MC1	2.8	26	0.82	1.04	0.86
MC1	2.8	49	1.14	1.25	1.18
MC1	6.9	32	0.43	0.44	0.54
MC1	6.9	50	0.35	0.35	0.35
MC2 v1	2.8	26	0.82	1.38	1.01
MC2 v1	2.8	52	0.73	0.89	0.90
MC2 v1	6.9	33	0.62	0.63	0.69
MC2 v1	6.9	53	0.73	0.74	0.74

In these comparisons, the bulk modulus model performs very well. In eight of 20 tests, it has a lower RMSE than the original model, and in only five of 20 does its RMSE exceed the original model by more than 0.1 dB. The non-shear model gives similar error to the original model in a large fraction of the cases, but higher error in others; its RSME exceeds the original model by more than 0.1 dB in seven cases. Notably, the RMSE values are very similar for all the 6.9 MPa tests, while for the lower pressure 2.8 MPa, the non-shear model varies in its performance versus both the original and the bulk modulus models, depending on the material being tested. For MA1 and MB2 v1, the non-shear model performs worse than both the original and the bulk modulus models; while for MB1 and MC1, the non-shear model has similar error to the original model, and lower

error than the bulk modulus model. For MC2 v1, the non-shear model has higher error than the original model, but lower error than the bulk modulus model only for the low temperature (26 C) case. Some of these results are discussed in the following paragraphs.

Figure 38 and Figure 39 illustrate some of the 6.9 MPa cases, in which the three models give essentially identical RMSE results. It can be seen that there is little variation in TL predictions over the whole range of frequencies shown.

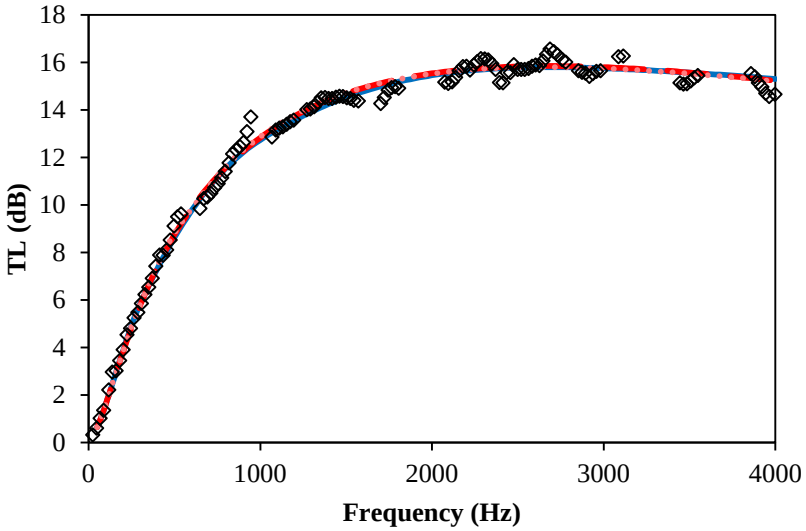

Figure 38: Experimental and model TL for MB1 at 6.9 MPa, 32 C. ◇ Reduced experimental data; — Original model; — — Bulk modulus model; ▪ ▪ Non-shear model.

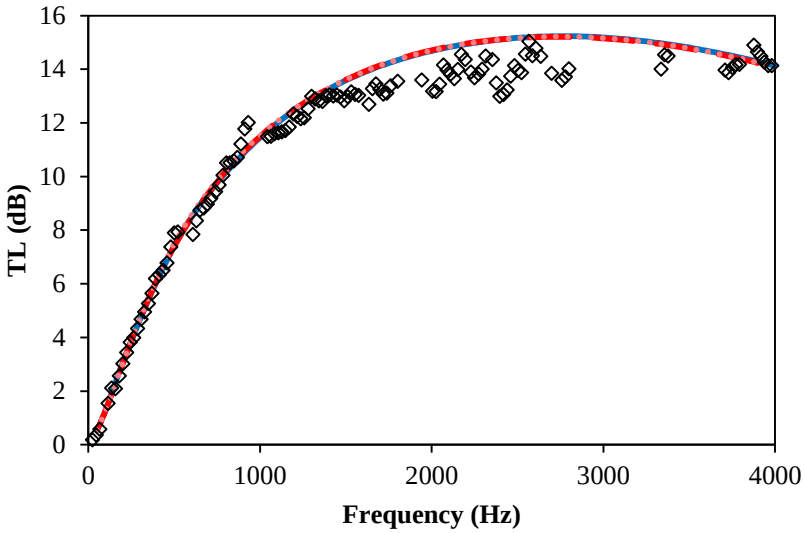

Figure 39: Experimental and model TL for MC2 v1 at 6.9 MPa, 53 C. ◇ Reduced experimental data; — Original model; — — Bulk modulus model; ▪ ▪ Non-shear model.

Figure 40 through Figure 43 show several examples at a system pressure of 2.8 MPa in which the bulk modulus model gives better RMSE than the non-shear model. The non-shear model tends to model the first narrow band resonance peak shown by the original model below about 200 Hz, but it also exhibits strong resonances at higher frequencies that do not match with the experimental data or original model. The bulk modulus model, on the other hand, does not exhibit any narrow band resonance behavior, but smoothly represents the experimental data and original model data without any major deviations.

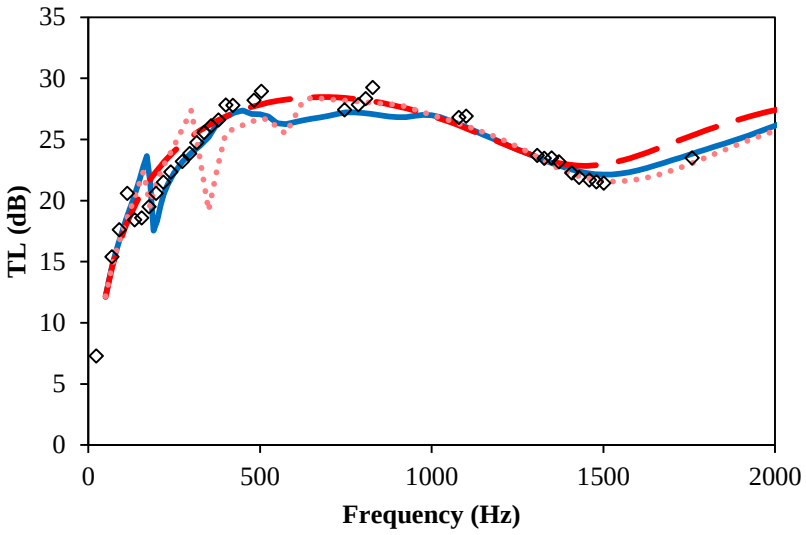

Figure 40: Experimental and model TL for MA1 at 2.8 MPa, 26 C. ◇ Reduced experimental data; — Original model; – – Bulk modulus model; ▪ ▪ Non-shear model.

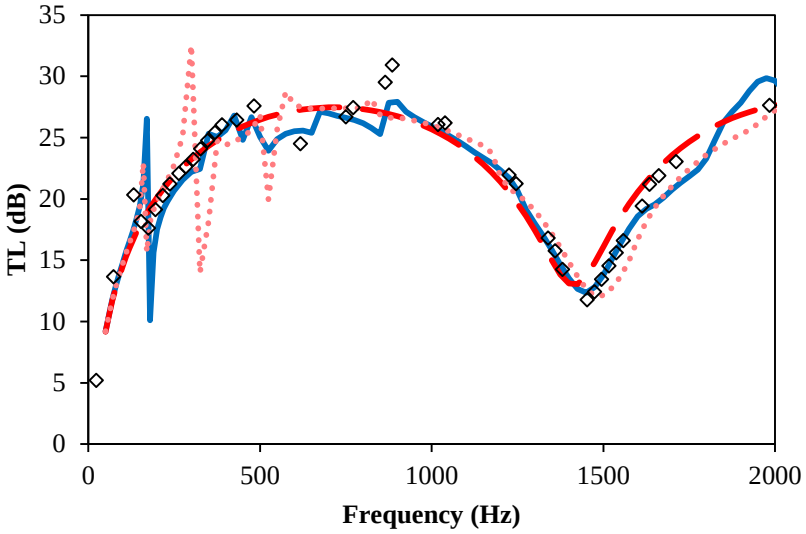

Figure 41: Experimental and model TL for MA1 at 2.8 MPa, 53 C. ◇ Reduced experimental data; — Original model; – – Bulk modulus model; ▪ ▪ Non-shear model.

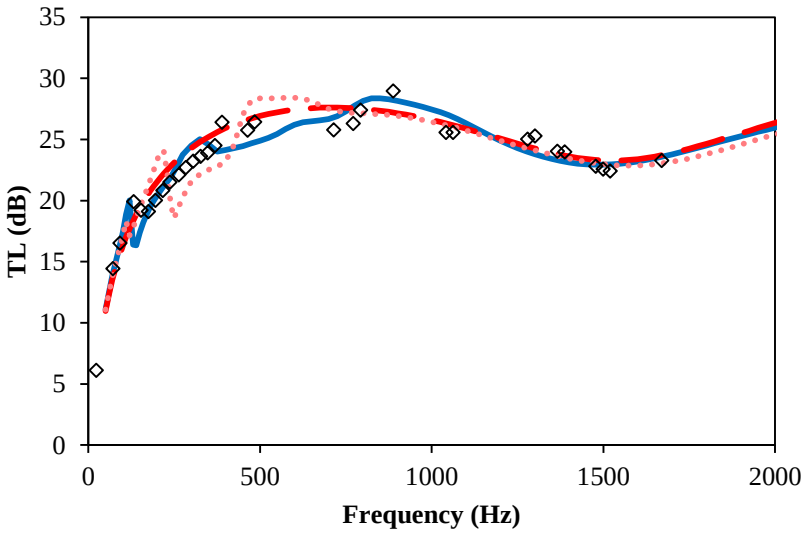

Figure 42: Experimental and model TL for MB2 v1 at 2.8 MPa, 45 C. ◇ Reduced experimental data; — Original model; – – Bulk modulus model; ··· Non-shear model.

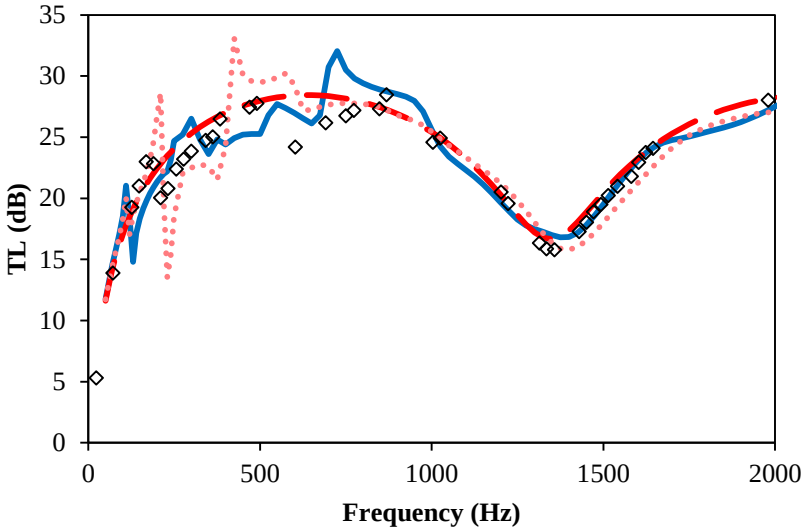

Figure 43: Experimental and model TL for MB2 v1 at 2.8 MPa, 60 C. ◇ Reduced experimental data; — Original model; – – Bulk modulus model; ··· Non-shear model.

In Figure 44 to Figure 46, the cases are shown in which the non-shear model gives lower RMSE than the bulk modulus model. In Figure 44, the models are all qualitatively similar, with the bulk modulus model predicting slightly higher TL overall. In Figure 45 and Figure 46, the non-shear model roughly approximates the bulk modulus until the TL

prediction dips slightly around 1500 Hz; this dip is not observed in the original model, but it still provides a better fit to the experimental data than the bulk modulus model.

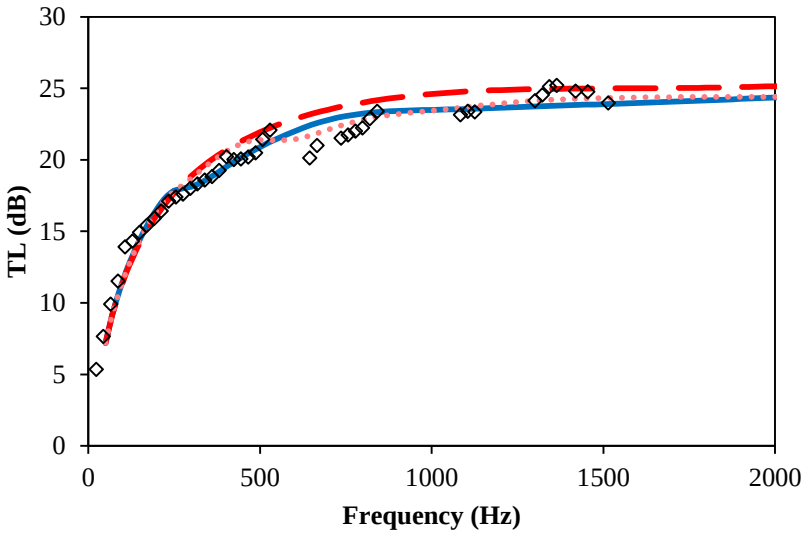

Figure 44: Experimental and model TL for MB1 at 2.8 MPa, 26 C. ◇ Reduced experimental data; — Original model; — — Bulk modulus model; ▪ ▪ Non-shear model.

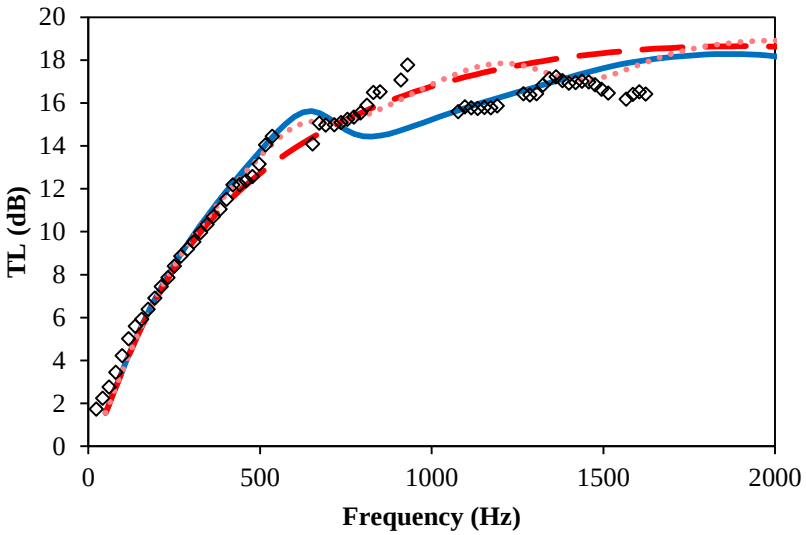

Figure 45: Experimental and model TL for MC1 at 2.8 MPa, 26 C. ◇ Reduced experimental data; — Original model; — — Bulk modulus model; ▪ ▪ Non-shear model.

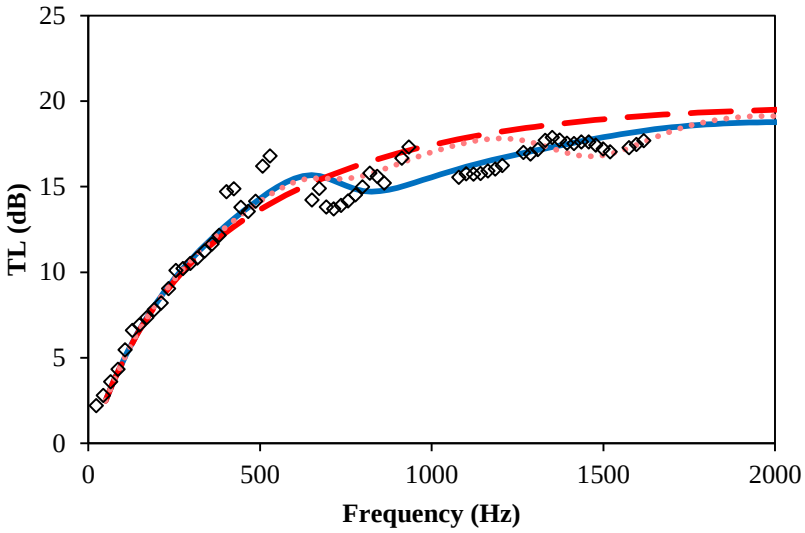

Figure 46: Experimental and model TL for MC2 v1 at 2.8 MPa, 26 C. ◇ Reduced experimental data; — Original model; — — Bulk modulus model; ▪ ▪ Non-shear model.

Overall, both model simplifications approximately match or improve on the original model predictions for certain cases. The non-shear model captures some of the low frequency resonances that the bulk modulus model does not, but in these cases it also tends to generate significant higher frequency resonances which match neither the original model nor the experimental data. The bulk modulus model does not capture all of the finer details of the original model, but it has the simplicity of relying on only a single modulus, and performs sufficiently well for the vast majority of the cases that it should have significant utility for preliminary predictive purposes.

6.3 Optimization

While the current set of syntactic foam samples has been shown to effectively reduce noise in the frequency ranges of interest for many hydraulic systems, the nominal critical pressures for both sets of microspheres are less than 2.5 MPa, while typical working pressures for hydraulic systems may be on the order of 20 to 35 MPa. As shown

in Equation (5.5), critical pressures can be increased by changing the microsphere material properties, decreasing their radius, or increasing their wall thickness. These higher pressure microspheres are not currently available off the shelf; the optimizations in this section are meant to show whether there is utility in developing such microspheres for noise control use.

6.3.1 Optimization objective

For this optimization exercise, it is desired to reduce hydraulic noise for a particular task using a mobile hydraulically actuated excavator. Gruber[78] has done some work optimizing sets of pressurized hydraulic noise suppressors, such as those discussed in Chapter 7, for excavator work cycles, and has published some experimental noise measurements from Eaton Corporation to use as reference values. Some of his data are utilized for the present optimization, in which it is desired to reduce the noise in the boom actuation subsystem during a particular operation.

The typical noise profiles of the pumping system in question are available at four pressures: 3.4, 6.9, 13.8, and 20.7 MPa (500, 1000, 2000, and 3000 psi); and are shown in Figure 47, normalized to a maximum pressure value of unity for the entire measured range of 10 to 5100 Hz. A subset of these data are examined in dB scale (normalized so unity pressure equals 0 dB) in Figure 48. Here the data are viewed in 200 Hz bands centered from 100 to 1500 Hz, and looking only at the values above -50 dB. It is clearly seen in the figure that the majority of the excitation occurs below 500 Hz. To further clarify the excitation, the combined levels for several frequency bands are shown in Table 16, using the same normalized levels. Here it is seen that the highest overall levels are

clearly experienced at the highest two system pressures, and any noise contributions in the frequencies above 2000 Hz are negligible.

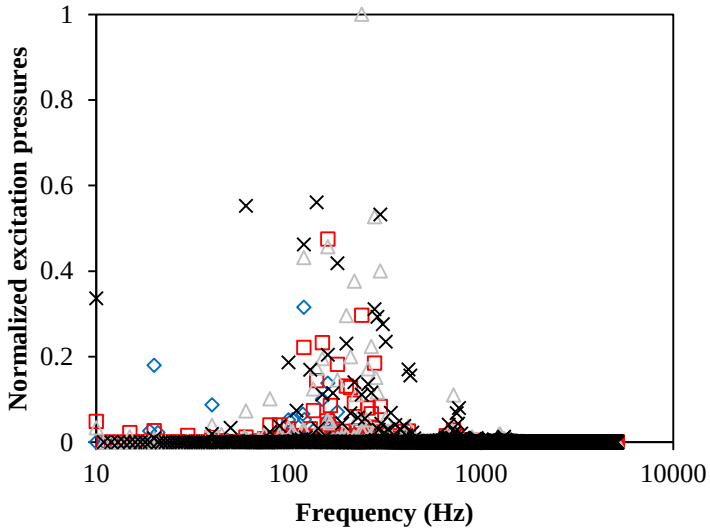

Figure 47: Linear excitation pressure values, normalized to unity. System pressures: ◇ 3.4 MPa; □ 6.9 MPa; △ 13.8 MPa; × 20.7 MPa.

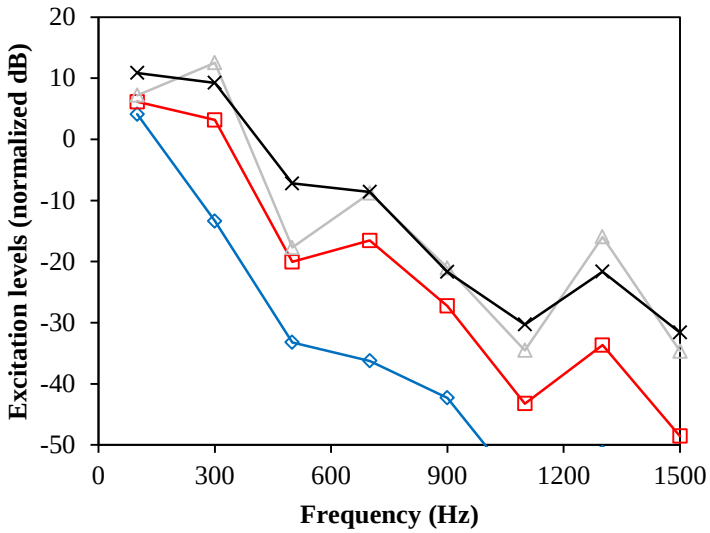

Figure 48: Excitation levels at each frequency, limited to highest amplitude values. System pressures: ◇ 3.4 MPa; □ 6.9 MPa; △ 13.8 MPa; × 20.7 MPa.

Table 16: Frequency band levels of noise excitation.

Pressure (MPa)	Levels (normalized dB)			
	10-500 Hz	500-2000 Hz	2000-5100 Hz	10-5100 Hz (Total)
3.4	5.29	-30.23	-68.45	5.43
6.9	11.02	-12.63	-55.45	11.58
13.8	16.45	-3.41	-44.31	17.30
20.7	16.67	-4.06	-42.00	17.44

The working pressures of the actual excavator versus time are continuous. The average data for a run are discretized into pressure bins with a resolution of 0.7 MPa (100 psi), as shown in Figure 49 for a back-filling task, where the sum of all the time fraction values is unity.

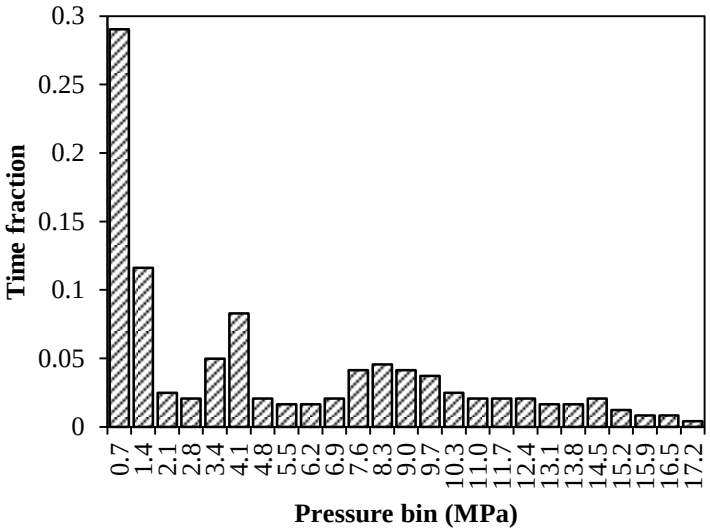

Figure 49: Time fraction of boom subsystem at each pressure, back-filling task (bins of 0.7 MPa)

Comparing Figure 49 to Table 16, it is obvious that representative noise profiles are not provided for the entire set of system pressures. To correlate the entire range of pressures and frequencies, several approximations are made. First, noise profiles are created for 10.3 and 17.2 MPa (1500 and 2500 psi) by interpolating the linear pressure values. The pressure values for the time fractions are also consolidated into bins centered

at 3.4, 6.9, 10.3, 13.8, and 17.2 MPa. Each of the original values is aggregated into the nearest consolidated bin, except for values below 1.7 MPa, which are considered "idle time" with negligible contribution to the noise profile. Notably, there is no 20.7 MPa pressure bin, as the maximum pressures measured for this work profile are below that value. The time weights are re-normalized such that their sum is again unity, and the resulting time-pressure correlation is shown in Figure 50.

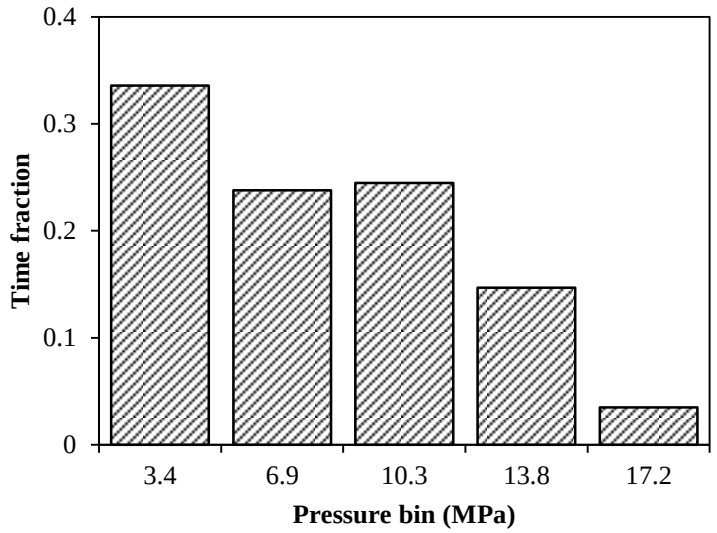

Figure 50: Time fraction of boom subsystem at each condensed pressure, back-filling task (bins of 3.4 MPa).

Since this profile is weighted largely toward low pressures, two other time profiles are considered. The condensed profile for a trenching task is shown in Figure 51, while for an arbitrary equal time weight task, all five time weights are 0.2.

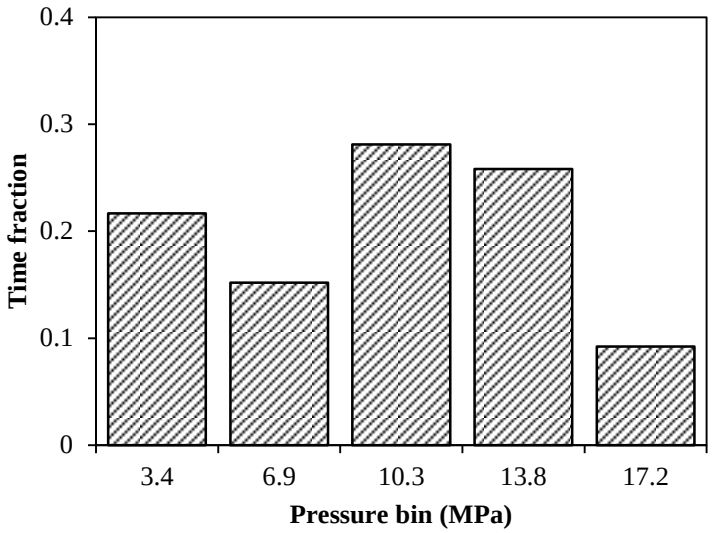

Figure 51: Time fraction of boom subsystem at each condensed pressure, trenching task (bins of 3.4 MPa).

With the excitations defined, an objective function for the optimization can now be discussed. In the several optimizations to follow, the objective function F to be minimized is

$$F\left(\vec{\alpha}\right)=\sum_{m=1}^{M}T_m\left[L_{P2,m}\left(\vec{\alpha}\right)-L_{P1,m}\right], \tag{6.4}$$

where $\vec{\alpha}$ is the vector of optimization input parameters, to be defined later; M = 5 is the number of pressures being considered; T_m is the time fraction of each pressure as shown, for example, in Figure 50; $L_{P1,m}$ is the overall excitation level at each system pressure; and $L_{P2,m}\left(\vec{\alpha}\right)$ is the reduced level at each pressure after transmission loss is considered. Letting P_{mn} be the (normalized) pressure amplitude of the excitation at system pressure number m and frequency number n out of N, and likewise $\mathrm{TL}_{mn}\left(\vec{\alpha}\right)$ the transmission loss in dB at the same pressure and frequency, the levels may be defined as

$$L_{P1,m}=20\log_{10}\left(\sum_{n=1}^{N}10^{L_{1,mn}/20}\right), \tag{6.5}$$

$$L_{P2,m}\left(\vec{\alpha}\right) = 20\log_{10}\left(\sum_{n=1}^{N} 10^{L_{2,mn}(\vec{\alpha})/20}\right), \tag{6.6}$$

$$L_{P1,mn} = 20\log_{10}\left(P_{mn}\right), \tag{6.7}$$

$$L_{P2,mn}\left(\vec{\alpha}\right) = L_{1,mn} - \mathrm{TL}_{mn}\left(\vec{\alpha}\right). \tag{6.8}$$

In this way, the negative of the objective function represents the time-weighted overall transmission loss of the system, so the optimization maximizes a time-weighted transmission loss over the grouped operating pressure conditions. For the analyses to follow, the upper frequency limit of interest will be 2000 Hz, since the excitation sound power above this limit is negligible.

6.3.2 Material model and constraints

To simplify the optimization to a tractable level, it is necessary to make some assumptions and simplifications with regards to the material model used. The theoretical material used in this optimization will follow the procedure outlined in Section 5.2.1 for the determination of bulk modulus, and the bulk modulus model in Section 6.2.1 to estimate transmission loss.

Static bulk modulus K_0 depends on the host polymer, as well as the P_{cr} distribution of the microspheres. The manufacturer of the prototype liners indicated that a microsphere volume fraction of 0.4 was approximately the highest value that could be cast without difficulty in degassing, so this is assumed to be the volume fraction for all optimized liners. Two different P_{cr} distributions are considered.

In Optimization 1, the distribution of $\log_{10}(P_{cr})$ is considered to be normal, as in Section 5.2. The optimization parameter vector $\vec{\alpha}$ consists of $\alpha_1 = P_{cr0}$ and $\alpha_2 = \sigma_s$. P_{cr0} is allowed to vary between 3.4 and 20.7 MPa, and σ_s between 0.01 and 0.3

Optimization 2 is like Optimization 1, except that two distributions of microspheres are used. The parameter vector $\vec{\alpha}$ now consists of four values, which are in order: $P_{cr0,1}$, $P_{cr0,2}$, σ_1, and σ_2. Equation (5.10) is modified to be

$$a = a_0\left(F_{P0}\mathrm{e}^{-\frac{P_s}{K_P}} + F_{G0}\left(\frac{P_{atm}}{P_{tot}}\right) + \sum_{i=1}^{2} F_{U0,i}\left(G_{U,i}\mathrm{e}^{-\frac{P_s}{K_U}} + G_{B,i}F_H\mathrm{e}^{-\frac{P_s}{K_H}} + G_{B,i}\left(1-F_H\right)\left(\frac{P_{atm}}{P_{tot}}\right)\right)\right)^{\frac{1}{3}}, \qquad (6.9)$$

and Equations (5.8) and (5.15) are calculated for each set of $G_{U,i}$, $G_{B,i}$, and $\sigma_{s,i}$. The two populations of microspheres are both assumed to have the same initial volume fraction $F_{U0,1} = F_{U0,2} = 0.2$, and equal F_H, as discussed below.

For these optimizations, $K_P = K_U = K_H = 400$ MPa is taken as an arbitrary value representative of MA and MB, and $F_{G0} = 0$. Three different values of F_H are considered in these optimizations. As a best-case scenario, $F_H = 0$ is used. Since these spheres are expected to buckle at much higher pressures than those used in the current generation of liners, $F_H = 0.32$ is used as calculated for MB2, as well as $F_H = 0.5$, to illustrate the effects of thicker shells. Of course, different microsphere shell materials will also affect the needed shell thickness; the range of values used here is meant to be illustrative.

In all optimizations, K_0 is found as K in Equation (5.19) by applying a small ΔP to the model and numerically calculating the differential a value. Since no exact models are known, dynamic K is estimated based on observed trends in Chapter 5. For a given static K_0 and f in Hz, they are

$$K'(f) = K_0\left(1 + \frac{0.2875}{1000}f\right) \qquad (6.10)$$

$$K''(f) = K'(f)\left(0.13 - \frac{0.0225}{1000}f\right). \qquad (6.11)$$

6.3.3 Optimization results

As with the optimizations in Chapter 4 and Chapter 5, a simulated annealing solution method is used. The resulting optimization parameters and objective function values are summarized in Table 17 for the back fill task, in Table 18 for the trenching task, and in Table 19 for the equal time weight case. In each case, it can be seen that the optimization with two sets of microspheres generates a lower objective function by about 1 dB (highlighted cells), and the minimum objective function increases as F_H increases; these results are as expected. It may also be noted that within a single task and optimization type, the optimization parameters do not generally change much based on the F_H value. A significant reason for performing these optimizations is to compare the current type of suppressor to competing technologies. This is done in Chapter 7, and discussion of this comparison is saved for Section 7.5

Table 17: Optimization results for back fill task. Type 2 optimization results with lower objective functions for each F_H are highlighted.

Optimization type	F_H	$P_{cr0,1}$ (MPa)	$P_{cr0,2}$ (MPa)	$\sigma_{s,1}$	$\sigma_{s,2}$	Objective function value (dB)
1	0	6.70	-	0.039	-	-19.57
2	0	4.18	10.50	0.023	0.019	-20.47
1	0.32	6.70	-	0.038	-	-17.12
2	0.32	3.55	9.62	0.010	0.020	-19.84
1	0.5	6.66	-	0.038	-	-15.31
2	0.5	3.90	9.74	0.020	0.019	-16.30

Table 18: Optimization results for trenching task. Type 2 optimization results with lower objective functions for each F_H are highlighted.

Optimization type	F_H	$P_{cr0,1}$ (MPa)	$P_{cr0,2}$ (MPa)	$\sigma_{s,1}$	$\sigma_{s,2}$	Objective function value (dB)
1	0	8.80	-	0.038	-	-18.74
2	0	5.33	12.72	0.033	0.013	-20.00
1	0.32	11.19	-	0.020	-	-16.34
2	0.32	5.31	12.51	0.032	0.013	-17.67
1	0.5	9.15	-	0.036	-	-14.72
2	0.5	5.68	12.40	0.035	0.012	-15.86

Table 19: Optimization results for equal time weight case. Type 2 optimization results with lower objective functions for each F_H are highlighted.

Optimization type	F_H	$P_{cr0,1}$ (MPa)	$P_{cr0,2}$ (MPa)	$\sigma_{s,1}$	$\sigma_{s,2}$	Objective function value (dB)
1	0	9.04	-	0.040	-	-18.20
2	0	7.07	14.14	0.036	0.013	-19.02
1	0.32	9.20	-	0.038	-	-15.95
2	0.32	5.90	13.85	0.033	0.014	-16.79
1	0.5	9.20	-	0.038	-	-14.27
2	0.5	6.08	13.92	0.033	0.014	-15.01

Figure 52 shows the simulated radial compression of both optimization solutions for the back fill task, $F_H = 0$, in a similar style to Figure 14 through Figure 18. Figure 53 shows the corresponding K_0. Comparing Optimization 1 to Optimization 2, the compression curves and K_0 estimates are very similar, but Optimization 2 achieves about a 1 dB marginal improvement by having a slightly lower K_0 at the center values of the 3.4, 10.3, and 13.8 MPa pressure bins. If the optimization were performed over many more discrete pressures to better simulate a continuous operating range, it might be the case that having two sets of microspheres would have even less of an advantage; but if the operating pressure range were wider or more concentrated into specific pressure ranges, the two-population method might prove more beneficial. Compositions with two

sets of microspheres might be especially useful in a system with high and low pressure modes where the pressures are significantly different. In this case, a material could be designed, using a small buckling pressure standard deviation, to be compressible mainly at those two pressures, while staying relatively stiff at the intermediate pressures. This concept could theoretically be extended to a system with any discrete number of working pressures, using an equal number of microsphere populations.

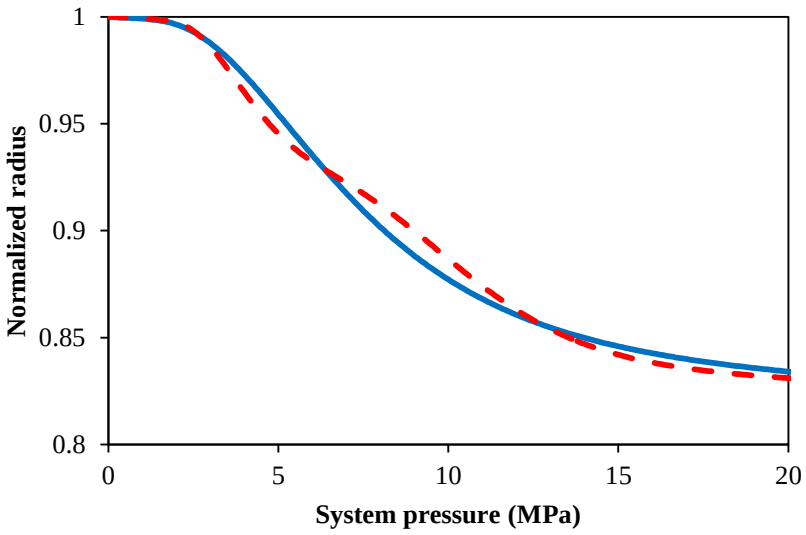

Figure 52: Simulated radial compression of optimized liner inserts, back fill task, $F_H = 0$. — Optimization 1; - - - Optimization 2.

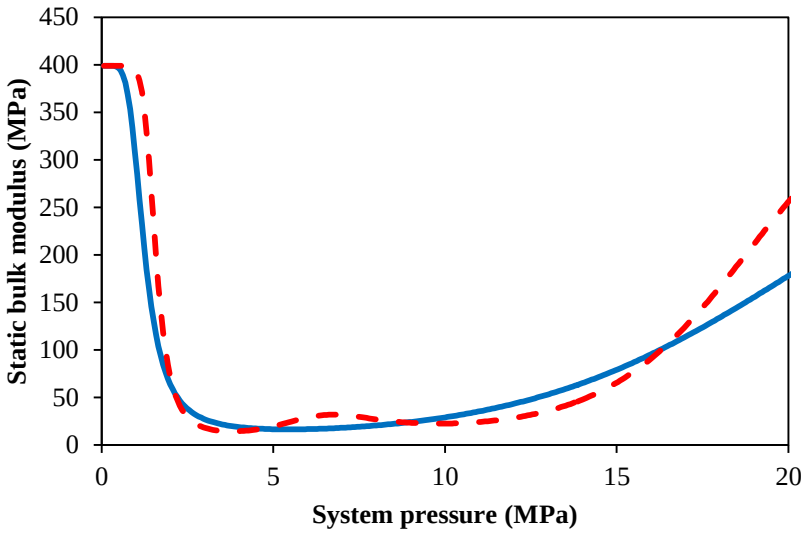

Figure 53: Static bulk modulus K_0 of optimized liner inserts, back fill task, $F_H = 0$. — Optimization 1; – – Optimization 2.

6.3.4 Comparison to two modulus model

While it has been shown that the bulk modulus model gives similar or improved matches to experimental data compared to the original model, it is helpful to also make a check with regards to the optimized models as well. This analysis is performed for Optimizations 1 and 2 of the back fill task, $F_H = 0$. For this analysis, the optimized bulk moduli are separated into λ and μ values using the μ value for MA1 at 53 C, as was used in Chapter 5, and then finding λ with Equation (6.1). The objective function is calculated for the original model, and the resulting values are compared to the bulk modulus model values in Table 20. The results show that the original model indicates a slightly worse objective function, but values differ by about 1.5 dB or less

Table 20: Comparison of optimization results (back fill task, $F_H = 0$) using original and bulk modulus models.

	Bulk modulus model objective function (dB)	Original model objective function (dB)
Optimization 1	-19.57	-18.04
Optimization 2	-20.47	-19.47

To further illuminate the comparison, TL predictions for both the bulk modulus and the full two modulus models are shown for three pressures with the material properties determined for Optimization 2. At the lowest simulated pressure, 3.4 MPa, there is significant deviation in the TL predictions over the frequency range of interest, as seen in Figure 54; however, they are very similar at the lowest frequencies, where much of the excitation lies. At the next highest pressure of 6.9 MPa, the two TL curves are largely converged in an average sense, with variations due to low-bandwidth resonances. This is shown in Figure 55. As the pressure increases, the two curves generally continue to converge; this is illustrated for 13.8 MPa in Figure 56. The static bulk modulus values, along with the 10 Hz values for λ' and μ', are shown in Table 21. Qualitatively, it is expected that higher λ with respect to μ will result in greater agreement between the two models, so it is unsurprising that at the lowest system pressure, where λ' is lowest, the discrepancy is greatest. Damping is also a factor in this comparison. Higher damping reduces the amplitude of resonances and anti-resonances, such that the difference between the two models will be expected to be smaller. In these models, both the values of μ' and of damping in general are only roughly estimated, so it is possible that the results from a physical system would be somewhat better or worse than what is predicted here. Additionally, the effects of temperature variations are not considered in these optimizations. However, these optimizations do clearly show that significant noise

reduction would be possible with microspheres utilizing an appropriate range of critical buckling pressures.

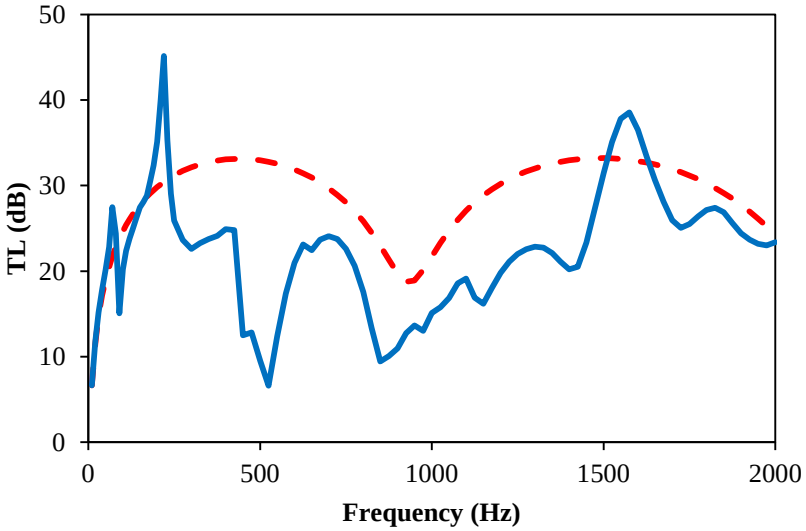

Figure 54: Model comparison for back fill task, F_H = 0, Optimization 2 results at 3.4 MPa system pressure. — Original model; - - - Bulk modulus model.

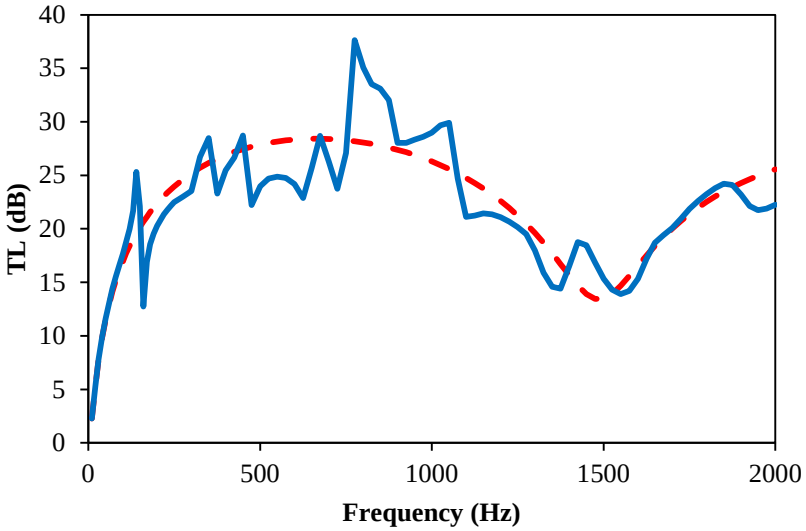

Figure 55: Model comparison for back fill task, F_H = 0,Optimization 2 results at 6.9 MPa system pressure. — Original model; - - - Bulk modulus model.

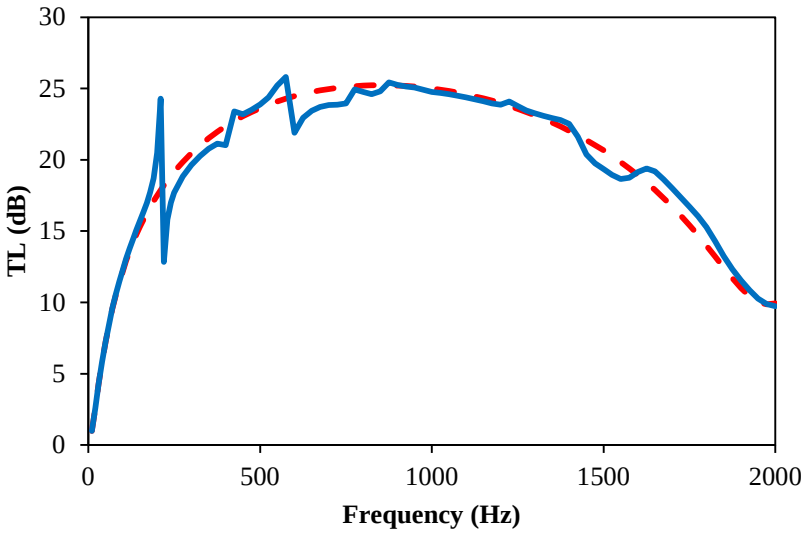

Figure 56: Model comparison for back fill task, F_H = 0, Optimization 2 results at 13.8 MPa system pressure. ━ Original model; ━ ━ Bulk modulus model.

Table 21: Modulus values for back fill task, F_H = 0, Optimization 2.

System pressure (MPa)	K_0 (MPa)	Re(λ(10 Hz)) (MPa)	Re(μ(10 Hz)) (MPa)
3.4	15.0	12.6	3.6
6.9	31.8	29.4	3.6
10.3	22.8	20.5	3.6
13.8	44.9	42.6	3.6
17.2	133.8	131.8	3.6

6.4 Summary

In this chapter, it is shown that the model presented in Chapter 4 can be simplified considerably by using only the bulk modulus rather than considering the separate effects of λ and μ. While this simplified model does not capture all the resonance behavior of the system, it provides TL predictions sufficiently close to experimental data to be used to preliminary design analyses. In the second part of this chapter, the bulk modulus model is used to optimize the design of a future syntactic foam insert, based on the buckling pressure distribution of the microspheres, as introduced in Chapter 5. An optimization method is developed, and implemented for two specific excavator work cycles and an

arbitrary cycle with uniform system pressure distribution. The best optimization results give an estimated time-weighted reduction of about 20 dB for the fluid-borne noise in the boom actuation subsystem, and this value is validated using the full two modulus model. While more development is needed in the physical production of microspheres, the optimization shows that significant noise reduction can be achieved if such materials are made available.

CHAPTER 7

ANALYSIS OF BLADDER STYLE SUPPRESSOR

While the syntactic foam lined suppressors are the main focus of this thesis, an understanding of currently available devices is desirable as well. One reason for this is that the available bladder style devices are, like the prototype devices already discussed, not well modeled in the literature; thus, modeling work will be useful for a designer wishing to use these devices in the present. Additionally, the modeling and experimental work contained in this chapter are needed to compare the effectiveness of the new devices to what is already available, thereby allowing judgments to be made of the current and any future prototype devices.

7.1 Model geometry

The various components of the suppressor under consideration are shown in Figure 57. There is an inner cylindrical flow path; the hydraulic fluid reaches an outer chamber through a coarse perforation layer, a spacer in the form of a compression spring, and a thin, finely perforated layer. Outside the perforated section, a rubber bladder separates the hydraulic fluid from the pressurized nitrogen gas in the outermost section of the chamber. The thin perforate layer and rubber bladder are shown removed from the main assembly in part (a) of the figure; the spring separator is omitted in part (b). Dimension labels are shown in Figure 58. The inlet and outlet pipe radius is r_0. The length of the suppressor is L plus inlet and outlet extension lengths L_1 and L_2. When the bladder is precharged to pressure P_c but the hydraulic system is unpressurized, the gas expands so that the bladder reaches the thin perforate layer at r_1; when the hydraulic

system is pressurized to P_s, the gas compresses further and is constrained between the rigid outer shell at r_2 and the rubber bladder at r_3.

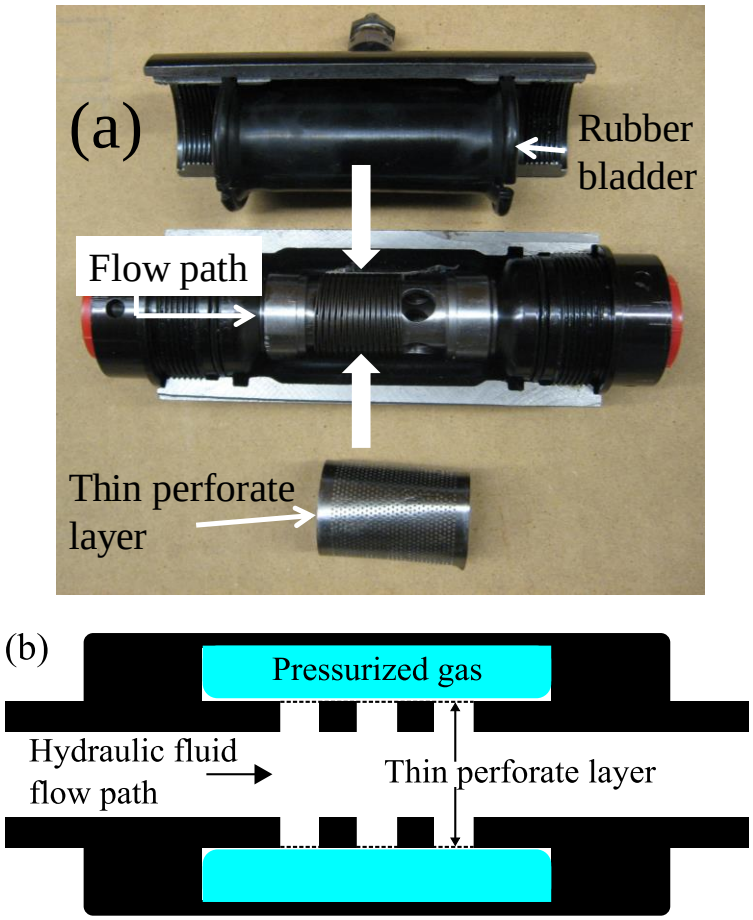

Figure 57: Suppressor features. (a) Photograph of device cross section with thin perforate layer and rubber bladder removed from main body; (b) Modeling diagram, showing thin perforate layer and bladder in place

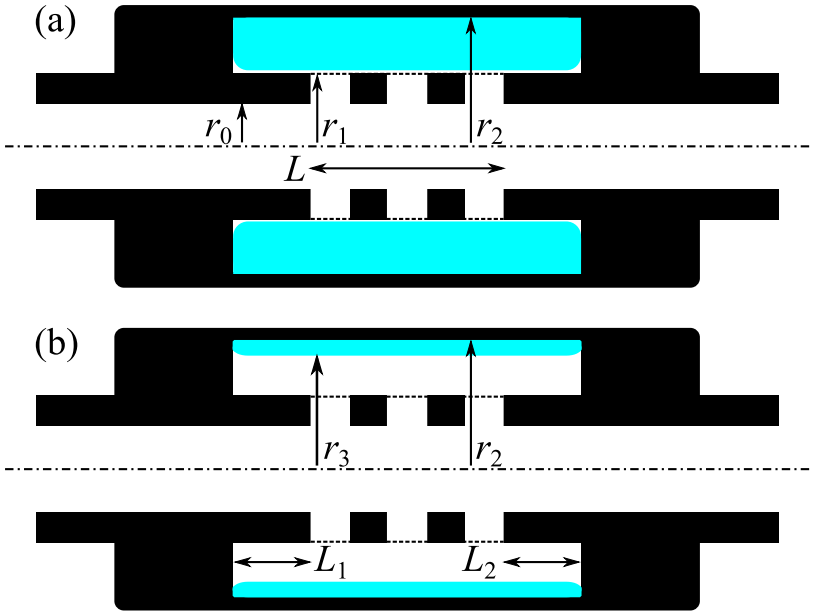

Figure 58: Suppressor geometry with dimensions for (a) unpressurized system, (b) pressurized system. When the system is not pressurized, the bladder is pushed against the thin perforate layer at r_1; when system pressure is applied, the bladder moves to equilibrium at r_3.

Bladder radius r_3 is determined by the suppressor geometry, as well as charge and system pressures P_c and P_s. When the bladder is precharged with nitrogen, the gas volume is known to be

$$V_0 = \pi L_T \left(r_2^2 - r_1^2 \right), \tag{7.1}$$

$$L_T = L + L_1 + L_2 . \tag{7.2}$$

The mass of the nitrogen is found using the ideal gas law

$$m = \frac{MPV_0}{RT_0}, \tag{7.3}$$

for molar mass M, temperature T_0 in Kelvins, and universal gas constant R. At full system pressure P_s and working temperature T, the nitrogen mass remains constant, and the bladder radius is found by solving

$$V = \frac{mRT}{MP_s} = \pi L_T \left(r_2^2 - r_3^2 \right), \tag{7.4}$$

from which r_3, the bladder radius, may be found. For this analysis to be valid, P_s must be greater than P_c.

The density ρ_f and sound speed c_f in the hydraulic fluid are assumed to be known and not to change with varying pressure or temperature. Additionally, the bladder at r_3 is treated as a limp mass sheet with sheet density σ_b calculated from the bladder mass, length, and diameter at P_s. For bladder mass m_b distributed evenly over length L_T,

$$\sigma_b = \frac{m_b}{2\pi r_3 L_T}. \tag{7.5}$$

7.2 Acoustic propagation model

For modeling purposes, the suppressor is divided into three axial regions, as shown in Figure 59. Region 1 includes the upstream (1*U*) and downstream (1*D*) pipes; region 2 represents the main body of the suppressor section, including the main hydraulic fluid flow path as well as the thin perforate layer, rubber bladder, and compressed nitrogen gas; and region 3 contains the upstream (3*U*) and downstream (3*D*) extension sections, including hydraulic fluid, rubber bladder, and compressed nitrogen layers. In general, the regions are referred to by number, with the *U* or *D* added only if the quantity differs between the upstream and downstream portions. The axial references $x = 0$ and $x = L$ are also shown, with the positive *x* direction facing right. As illustrated in Figure 60, each region *R* has forward and reverse travelling modes with unique modal amplitudes $A_{R,n}$ and $B_{R,n}$ for *N* modes, where *n* = 0 to *N*-1. For waves in regions 1*U*, 2, and 3*U*, modal amplitudes represent their values at $x = 0$; for regions 1*D* and 3*D*, they are found at $x = L$.

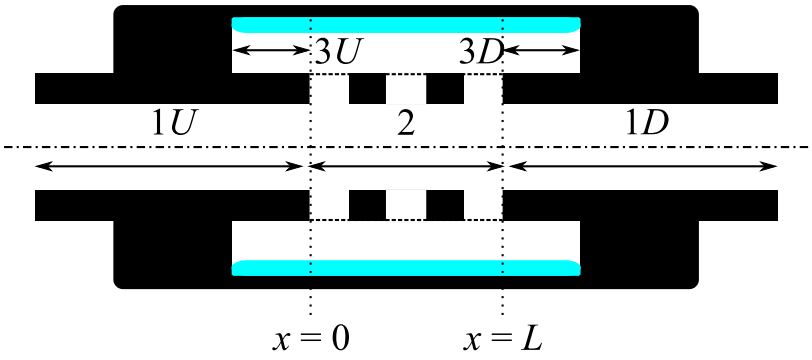

Figure 59: Model geometry with region labels

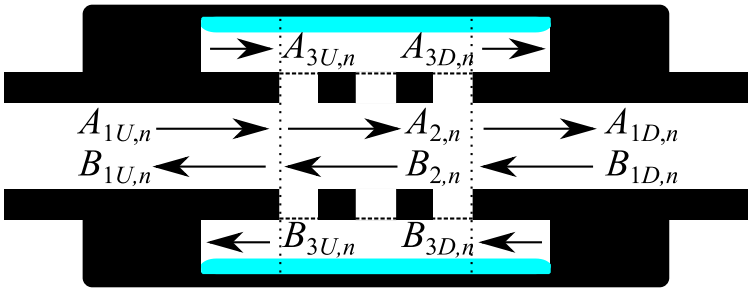

Figure 60: Model geometry with wave pressure amplitude labels

The elasticity of the hydraulic fluid and nitrogen gas (liner) are represented by Lamé parameters λ_f and λ_L, respectively. Shear moduli μ_f and μ_L are both zero for these materials, thus making λ_f and λ_L equivalent to the bulk moduli of the propagation media. This also means that only longitudinal waves will propagate in the suppressor. Sound speeds are defined as

$$c_f = \sqrt{\frac{\lambda_f}{\rho_f}}, \tag{7.6}$$

$$c_L = \sqrt{\frac{\lambda_L}{\rho_L}}, \tag{7.7}$$

and for angular frequency ω, wavenumbers k are defined as

$$k_f = \frac{\omega}{c_f}, \quad k_L = \frac{\omega}{c_L}. \tag{7.8}$$

For each propagation mode n and region R, the wavenumbers may be decomposed into axial and radial components, represented by subscripts x and r. These relate to the wavenumbers by

$$k_f^2 = k_{Rx,n}^2 + k_{Rrf,n}^2, \tag{7.9}$$

$$k_L^2 = k_{Rx,n}^2 + k_{RrL,n}^2. \tag{7.10}$$

Notably, in the suppressor, the axial wavenumber is the same in the hydraulic fluid as in the nitrogen, while the radial wavenumber differs in general, resulting in an additional subscript f or L to denote the medium. The acoustic displacements $u_{Rr,n}$ and $u_{Rx,n}$ in the radial and axial directions, respectively, are for the forward travelling modes:

$$u_{1Ur,n} = -k_{1rf,n} J_1\left(k_{1rf,n} r\right) A_{1U,n}\, \mathrm{e}^{-\mathrm{i}k_{1x,n}x}\, \mathrm{e}^{\mathrm{i}\omega t}, \tag{7.11}$$

$$u_{1Dr,n} = -k_{1rf,n} J_1\left(k_{1rf,n} r\right) A_{1D,n}\, \mathrm{e}^{-\mathrm{i}k_{1x,n}x'}\, \mathrm{e}^{\mathrm{i}\omega t}, \tag{7.12}$$

$$u_{2r,n} = \begin{cases} -k_{2rf,n} y_{1,n} J_1\left(k_{2rf,n} r\right) A_{2,n}\, \mathrm{e}^{-\mathrm{i}k_{2x,n}x}\, \mathrm{e}^{\mathrm{i}\omega t}, & r < r_1 \\ -k_{2rf,n}\left(y_{2,n} J_1\left(k_{2rf,n} r\right) + y_{3,n} Y_1\left(k_{2rf,n} r\right)\right) A_{2,n}\, \mathrm{e}^{-\mathrm{i}k_{2x,n}x}\, \mathrm{e}^{\mathrm{i}\omega t}, & r_1 \le r < r_3 \\ -k_{2rL,n}\left(y_{4,n} J_1\left(k_{2rL,n} r\right) + y_{5,n} Y_1\left(k_{2rL,n} r\right)\right) A_{2,n}\, \mathrm{e}^{-\mathrm{i}k_{2x,n}x}\, \mathrm{e}^{\mathrm{i}\omega t}, & r \ge r_3 \end{cases}, \tag{7.13}$$

$$u_{3Ur,n} = \begin{cases} -k_{3rf,n}\left(y_{6,n} J_1\left(k_{3rf,n} r\right) + y_{7,n} Y_1\left(k_{3rf,n} r\right)\right) A_{3U,n}\, \mathrm{e}^{-\mathrm{i}k_{3x,n}x}\, \mathrm{e}^{\mathrm{i}\omega t}, & r < r_3 \\ -k_{3rL,n}\left(y_{8,n} J_1\left(k_{3rL,n} r\right) + y_{9,n} Y_1\left(k_{3rL,n} r\right)\right) A_{3U,n}\, \mathrm{e}^{-\mathrm{i}k_{3x,n}x}\, \mathrm{e}^{\mathrm{i}\omega t}, & r \ge r_3 \end{cases}, \tag{7.14}$$

$$u_{3Dr,n} = \begin{cases} -k_{3rf,n}\left(y_{6,n} J_1\left(k_{3rf,n} r\right) + y_{7,n} Y_1\left(k_{3rf,n} r\right)\right) A_{3D,n}\, \mathrm{e}^{-\mathrm{i}k_{3x,n}x'}\, \mathrm{e}^{\mathrm{i}\omega t}, & r < r_3 \\ -k_{3rL,n}\left(y_{8,n} J_1\left(k_{3rL,n} r\right) + y_{9,n} Y_1\left(k_{3rL,n} r\right)\right) A_{3D,n}\, \mathrm{e}^{-\mathrm{i}k_{3x,n}x'}\, \mathrm{e}^{\mathrm{i}\omega t}, & r \ge r_3 \end{cases}, \tag{7.15}$$

$$u_{1Ux,n} = -\mathrm{i}k_{1x,n} J_0\left(k_{1rf,n} r\right) A_{1U,n}\, \mathrm{e}^{-\mathrm{i}k_{1x,n}x}\, \mathrm{e}^{\mathrm{i}\omega t}, \tag{7.16}$$

$$u_{1Dx,n} = -\mathrm{i}k_{1x,n} J_0\left(k_{1rf,n} r\right) A_{1D,n}\, \mathrm{e}^{-\mathrm{i}k_{1x,n}x'}\, \mathrm{e}^{\mathrm{i}\omega t}, \tag{7.17}$$

$$u_{2x,n}=\begin{cases}-\mathrm{i}k_{2x,n}y_{1,n}J_0\left(k_{2rf,n}r\right)A_{2,n}\,\mathrm{e}^{-\mathrm{i}k_{2x,n}x}\,\mathrm{e}^{\mathrm{i}\omega t},\ r<r_1\\ -\mathrm{i}k_{2x,n}\left(y_{2,n}J_0\left(k_{2rf,n}r\right)+y_{3,n}Y_0\left(k_{2rf,n}r\right)\right)A_{2,n}\,\mathrm{e}^{-\mathrm{i}k_{2x,n}x}\,\mathrm{e}^{\mathrm{i}\omega t},\ r_1\le r<r_3\\ -\mathrm{i}k_{2x,n}\left(y_{4,n}J_0\left(k_{2rL,n}r\right)+y_{5,n}Y_0\left(k_{2rL,n}r\right)\right)A_{2,n}\,\mathrm{e}^{-\mathrm{i}k_{2x,n}x}\,\mathrm{e}^{\mathrm{i}\omega t},\ r\ge r_3\end{cases}, \tag{7.18}$$

$$u_{3Ux,n}=\begin{cases}-\mathrm{i}k_{3x,n}\left(y_{6,n}J_0\left(k_{3rf,n}r\right)+y_{7,n}Y_0\left(k_{3rf,n}r\right)\right)A_{3U,n}\,\mathrm{e}^{-\mathrm{i}k_{3x,n}x}\,\mathrm{e}^{\mathrm{i}\omega t},\ r<r_3\\ -\mathrm{i}k_{3x,n}\left(y_{8,n}J_0\left(k_{3rL,n}r\right)+y_{9,n}Y_0\left(k_{3rL,n}r\right)\right)A_{3U,n}\,\mathrm{e}^{-\mathrm{i}k_{3x,n}x}\,\mathrm{e}^{\mathrm{i}\omega t},\ r\ge r_3\end{cases}, \tag{7.19}$$

$$u_{3Dx,n}=\begin{cases}-\mathrm{i}k_{3x,n}\left(y_{6,n}J_0\left(k_{3rf,n}r\right)+y_{7,n}Y_0\left(k_{3rf,n}r\right)\right)A_{3D,n}\,\mathrm{e}^{-\mathrm{i}k_{3x,n}x'}\,\mathrm{e}^{\mathrm{i}\omega t},\ r<r_3\\ -\mathrm{i}k_{3x,n}\left(y_{8,n}J_0\left(k_{3rL,n}r\right)+y_{9,n}Y_0\left(k_{3rL,n}r\right)\right)A_{3D,n}\,\mathrm{e}^{-\mathrm{i}k_{3x,n}x'}\,\mathrm{e}^{\mathrm{i}\omega t},\ r\ge r_3\end{cases}, \tag{7.20}$$

where J_m and Y_m are m^{th} order Bessel functions of the first and second kind, relative complex amplitudes of coefficients $y_{1,n}$ to $y_{5,n}$ and $y_{6,n}$ to $y_{9,n}$ are unique for each mode n in regions 2 and 3, and $x'=x-L$. Similarly, acoustic pressures $p_{R,n}$ are:

$$p_{1U,n}=k_f^2\lambda_f J_0\left(k_{1rf,n}r\right)A_{1U,n}\,\mathrm{e}^{-\mathrm{i}k_{1x,n}x}\,\mathrm{e}^{\mathrm{i}\omega t}, \tag{7.21}$$

$$p_{1D,n}=k_f^2\lambda_f J_0\left(k_{1rf,n}r\right)A_{1D,n}\,\mathrm{e}^{-\mathrm{i}k_{1x,n}x'}\,\mathrm{e}^{\mathrm{i}\omega t}, \tag{7.22}$$

$$p_{2,n}=\begin{cases}k_f^2\lambda_f y_{1,n}J_0\left(k_{2rf,n}r\right)A_{2,n}\,\mathrm{e}^{-\mathrm{i}k_{2x,n}x}\,\mathrm{e}^{\mathrm{i}\omega t},\ r<r_1\\ k_f^2\lambda_f\left(y_{2,n}J_0\left(k_{2rf,n}r\right)+y_{3,n}Y_0\left(k_{2rf,n}r\right)\right)A_{2,n}\,\mathrm{e}^{-\mathrm{i}k_{2x,n}x}\,\mathrm{e}^{\mathrm{i}\omega t},\ r_1\le r<r_3\\ k_L^2\lambda_L\left(y_{4,n}J_0\left(k_{2rL,n}r\right)+y_{5,n}Y_0\left(k_{2rL,n}r\right)\right)A_{2,n}\,\mathrm{e}^{-\mathrm{i}k_{2x,n}x}\,\mathrm{e}^{\mathrm{i}\omega t},\ r\ge r_3\end{cases}, \tag{7.23}$$

$$p_{3U,n}=\begin{cases}k_f^2\lambda_f\left(y_{6,n}J_0\left(k_{3rf,n}r\right)+y_{7,n}Y_0\left(k_{3rf,n}r\right)\right)A_{3U,n}\,\mathrm{e}^{-\mathrm{i}k_{3x,n}x}\,\mathrm{e}^{\mathrm{i}\omega t},\ r<r_3\\ k_L^2\lambda_L\left(y_{8,n}J_0\left(k_{3rL,n}r\right)+y_{9,n}Y_0\left(k_{3rL,n}r\right)\right)A_{3U,n}\,\mathrm{e}^{-\mathrm{i}k_{3x,n}x}\,\mathrm{e}^{\mathrm{i}\omega t},\ r\ge r_3\end{cases}, \tag{7.24}$$

$$p_{3D,n}=\begin{cases}k_f^2\lambda_f\left(y_{6,n}J_0\left(k_{3rf,n}r\right)+y_{7,n}Y_0\left(k_{3rf,n}r\right)\right)A_{3D,n}\,\mathrm{e}^{-\mathrm{i}k_{3x,n}x'}\,\mathrm{e}^{\mathrm{i}\omega t},\ r<r_3\\ k_L^2\lambda_L\left(y_{8,n}J_0\left(k_{3rL,n}r\right)+y_{9,n}Y_0\left(k_{3rL,n}r\right)\right)A_{3D,n}\,\mathrm{e}^{-\mathrm{i}k_{3x,n}x'}\,\mathrm{e}^{\mathrm{i}\omega t},\ r\ge r_3\end{cases}. \tag{7.25}$$

Because the flow speed in the hydraulic line is negligible compared to the speed of sound in hydraulic fluid, the values for the reverse travelling modes in Equations (7.11) to

(7.24) can be found by replacing $A_{R,n}$, with $B_{R,n}$; and by replacing all instances of $k_{Rx,n}$ with $-k_{Rx,n}$. To differentiate, the displacement and pressures will have a superscript plus and minus added when needed to indicate modes travelling in the positive and negative axial directions.

Each mode n in a region R is characterized by a unique axial wavenumber $k_{Rx,n}$. To find the wavenumber, an eigenequation must be solved in each region. For region 1, the wavenumber must satisfy a zero radial displacement condition at the outer wall; that is,

$$\left[u_{1r,n}\right]_{r=r_0} = 0\,. \tag{7.26}$$

Because of the negligible mean flow speed, the eigenequation has solutions of $\pm k_{Rx,n}$, so it is sufficient to solve only for positive travelling modes. In region 2, five radial boundary or continuity conditions must be met, resulting in five equations that must be solved simultaneously to find the wavenumber $k_{2x,n}$ as well as the relative amplitudes of $y_{1,n}$ through $y_{5,n}$. The conditions and corresponding equations are: zero displacement at the outer wall,

$$\left[u_{2r,n}\right]_{r=r_2} = 0\,, \tag{7.27}$$

continuity of displacement at the bladder,

$$\left[u_{2r,n}\right]_{r=r_3-} = \left[u_{2r,n}\right]_{r=r_3+}\,, \tag{7.28}$$

(r_3- and r_3+ representing the limits as r approaches r_3 from the negative and positive directions), a force balance at the bladder,

$$\left[p_2\right]_{r=r_3-} = \left[p_2 + \sigma_b \ddot{u}_{2r}\right]_{r=r_3+} = \left[p_2 - \omega^2 \sigma_b u_{2r}\right]_{r=r_3+}\,, \tag{7.29}$$

continuity of displacement at the perforate layer,

$$\left[u_{2r,n}\right]_{r=r_1-} = \left[u_{2r,n}\right]_{r=r_1+}, \tag{7.30}$$

and an impedance condition at the perforate layer,

$$\left[p_{2,n}\right]_{r=r_1+} - \left[p_{2,n}\right]_{r=r_1-} = Z_p \left[u_{2r,n}\right]_{r=r_1}, \tag{7.31}$$

where Z_p is the measured or calculated acoustic impedance across the perforate layer. As no experimental studies were found, the perforate impedance was calculated using Eqs. (9.21) and (9.29) of Bies and Hansen[21]. Omitting terms not used in the present analysis, Z_p is calculated as

$$Z_{\mathrm{P}} = \frac{1}{F}\left(\pi a_h^2 R_{\mathrm{P}} + \mathrm{i}\rho_{\mathrm{f}} c_{\mathrm{f}} \tan\left(k_{\mathrm{f}} w + \left(\frac{16 k_{\mathrm{f}} a_h}{3\pi}\right)\left(1 - 0.43\frac{a_h}{q}\right)\right)\right), \tag{7.32}$$

$$R_{\mathrm{P}} = \frac{\rho_{\mathrm{f}} c_{\mathrm{f}} k d}{\pi a^2}\left(\frac{w}{a_h} + 0.288\log_{10}\left(\frac{4a_h^2}{h^2}\right)\right), \tag{7.33}$$

$$d = \sqrt{\frac{2\mu}{\rho_{\mathrm{f}}\omega}}, \tag{7.34}$$

$$h = \max\left(\frac{w}{2}, d\right), \tag{7.35}$$

where w, a_h, q, and F are the perforate layer thickness, hole radius, hole separation distance, and hole area fraction, respectively. As the impedance formulation was derived with gaseous flow through larger orifices in mind, there is some uncertainty as to its applicability to the present case. Of particular note is the log term of R_{P}, which is derived from Eq. (9.1.23) of Morse and Ingard[79]. Morse and Ingard specify that the perforated plate should be much thinner than the perforate hole radius, a condition which is not met

in the current case. Thus, it is uncertain whether the impedance calculation used will be sufficiently accurate.

Solving Equations (7.27) to (7.31) simultaneously for eigenvalues $k_{2x,n}$ thus gives the acoustic pressure and displacement for each mode in region 2. Region 3 has a similar formulation, but does not include the perforate layer:

$$\left[u_{3r,n}\right]_{r=r_2} = 0\,, \tag{7.36}$$

$$\left[u_{3r,n}\right]_{r=r_{3-}} = \left[u_{3r,n}\right]_{r=r_{3+}}, \tag{7.37}$$

$$\left[p_3\right]_{r=r_{3-}} = \left[p_3 - \omega^2\sigma_b u_{3r}\right]_{r=r_{3+}}. \tag{7.38}$$

Given a finite number of radial modes N, the modal amplitudes $A_{R,n}$ and $B_{R,n}$ can be found by simultaneously solving a number of equations which provide for pressure and axial displacement continuity at the region boundaries. The number of equations is reduced by letting all $B_{1D,n}$=0 due to an assumption of an anechoic termination. Additionally, it is assumed that incoming evanescent waves $A_{1U,n}$ have zero amplitude at $x = 0$, with the exception of excitation plane wave $A_{1U,0}$, which is the reference input and is arbitrarily set to unity. To further simplify, the rigid region 3 wall boundaries at $x = -L_1$ and $x = L + L_2$ allow for the immediate substitutions

$$A_{3U,n} = B_{3U,n}\mathrm{e}^{-2\mathrm{i}k_{3x,n}L_1}, \tag{7.39}$$

$$B_{3D,n} = A_{3D,n}\mathrm{e}^{-2\mathrm{i}k_{3x,n}L_2}. \tag{7.40}$$

The other axial equations are in the form of area integrals,

$$\int_0^{r_a}\sum_{n=0}^{N-1}\left(\left[p^+_{1U,n}\right]_{x=0} + \left[p^-_{1U,n}\right]_{x=0}\right)rdr = \int_0^{r_a}\sum_{n=0}^{N-1}\left(\left[p^+_{2,n}\right]_{x=0} + \left[p^-_{2,n}\right]_{x=0}\right)rdr\,, \tag{7.41}$$

$$\int_0^{r_a}\sum_{n=0}^{N-1}\left(\left[p_{1D,n}^{+}\right]_{x=L}+\left[p_{1D,n}^{-}\right]_{x=L}\right)rdr=\int_0^{r_a}\sum_{n=0}^{N-1}\left(\left[p_{2,n}^{+}\right]_{x=L}+\left[p_{2,n}^{-}\right]_{x=L}\right)rdr\,, \tag{7.42}$$

$$\int_{r_1}^{r_c}\sum_{n=0}^{N-1}\left(\left[p_{3U,n}^{+}\right]_{x=0}+\left[p_{3U,n}^{-}\right]_{x=0}\right)rdr=\int_{r_1}^{r_c}\sum_{n=0}^{N-1}\left(\left[p_{2,n}^{+}\right]_{x=0}+\left[p_{2,n}^{-}\right]_{x=0}\right)rdr\,, \tag{7.43}$$

$$\int_{r_1}^{r_c}\sum_{n=0}^{N-1}\left(\left[p_{3D,n}^{+}\right]_{x=L}+\left[p_{3D,n}^{-}\right]_{x=L}\right)rdr=\int_{r_1}^{r_c}\sum_{n=0}^{N-1}\left(\left[p_{2,n}^{+}\right]_{x=L}+\left[p_{2,n}^{-}\right]_{x=L}\right)rdr\,, \tag{7.44}$$

$$\int_0^{r_b}\sum_{n=0}^{N-1}\left(\left[u_{2x,n}^{+}\right]_{x=0}+\left[u_{2x,n}^{-}\right]_{x=0}\right)rdr=\begin{cases}\displaystyle\int_0^{r_b}\sum_{n=0}^{N-1}\left(\left[u_{1Ux,n}^{+}\right]_{x=0}+\left[u_{1Ux,n}^{-}\right]_{x=0}\right)rdr, & r_b<r_0\\ U_U, & r_0\le r_b<r_1\\ \displaystyle U_U+\int_{r_1}^{r_b}\sum_{n=0}^{N-1}\left(\left[u_{3Ux,n}^{+}\right]_{x=0}+\left[u_{3Ux,n}^{-}\right]_{x=0}\right)rdr, & r_b\ge r_1\end{cases}, \tag{7.45}$$

$$\int_0^{r_b}\sum_{n=0}^{N-1}\left(\left[u_{2x,n}^{+}\right]_{x=L}+\left[u_{2x,n}^{-}\right]_{x=L}\right)rdr=\begin{cases}\displaystyle\int_0^{r_b}\sum_{n=0}^{N-1}\left(\left[u_{1Dx,n}^{+}\right]_{x=0}+\left[u_{1Dx,n}^{-}\right]_{x=0}\right)rdr, & r_b<r_0\\ U_D, & r_0\le r_b<r_1\\ \displaystyle U_D+\int_{r_1}^{r_b}\sum_{n=0}^{N-1}\left(\left[u_{3Dx,n}^{+}\right]_{x=L}+\left[u_{3Dx,n}^{-}\right]_{x=L}\right)rdr, & r_b\ge r_1\end{cases}, \tag{7.46}$$

$$U_U=\int_0^{r_0}\sum_{n=0}^{N-1}\left(\left[u_{1Ux,n}^{+}\right]_{x=0}+\left[u_{1Ux,n}^{-}\right]_{x=0}\right)rdr\,, \tag{7.47}$$

$$U_D=\int_0^{r_0}\sum_{n=0}^{N-1}\left(\left[u_{1Dx,n}^{+}\right]_{x=L}+\left[u_{1Dx,n}^{-}\right]_{x=L}\right)rdr\,, \tag{7.48}$$

$$r_a=\frac{m+1}{M}r_0,\quad r_b=\frac{m+1}{M}r_2,\quad r_c=r_1+\frac{m+1}{M}\left(r_2-r_1\right), \tag{7.49}$$

where m = 0 to M-1, and $M = N$. Acoustic transmission loss (TL) can then be found as

$$\mathrm{TL}=-20\log_{10}\left|\frac{A_{1D,0}}{A_{1U,0}}\right|^2, \tag{7.50}$$

7.3 Experiment

To validate the analytical model predictions, a commercially available suppressor, Wilkes & McLean model WM-5081, was purchased and tested. It was non-destructively disassembled to measure various internal dimensions. A model WM-3081 was also purchased and permanently deconstructed to determine the remaining internal dimensions; it is rated for a lower pressure than the WM-5081 and therefore has a different external casing, but all internal construction details are identical as far as can be verified. The relevant dimensions and measurements for the suppressor are found in Table 22, including bladder measurements for finding σ_b. Additional dimensions were measured for the thin perforated sheet, shown in Table 23, in order to estimate Z_p. The hydraulic fluid used in these tests has density ρ_f = 866 kg m^{-3} and sound speed c_f = 1400 m s^{-1}. The test setup and methodology are detailed in Chapter 3.

Table 22: Commercial suppressor dimensions

Inlet Pipe Radius r_0 (m)	0.0103
Uncompressed Inner Radius r_1 (m)	0.0173
Outer Radius r_2 (m)	0.0262
Length L (m)	0.0450
Inlet extension L_1 (m)	0.0185
Outlet extension L_2 (m)	0.0185
Bladder total mass m_b (kg)	0.038
Bladder total length (m)	0.112

Table 23: Perforate layer dimensions and features

Perforate layer thickness w (m)	0.0006
Perforate hole radius a_h (m)	0.0005
Perforate hole separation q (m)	0.0027
Perforate hole area fraction F	0.227

The hydraulic fluid used in these tests has density ρ_f = 866 kg m^{-3} and sound speed c_f = 1400 m s^{-1}. The kinematic viscosity of the fluid is published to be 46.0 cSt at 40°C and 6.8 cSt at 100°C; a linear fit is taken for experimentally measured temperatures.

7.4 Results

7.4.1 Modeling results

Several new features have been added to existing methods to create the present suppressor model. There is some uncertainty in the model regarding the effects and reliability of some of these additions; specifically of concern are the bladder mass, the temperature of the compressed gas when the bladder is filled, and how the perforate model affects transmission loss performance. These three items are examined in further detail in this section. First, the mass of the rubber bladder is considered. The total mass contained in the expansion area is uncertain; the expansion length L_T is 0.73 times the total bladder length, but the effective mass of the bladder will be less than this fraction because the bladder thickens into rings at each end, resulting in a nonuniform mass distribution per length. It is estimated that using 0.5 times the measured bladder mass, 0.019 kg, in Equation (7.5) will approximately account for the bladder sheet density. To test the sensitivity of this estimate to errors, simulations have been run for m_b equal to 0.019, 0.027, and 0.038 kg, as shown in Figure 61. Although differences of around 4 dB are observed above 3000 Hz, the differences are below about 1.5 dB below 2000 Hz. The results are therefore relatively insensitive to changes in bladder mass, especially at low frequencies; and any error in the bladder estimation should not cause significant error in the transmission loss predictions.

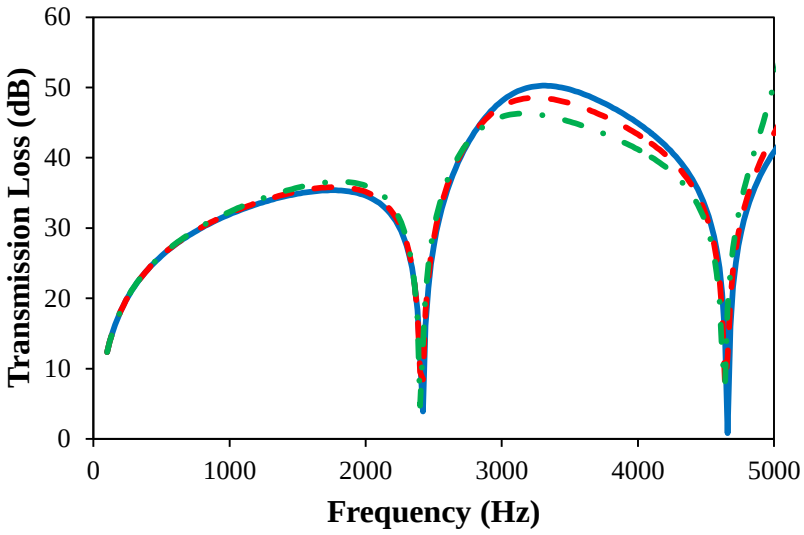

Figure 61: Study of TL versus bladder mass, P_s = 10.3 MPa, P_c = 5.2 MPa, no perforate layer. — m_b = 0.019 kg; — — m_b = 0.027 kg; — · m_b = 0.038 kg

In addition, temperature affects the compressibility of the nitrogen and may have important effects on transmission loss. Although the system temperature during testing is measured, there is some uncertainty in the temperature when the bladder is initially pressurized up to P_c, which affects the calculated mass of the nitrogen and bladder radius r_3. For a system running at 36°C, precharge temperatures of 20°C and 40°C are simulated in Figure 62 to determine the sensitivity to precharge temperature. As can be observed, the differences are minimal over the whole range of 0 to 5000 Hz, and it is thus concluded that uncertainty or reasonable variation in bladder precharge temperature will not significantly affect transmission loss predictions.

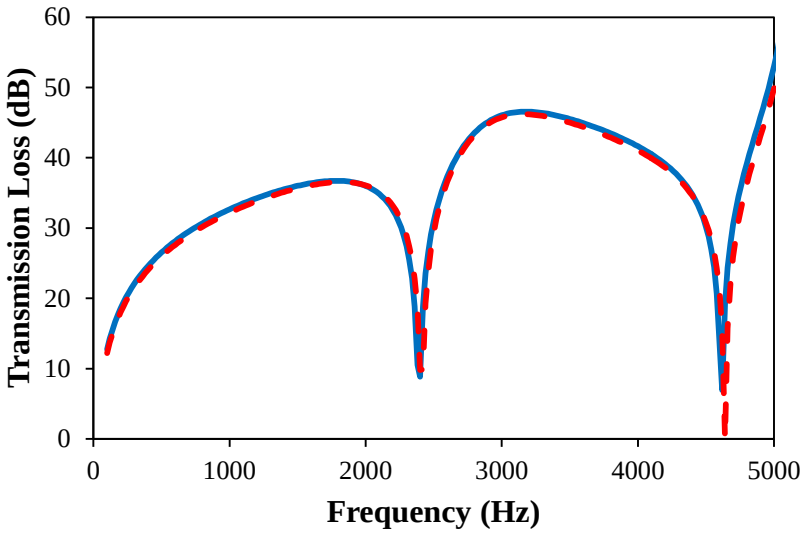

Figure 62: TL versus temperature study, P_s = 10.3 MPa, P_c = 5.2 MPa, no perforate layer, system temperature = 36°C. Nitrogen precharge temperature: — 20°C; — — 40°C.

Finally, sensitivity to the perforate layer is investigated. As no experimental studies were found, the perforate impedance was calculated using Equations (9.21) and (9.29) of Bies and Hansen[21]. However, part of the derivation of this model, from Equation (9.1.23) of Morse and Ingard[79], requires that the perforated plate be much thinner than the perforate hole radius, a condition which is not met in the current case. Thus, the validity of the current perforate impedance model is called into question. Nevertheless, the model may give some indication of the importance and probable effects of the perforate layer. Two simulations are shown in Figure 63, where the only difference is inclusion of the perforate layer. The difference between the models is clear, reaching 5 dB at a frequency of about 1500 Hz, and continuing to show significant deviation at higher frequencies. To help determine the validity of the current perforate model, results are shown with and without the perforate layer in the experimental validation section.

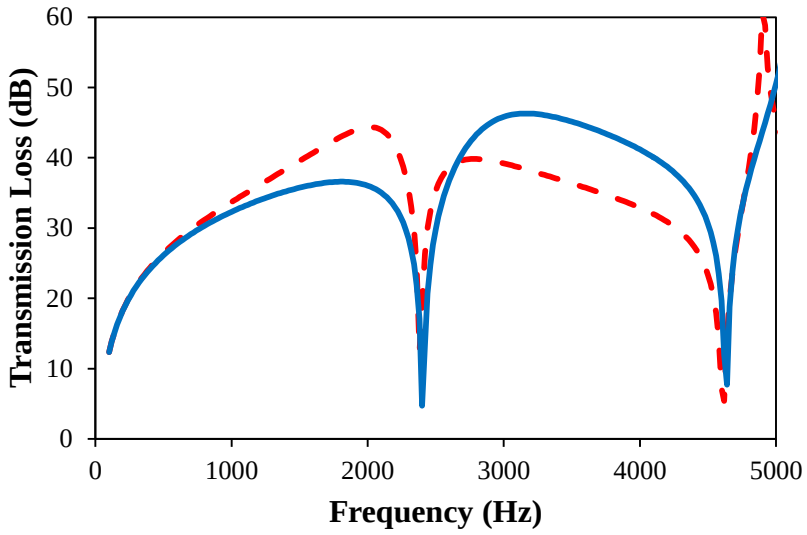

Figure 63: TL versus perforate layer impedance study, P_s = 10.3 MPa, P_c = 5.2 MPa. — No perforate layer; — — Includes perforate layer impedance.

7.4.2 Experimental validation

To validate the model experimentally, tests were run on the experimental rig at various system and bladder precharge pressures. Figure 64 shows the validation for a system pressure of P_s = 10.3 MPa and a precharge pressure of P_c = 2.1 MPa. In Figure 65 and Figure 66, P_s is maintained, but P_c is increased to 3.1 MPa and then to the manufacturer recommended 0.5 P_s, or 5.2 MPa. In Figure 67, P_c is maintained at 0.5 P_s, with P_s being increased to 20.7 MPa, and P_c at 10.3 MPa. Experimental data were filtered to remove points where $e_e > 0.05$. This is higher than the 0.03 criterion used for prototype data, because the stricter criterion removes too much data for the results to be useful. RMSE of each case, for the frequency range 0-2000 Hz, is shown in Table 24.

In all the figures below, the simulation with the perforate layer shows less agreement with low frequency experimental data than the simulation that omits the perforate layer. Also, at low frequencies (below 2000 Hz) better agreement is found with experimental data when the precharge pressure is lower (Figure 64 to Figure 66), or,

considering the same relative precharge percentage, when the total pressure is higher (Figure 66 and Figure 67). Notably, the predicted transmission loss dips around 2500 Hz are not observed in the experimental data; additionally, experimental agreement is poor generally above 2000 Hz, especially for frequencies of high predicted transmission loss. The lack of an experimental transmission loss dip around 2500 Hz could be indicative of insufficiently modeled system damping; the large divergence between model and experiment at higher frequencies may indicate flanking transmission paths or unmodeled phenomena that become significant at higher frequencies. The divergence may also be indicative of the upper limit of measurement capability for the test rig, since as TL increases, any minor disturbances in the downstream section may begin to overwhelm the ideal signal measurement. Judging from the available experimental data and models, this facility limit of the rig is estimated to be about 30 dB of transmission loss. In addition to test rig limitations, discrepancies may indicate a need for improved perforate layer models, or for more complex models of the rubber bladder behavior. Nevertheless, the model is accurate within 5 dB up to about 1300 Hz for all tests with the system pressures here examined, and bladder precharge pressures up to 0.5 times system pressure; and up to about 2300 Hz for three of the cases. This makes it useful for at least the first several harmonics of many axial piston pumps, which are commonly used in the hydraulics industry.

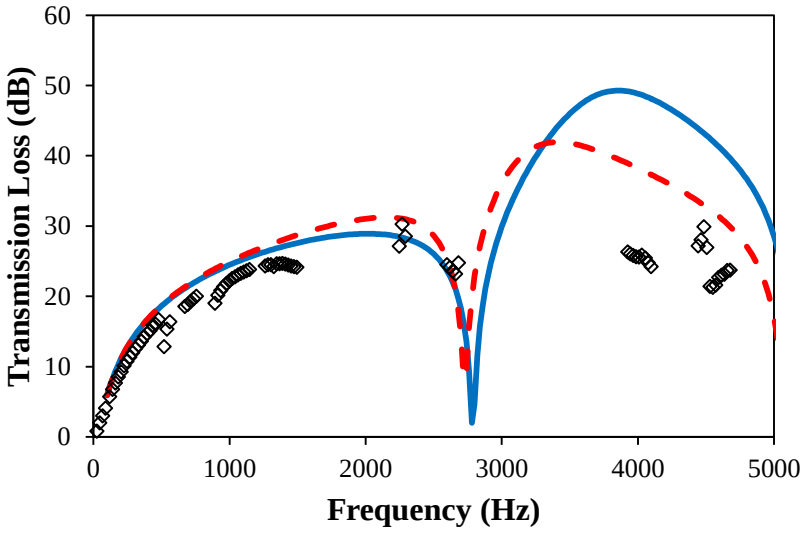

Figure 64: Experimental and model TL, P_s = 10.3 MPa, P_c = 2.1 MPa. ◇ Reduced experimental data; — Model, no perforate layer; — — Model with perforate layer impedance.

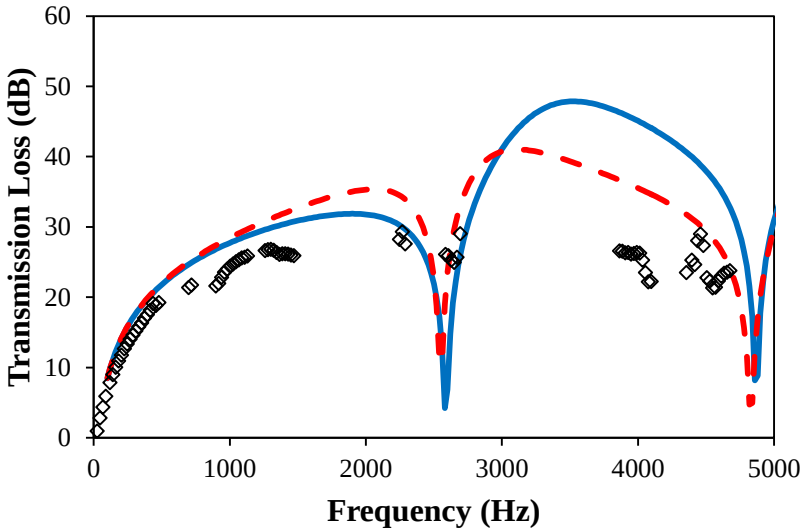

Figure 65: Experimental and model TL, P_s = 10.3 MPa, P_c = 3.1 MPa. ◇ Reduced experimental data; — Model, no perforate layer; — — Model with perforate layer impedance.

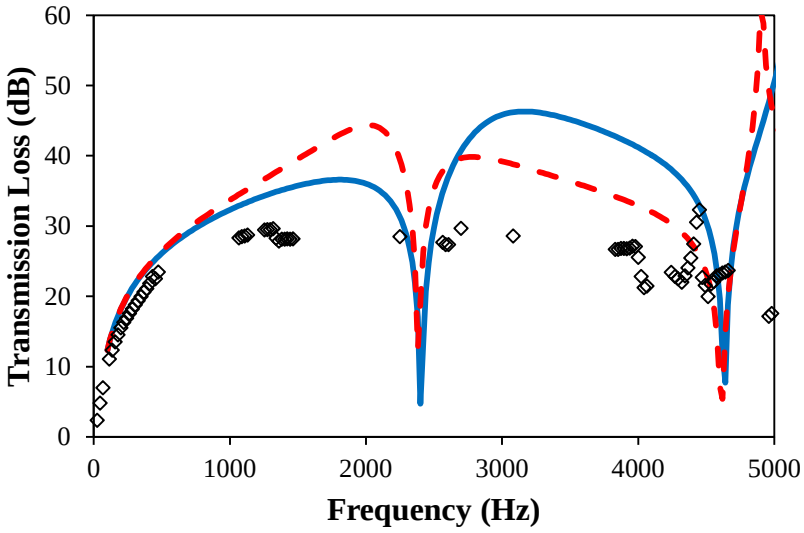

Figure 66: Experimental and model TL, P_s = 10.3 MPa, P_c = 5.2 MPa. ◇ Reduced experimental data; — Model, no perforate layer; — — Model with perforate layer impedance..

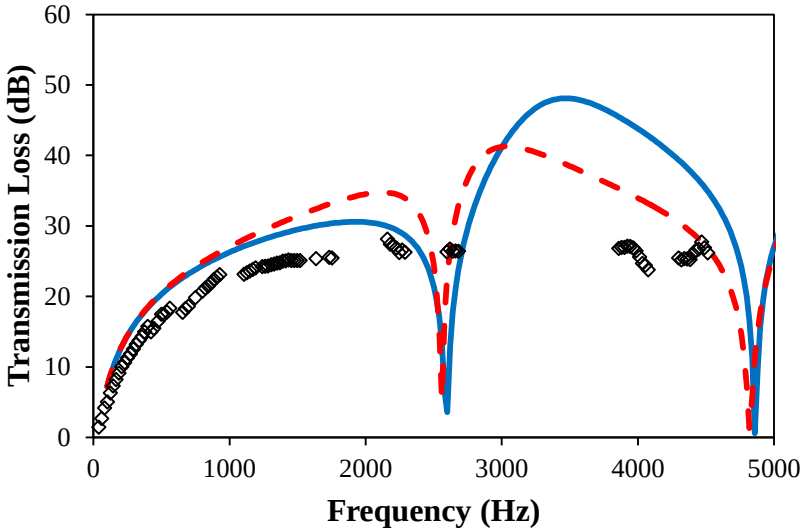

Figure 67: Experimental and model TL, P_s = 20.7 MPa, P_c = 10.3 MPa. ◇ Reduced experimental data; — Model, no perforate layer; — — Model with perforate layer impedance.

Table 24: Root Mean Squared Error for various bladder style suppressor conditions

P_s (MPa)	P_c (MPa)	RMSE 0-2000 Hz, no perforate layer (dB)	RMSE 0-2000 Hz, with perforate layer (dB)
10.3	2.1	2.3	2.8
10.3	3.1	3.1	3.9
10.3	5.2	4.4	6.0
20.7	10.3	3.6	4.4

7.5 Comparison to optimized syntactic foam

In Chapter 6, a material optimization was performed with respect to three different use cases. In order to compare the potential performance of a syntactic foam suppressor to a commercial compressed gas style compressor, the objective function in Equation (6.4) is calculated for the commercial suppressor considered in this chapter, which is of similar external dimensions to the prototype suppressor considered in the previous chapters. For the compressed gas style suppressor, no optimization needs to be performed; since TL drops to nearly zero once precharge pressure exceeds system pressure[80], the maximum performance will almost necessarily be at a pressure slightly below the minimum system pressure; this has been verified for the current set of optimization cases. For this comparison, the precharge pressure is 3.1 MPa, or 90% of the lowest pressure bin value. The objective function values are compared to the best objective function values from Section 6.3.3, which is from Optimization 2; all three values of F_H are shown. Depending on the assumption of F_H, the optimized syntactic foam suppressor is predicted to perform as well as or better than the compressed gas suppressor for the trenching task and the equal time case. For the back fill task, the compressed gas suppressor has a better objective function than the syntactic foam device with F_H = 0.5. Of the three tasks, the back fill task is most heavily weighted toward low pressures, which is why the compressed gas suppressor has relatively better performance

for that task. The gas suppressor necessarily performs best at system pressures just above the precharge pressure, and steadily worse as system pressure increases. Thus, the ability to create a syntactic foam liner using microspheres with an arbitrary distribution of buckling pressures is very advantageous for hydraulic systems where much time is spent at different system pressures.

Table 25: Comparison to optimized suppressor from Chapter 6.

Device/liner	Objective function (dB) for case:		
	Back fill task	Trenching task	Equal time case
Compressed gas suppressor	-18.21	-15.68	-15.19
Optimization 2, $F_H = 0$	-20.47	-19.99	-19.02
Optimization 2, $F_H = 0.32$	-19.84	-17.67	-16.79
Optimization 2, $F_H = 0.5$	-16.30	-15.86	-15.01

CHAPTER 8

CONCLUSIONS

8.1 Summary of results

A multimodal model has been developed for the analysis of in-line hydraulic suppressors with solid insert liners. The model couples longitudinal waves in the working fluid with longitudinal and shear waves in the liner, and it takes into account the compression of the liner due to hydrostatic pressure. It has been successfully validated against a finite element model, and against experimental data at two different suppressor lengths. The model has been used to estimate material properties of several different prototype inserts. It is shown that the model is relatively insensitive to axial position of the compressed liner; and that a bulk modulus simplified model gives reasonably accurate results for analyzing syntactic foam liners.

A material model has been developed which attempts to determine static bulk modulus of the syntactic foam based the constituent materials in the syntactic foam. The model parameters are derived using a combination of directly measured data, manufacturer's data, and material compression experiments. Bulk modulus values found from compression data using this model are similar to the low frequency bulk modulus found from transmission loss data using the multimodal model in certain cases. The best fits are generally found for low bulk modulus values, due to the inverse dependence on slope of the compression curve. Additionally, the model accuracy suffers due to the lack of temperature dependence in data used to find model parameters. Nevertheless, based on estimated parameters from existing liners, the material model is used to predict material

properties for new liners based on composition, and several compositions are estimated to optimize noise reduction on a hydraulic excavator's boom actuation system for three different use cases.

The multimodal method has also been extended to a compressed gas style suppressor such as those that are currently commercially available. The presented theoretical model has been shown to correspond well to experimental data at frequencies of interest for many hydraulic systems, with the quality of fit depending on system and precharge pressure conditions. Simulations show that the transmission loss predictions are sensitive to impedance of the perforate layer, but existing theoretical treatments of the perforate layer effects are found to be inadequate for the purposes of this model.

A comparison is made between the predicted transmission loss of an optimized syntactic foam lined suppressor, and a compressed gas style suppressor of similar dimensions. The results are found to depend on the work cycle, as well as the total compressible volume of the microspheres, but in general the syntactic foam is found to perform comparably to the compressed gas device. The compressed gas suppressor is able to compress more overall, which translates to higher transmission losses at the optimal pressures; but it must generally be configured to work best at low pressures, because performance at system pressures below the precharge pressure is extremely bad. In contrast, the syntactic foam has less available gas volume to compress, but the buckling pressures can theoretically be distributed in any arbitrary manner, so a single liner could provide acceptable transmission loss at two widely separated pressures. Additionally, the performance of the syntactic foam device will depend on having a high gas to shell volume ratio when buckling pressures are high; at present, the possible ratios

are unknown, and so the overall potential efficacy of the syntactic foam suppressors is still unknown.

8.2 Future work and conclusions

While many initial results in this work are promising, much work is still needed to make syntactic foam lined suppressors into viable commercial products. The primary need is a supply of microspheres which reversibly buckles at pressures in the 10 to 30 MPa range. In the spheres used in this work, shell thickness increased with increased buckling pressure, reducing the total amount of compressible gas in the liner. Thus, the high pressure results may also depend on shell material selection for the microspheres, inasmuch as that determines shell thickness. More study will also be needed regarding the choice of polymer matrix, depending on desired damping characteristics and temperature response, though some of the materials used in this study may also be suitable for use in high pressure syntactic foams as well.

There is also much room for improvements in the syntactic foam models. More complete constituent material properties, more accurate compression tests with temperature data, more reliable transmission loss data, and complete static and dynamic testing of the liners at various pressures would all be useful in producing more accurate models, and in better validating the models that have been presented. With additional information on the constituent materials, it might also be possible to create first principle models or micro-scale finite element models to better predict composite material performance as well.

Finally, the opportunities for syntactic foams in fluid-borne noise reduction are much broader than just in-line suppressors. The syntactic foams may be cast in a variety

of shapes, and could potentially be incorporated as internal linings on hoses or other hydraulic circuit components. This might reduce the need for separate noise control components in systems, saving space which is often at a premium in mobile hydraulic equipment.

APPENDIX A

PARTICLE SIZE DOCUMENTATION

www.Expancel.com

PARTICLE SIZE OF EXPANCEL® DE

Technical Bulletin no 8b

PARTICLE SIZE OF EXPANCEL® DE

*The particle size is determined in each batch of **EXPANCEL DE**. The technique we use is laser diffraction.*

SYSTEM DESCRIPTION

Optical part	Malvern Mastersizer 2000
Sample dispersion - accessories	Sirocco 2000
Software	Mastersizer 2000
Measurement principle	Mie scattering
Light sources	Red light: Helium neon laser. Blue light: Solid state light source
Detection system	Red light: Forward scattering, side and back scattering Blue light: Wide angle forward and back scattering.

PROCEDURE

The particle size of **EXPANCEL DE** is measured by laser diffraction, Low Angle Laser Light Scattering (LALLS). The applicable range is 0,02 - 2000 µm. The instrument has a laser source of coherent intense light of fixed wavelength and several photosensitive detectors.

The dry powder of **EXPANCEL DE** is blown through the beam by means of pressure in a measuring cell and sucked into a vacuum cleaner to prevent dust.

This instrument, Malvern Mastersizer 2000 uses the full MIE theory which solves the equation for interaction of light with matter. The MIE theory assumes the volume of the particle and considers the refractive indices of the material for the calculation. For information read www.Malvern.com.

Software-driven SOPs, Standard Operating Procedures eliminate user variability and enable global method transfer. All measurement parameters are automatically embedded in the result files.

Measurements can be replicated by following the same SOP. Every sample analysis has a background measurement.

The particle size is reported by a distribution curve with following calculated results.

D01	median particle size when 10% of the particles are smaller and 90% are larger.
D05	median particle size where 50% of the sample are smaller and larger.
D09	median particle size when 90% of the particles are smaller and 10% are larger.
Span	explains the amplitude of the size distribution curve, |D09 – D01|/D05.
Concentration	the concentration of the volume in the sample.
Obscuration	concentration of the sample in the surrounding media.
Particle RI	the refractive indices of the sample.
Weighed residual	The residual is an indication of how well the calculated data was fitted to the measurement data. A good fit is indicated by a residual of less than 1%. If the residuals are over 1% this may be an indication that you have not used the correct refractive index and absorption values for the sample and dispersant.

Se enclosed distribution curve.

COMMENTS

The information contained in this leaflet is the result of our research and experience. It is given in good faith, but under no circumstances does it constitute a guarantee on our part, nor does it hold us responsible, particularly in the case of legal action by a third party.

MASTERSIZER 2000

Result Analysis Report

Sample Name: 20030082-49 551-40-2 dens.42,3 -	**SOP Name:** 551DE	**Measured:** den 23 januari 2003 10:11:42
Measured by: layne	**Result Source:** Averaged	**Analysed:** den 23 januari 2003 10:11:43

Particle RI:	Accessory Name:	Analysis model:	Weighted Residual:
1,540	Scirocco 2000 (A)	General purpose	0,629 %

Span : 1,001

d(0.1): 24,415 µm **d(0.5):** 39,649 µm **d(0.9):** 64,112 µm

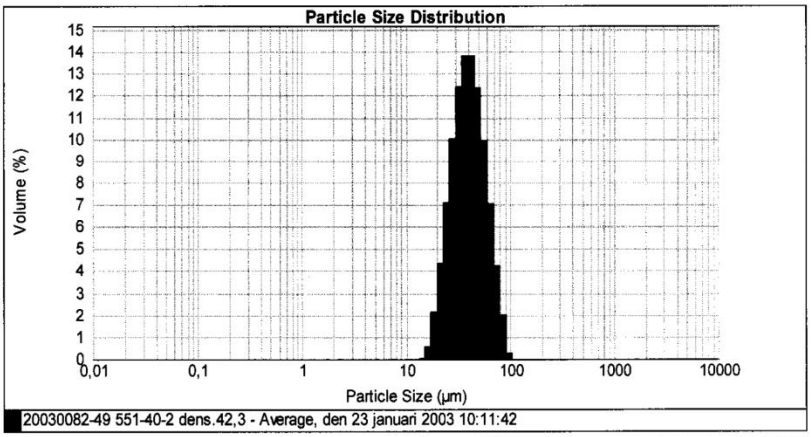

Size (µm)	Volume In %
0,010	0,00
0,011	0,00
0,013	0,00
0,015	0,00
0,017	0,00
0,020	0,00
0,023	0,00
0,026	0,00
0,030	0,00
0,035	0,00
0,040	0,00
0,046	0,00
0,052	0,00
0,060	0,00
0,069	0,00
0,079	0,00
0,091	0,00
0,105	0,00

Size (µm)	Volume In %
0,105	0,00
0,120	0,00
0,138	0,00
0,158	0,00
0,182	0,00
0,209	0,00
0,240	0,00
0,275	0,00
0,316	0,00
0,363	0,00
0,417	0,00
0,479	0,00
0,550	0,00
0,631	0,00
0,724	0,00
0,832	0,00
0,955	0,00
1,096	0,00

Size (µm)	Volume In %
1,096	0,00
1,259	0,00
1,445	0,00
1,660	0,00
1,905	0,00
2,188	0,00
2,512	0,00
2,884	0,00
3,311	0,00
3,802	0,00
4,365	0,00
5,012	0,00
5,754	0,00
6,607	0,00
7,586	0,00
8,710	0,00
10,000	0,00
11,482	0,00

Size (µm)	Volume In %
11,482	0,00
13,183	0,03
15,136	0,58
17,378	2,15
19,953	4,32
22,909	7,12
26,303	10,00
30,200	12,42
34,674	13,80
39,811	13,78
45,709	12,37
52,481	9,93
60,256	7,03
69,183	4,26
79,433	1,99
91,201	0,24
104,713	0,00
120,226	0,00

Size (µm)	Volume In %
120,226	0,00
138,038	0,00
158,489	0,00
181,970	0,00
208,930	0,00
239,883	0,00
275,423	0,00
316,228	0,00
363,078	0,00
416,869	0,00
478,630	0,00
549,541	0,00
630,957	0,00
724,436	0,00
831,764	0,00
954,993	0,00
1096,478	0,00
1258,925	0,00

Size (µm)	Volume In %
1258,925	0,00
1445,440	0,00
1659,587	0,00
1905,461	0,00
2187,762	0,00
2511,886	0,00
2884,032	0,00
3311,311	0,00
3801,894	0,00
4365,158	0,00
5011,872	0,00
5754,399	0,00
6606,934	0,00
7585,776	0,00
8709,636	0,00
10000,000	0,00

MASTERSIZER 2000

Result Analysis Report

Sample Name: 20030320-092-120-2 dens 30,8 -	**SOP Name:** 092DE	**Measured:** den 10 februari 2003 09:14:21	
Measured by: A-L	**Result Source:** Averaged	**Analysed:** den 10 februari 2003 09:14:22	
Particle RI: 1,590	**Accessory Name:** Scirocco 2000 (A)	**Analysis model:** General purpose	**Weighted Residual:** 0,400 %

Span : 1,111

d(0.1): 57,511 µm **d(0.5):** 102,448 µm **d(0.9):** 171,331 µm

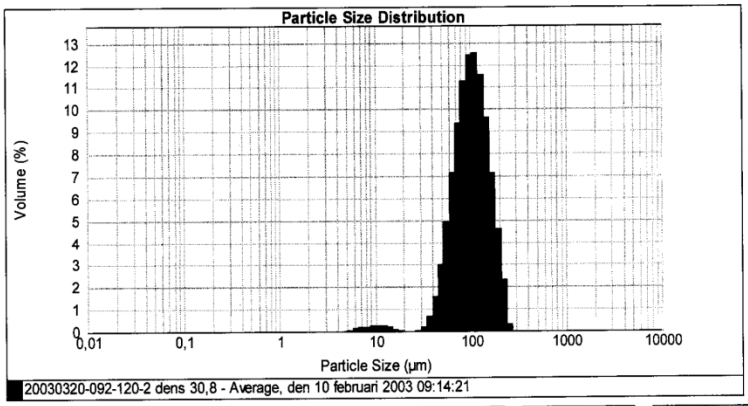

Size (µm)	Volume In %
0,010	0,00
0,011	0,00
0,013	0,00
0,015	0,00
0,017	0,00
0,020	0,00
0,023	0,00
0,026	0,00
0,030	0,00
0,035	0,00
0,040	0,00
0,046	0,00
0,052	0,00
0,060	0,00
0,069	0,00
0,079	0,00
0,091	0,00
0,105	0,00

Size (µm)	Volume In %
0,105	0,00
0,120	0,00
0,138	0,00
0,158	0,00
0,182	0,00
0,209	0,00
0,240	0,00
0,275	0,00
0,316	0,00
0,363	0,00
0,417	0,00
0,479	0,00
0,550	0,00
0,631	0,00
0,724	0,00
0,832	0,00
0,955	0,00
1,096	0,00

Size (µm)	Volume In %
1,096	0,00
1,259	0,00
1,445	0,00
1,660	0,00
1,905	0,00
2,188	0,00
2,512	0,00
2,884	0,00
3,311	0,00
3,802	0,00
4,365	0,00
5,012	0,00
5,754	0,03
6,607	0,11
7,586	0,16
8,710	0,21
10,000	0,25
11,482	0,26

Size (µm)	Volume In %
11,482	0,24
13,183	0,19
15,136	0,10
17,378	0,01
19,953	0,00
22,909	0,00
26,303	0,01
30,200	0,17
34,674	0,67
39,811	1,58
45,709	3,00
52,481	4,88
60,256	7,10
69,183	9,35
79,433	11,26
91,201	12,41
104,713	12,53
120,226	

Size (µm)	Volume In %
120,226	11,54
138,038	9,59
158,489	7,14
181,970	4,59
208,930	2,30
239,883	0,32
275,423	0,00
316,228	0,00
363,078	0,00
416,869	0,00
478,630	0,00
549,541	0,00
630,957	0,00
724,436	0,00
831,764	0,00
954,993	0,00
1096,478	0,00
1258,925	

Size (µm)	Volume In %
1258,925	0,00
1445,440	0,00
1659,587	0,00
1905,461	0,00
2187,762	0,00
2511,886	0,00
2884,032	0,00
3311,311	0,00
3801,894	0,00
4365,158	0,00
5011,872	0,00
5754,399	0,00
6606,934	0,00
7585,776	0,00
8709,636	0,00
10000,000	

AKZO NOBEL

Head Office: Expancel, Box 13000, SE-850 13 Sundsvall, SWEDEN, Phone: +46 60 13 40 00, Fax: +46 60 56 95 18
US Office: Expancel Inc, 2240 Northmont Pkwy, Duluth GA 30096, USA, Phone: +1 770 813 9126, Fax: +1 770 813 8639
E-mail: info@expancel.com Internet: www.Expancel.com

Issue 2007-05-08 (Replaces 2005-04-18)

REFERENCES

1. Rabie, M.G., *On the application of oleo-pneumatic accumulators for the protection of hydraulic transmission lines against water hammer - a theoretical study.* International Journal of Fluid Power, 2007. **8**(1): p. 39-49.

2. Byrd Jr., W. and W. Annis, *Hydraulic surge damper*, in *USPTO*, USA patent no. 2,495,693. United States Navy, 1950.

3. Kachnik, J.E., *Supercharge hose*, in *USPTO*, USA patent no. 3,665,967. The Western Company of North America, 1972.

4. Henderson, A.R. and R.J. Whitson, *Hydraulic noise attenuators*, in *USPTO*, USA patent no. 4,671,380. American Olaer, Inc., 1987.

5. Hansen, R.C., *Fluidborne noise attenuator*, in *USPTO*, USA patent no. 4,314,621. Caterpillar Tractor Co., 1982.

6. Beach, R.H., *Pipe line noise eliminator*, in *USPTO*, USA patent no. 2,261,948. Gerotor May Company, 1941.

7. Dexter, E., *Pulsation dampener and acoustic attenuator*, in *USPTO*, USA patent no. 4,497,388. Gaulin Corporation, 1985.

8. Arendt, E., *Pulsation absorbing device*, in *USPTO*, USA patent no. 4,759,387. Wilkes-McLean, Ltd., 1988.

9. Jenski, J., Gary M. and J.C. Shiery, *Noise suppressor*, in *USPTO*, USA patent no. 5,735,313. Aeroquip Corporation, 1998.

10. Jenski, J., Gary M. and J.C. Shiery, *Noise suppressor*, in *USPTO*, USA patent no. 6,131,613. Aeroquip Corporation, 2000.

11. Shiery, J.C., *Noise suppressor*, in *USPTO*, USA patent no. 5,732,741. Aeroquip Corporation, 1998.

12. Wilkes, R. *Noise Reduction in Hydraulic Systems*. in *Inter-Noise 95*. 1995. Newport Beach, CA, USA.

13. Blackstock, D.T., *Fundamentals of physical acoustics*. 2000, New York: John Wiley & Sons, Inc.

14. Xu, M.B., et al., *Sound attenuation in dissipative expansion chambers.* Journal of Sound and Vibration, 2003. **272**(3-5): p. 1125-1133.

15. Peat, K.S., *A transfer matrix for an absorption silencer element.* Journal of Sound and Vibration, 1991. **146**(2): p. 353-360.

16. Cummings, A. and I.-J. Chang, *Sound attenuation of a finite length dissipative flow duct silencer with internal mean flow in the absorbent.* Journal of Sound and Vibration, 1988. **127**(1): p. 1-17.

17. Kirby, R. and F.D. Denia, *Analytic mode matching for a circular dissipative silencer containing mean flow and a perforated pipe.* Journal of the Acoustical Society of America, 2007. **122**(6): p. 3471-3482.

18. Kirby, R., *Simplified techniques for predicting the transmission loss of a circular dissipative silencer.* Journal of Sound and Vibration, 2001. **243**(3): p. 403-426.

19. Nennig, B., E. Perrey-Debain, and M. Ben Tahar, *A mode matching method for modeling dissipative silencers lined with poroelastic materials and containing mean flow.* Journal of the Acoustical Society of America, 2010. **128**(6): p. 3308-3320.

20. Selamet, A., et al., *Analytical approach for sound attenuation in perforated dissipative silencers.* Journal of the Acoustical Society of America, 2004. **115**(5): p. 2091-2099.

21. Bies, D.A. and C.H. Hansen, *Engineering Noise Control: Theory and Practice*. Fourth Ed. ed. 2009, New York: Spon Press.

22. Sullivan, J.W. and M.J. Crocker, *Analysis of concentric-tube resonators having unpartitioned cavities.* Journal of the Acoustical Society of America, 1978. **64**(1): p. 207-215.

23. Dickey, N.S., A. Selamet, and M.S. Ciray, *An experimental study of the impedance of perforated plates with grazing flow.* Journal of the Acoustical Society of America, 2001. **110**(5): p. 2360-2370.

24. Kirby, R. and A. Cummings, *The impedance of perforated plates subjected to grazing gas flow and backed by porous media.* Journal of Sound and Vibration, 1998. **217**(4): p. 619-636.

25. Lee, I., A. Selamet, and N.T. Huff, *Acoustic impedance of perforations in contact with fibrous material.* Journal of the Acoustical Society of America, 2006. **119**(5): p. 2785-2797.

26. Selamet, A. and Z.L. Ji, *Acoustic attenuation performance of circular expansion chambers with extended inlet/outlet.* Journal of Sound and Vibration, 1999. **223**(2): p. 197-212.

27. Denia, F.D., et al., *Acoustic attenuation performance of perforated dissipative muflers with empty inlet/outlet extensions.* Journal of Sound and Vibration, 2007. **302**: p. 1000-1017.

28. Selamet, A., et al., *Analytical approach for sound attenuation in perforated dissipative silencers with inlet/outlet extensions.* Journal of the Acoustical Society of America, 2005. **117**(4): p. 2078-2089.

29. Panigrahi, S.N. and M.L. Munjal, *Comparison of various methods for analyzing lined circular ducts.* Journal of Sound and Vibration, 2005. **285**: p. 905-923.

30. Bilawchuk, S. and K.R. Fyfe, *Comparison and implementation of the various numerical methods used for calculating transmission loss in silencer systems.* Applied Acoustics, 2003. **64**: p. 903-916.

31. Lee, I., A. Selamet, and N.T. Huff, *Impact of perforation impedance on the transmission loss of reactive and dissipative silencers.* Journal of the Acoustical Society of America, 2006. **120**(6): p. 3706-3713.

32. Longmore, D.K. and A. Schlesinger, *Relative importance of the various vibration transmitting mechanisms in hoses in typical hydraulic systems.* Proc. IMechE Part I: J. Systems and Control Engineering, 1991. **205**(2): p. 105-111.

33. Klees, G.T., *Attenuating device*, in *USPTO*, USA patent no. 3323305. 1967.

34. Hastings, M.C. and C.-C. Chen. *Analysis of Tuning Cables for Reduction of Fluidborne Noise in Automotive Power Steering Hydraulic Lines*. in *Proceedings of the 1993 Noise and Vibration Conference*. 1993. SAE International.

35. Drew, J.E., D.K. Longmore, and D.N. Johnston, *Theoretical analysis of pressure and flow ripple in flexible hoses containing tuners.* Proceedings of the Institution of Mechanical Engineers, 1998. **212**(1): p. 405-422.

36. Way, T.M., *The use of hoses and hose inserts to reduce pressure ripple in hydraulic circuits*, 2004, University of Bath.

37. Munjal, M.L. and P.T. Thawani, *Acoustic performance of hoses—A parametric study.* Noise Control Engineering Journal, 1996. **44**(6): p. 274-280.

38. Dodson, J.M., D.R. Dowling, and K. Grosh, *Experimental investigation of quarter wavelength silencers in large-scale hydraulic systems.* Noise Control Engineering Journal, 1998. **46**(1): p. 15-22.

39. Suo, L. and E.B. Wylie, *Complex Wavespeed and Hydraulic Transients in Viscoelastic Pipes.* Journal of Fluids Engineering, 1990. **112**.

40. Munjal, M.L. and P.T. Thawani, *Acoustic analysis and design of compliant cable-hose systems.* Noise Control Engineering Journal, 1997. **45**(6): p. 235-242.

41. Yu, J. and E. Kojima, *Wave propagation in fluids contained in finite-length anisotropic viscoelastic pipes.* Journal of the Acoustical Society of America, 1998. **104**(6): p. 3227-3235.

42. Yu, J. and E. Kojima, *Dynamic response of unhomogeneously viscoelastic fluid lines*, in *American Control Conference*1995: Seattle, Washington. p. 1821-1825.

43. Johnston, D.N., T.M. Way, and K.M. Cone, *Measurement of wave propagation characteristics of flexible hoses*, in *2007 ASME International Mechanical Engineering Congress and Exposition*2007. p. 159-167.

44. Longmore, D.K., D.N. Johnston, and J.E. Drew, *Measurement of the dynamic properties of hose walls required for modelling fluid-borne noise.* Fluid Power Systems and Technology, 1997. **4**: p. 105-111.

45. Manson, J.A. and L.H. Sperling, *Polymer blends and composites*. 1976, New York: Plenum Press.

46. Capps, R.N., *Dynamic Young's moduli of some commercially available polyurethanes.* Journal of the Acoustical Society of America, 1983. **73**(6): p. 2000-2005.

47. Bicerano, J., *Prediction of polymer properties*. 3rd ed. 2002, New York: Marcel Dekker, Inc.

48. Williams, M.L., R.F. Landel, and J.D. Ferry, *The temperature dependence of relaxation mechanisms in amorphous polymers and other glass-forming liquids.* Journal of the American Chemical Society, 1955. **77**: p. 3701-3707.

49. Questad, D.L., et al., *Pressure-volume-temperature studies of a polyurethane elastomer.* Journal of Applied Physics, 1982. **53**(10): p. 6578-6580.

50. Huang, J.S. and L.J. Gibson, *Elastic moduli of a composite of hollow spheres in a matrix.* Journal of Mechanical Physics in Solids, 1993. **41**(1): p. 55-75.

51. Poveda, R., N. Gupta, and M. Porfiri, *Poisson's ratio of hollow particle filled composites.* Materials Letters, 2010. **64**: p. 2360-2362.

52. Buchanan, J.L., *Numerical solution for the dynamic moduli of a viscoelastic bar.* Journal of the Acoustical Society of America, 1987. **81**(6): p. 1775-1786.

53. Willis, R.L., et al., *An experimental-numerical technique for evaluating the bulk and shear dynamic moduli of viscoelastic materials.* Journal of the Acoustical Society of America, 1997. **102**(6): p. 3549-3555.

54. Sajo, T., *Antireflective materials at ultrasound frequencies.* Journal of the Acoustical Society of America, 1986. **79**(1): p. 18-25.

55. Marur, P.R., *Numerical estimation of effective elastic moduli of syntactic foams.* Finite Elements in Analysis and Design, 2010. **46**: p. 1001-1007.

56. Tagliavia, G., M. Porfiri, and N. Gupta, *Vinyl ester-glass hollow particle composites: Dynamic mechanical properties at high inclusion volume fraction.* Journal of Composite Materials, 2009. **43**(5): p. 561-582.

57. Baird, A.M., F.H. Kerr, and D.J. Townend, *Wave propagation in a viscoelastic medium containing fluid-filled microspheres.* Journal of the Acoustical Society of America, 1999. **105**(3): p. 1527-1538.

58. Antunes, F.V., J.A.M. Ferreira, and C. Capela, *Numerical modelling of the Young's modulus of syntactic foams.* Finite Elements in Analysis and Design, 2011. **47**: p. 78-84.

59. Yuan, Y.-L. and Z.-X. Lu, *Modulus prediction and discussion of reinforced syntactic foams with coated hollow spherical inclusions.* Applied Mathematics and Mechanics (English Ed.), 2004. **25**(5): p. 528-535.

60. Song, B., et al., *Temperature effects of dynamic compressive behavior of an epoxy syntactic foam.* Composite Structures, 2005. **67**: p. 289-298.

61. Gaunaurd, G., E. Callen, and J. Barlow, *Pressure effects on the dynamic effective properties of resonating perforated elastomers.* Journal of the Acoustical Society of America, 1984. **76**(1): p. 173-177.

62. Gupta, N., et al., *Characterization of mechanical and electrical properties of epoxy-glass microballoon syntactic composites.* Ferroelectrics, 2006. **345**: p. 1-12.

63. Gupta, N. and E. Woldesenbet, *Microballoon wall thickness effects on properties of syntactic foams.* Journal of Cellular Plastics, 2004. **40**: p. 461-480.

64. Sankaran, S., et al., *Characterization of epoxy syntactic foams by dynamic mechanical analysis.* Journal of Materials Science, 2006. **41**: p. 4041-4046.

65. Gupta, N. and W. Ricci, *Comparison of compressive properties of layered syntactic foams having gradient in microballoon volume fraction and wall thickness.* Materials Science and Engineering A, 2006. **427**: p. 331-342.

66. Rongong, J.A., et al., *Damping properties of syntactic foams with nanoparticulate additives*, in *Ninth International Conference on Vibrations in Rotating Machinery*2008, IMechE: University of Exeter, UK. p. 745-759.

67. Trivett, D.H., H. Pincon, and P.H. Rogers, *Investigation of a three-phase medium with a negative parameter of nonlinearity.* Journal of the Acoustical Society of America, 2006. **199**(6).

68. Wheeler, J.H. and J.P. Frentzos, *Fluid noise muffler and method of manufacture*, in *USPTO*, USA patent no. 5426270. The Texacone Company, Mesquite, TX, 1995.

69. DiRe, J., *Hydraulic pump with foamed elastomeric member in outlet chamber to reduce liquid-borne noise*, in *USPTO*, USA patent no. 5,180,298. IMO Industries, Inc., 1993.

70. Marek, K.A., N.E. Earnhart, and K.A. Cunefare, *Model and analysis of a cylindrical in-line hydraulic suppressor with a solid compressible liner*. Journal of Sound and Vibration, 2014.

71. Standardization, I.O.f., *Hydraulic fluid power - Determination of fluid-borne noise characteristics of components and systems - Part 2: Measurement of speed of sound in a fluid in a pipe*, 2000, International Organization for Standardization: Geneva, Switzerland.

72. Johnston, D.N., D.K. Longmore, and J.E. Drew, *A technique for the measurement of the transfer matrix characteristics of two-port hydraulic components*. Fluid Power Systems and Technology, 1994. **1**: p. 25-33.

73. Earnhart, N.E. and K.A. Cunefare, *Compact Helmholtz resonators for hydraulic systems.* International Journal of Fluid Power, 2012. **13**(1): p. 41-50.

74. Earnhart, N.E., *Modeling and validation of a syntactic foam lining for noise control devices for fluid power systems*, in *Mechanical Engineering*2012, Georgia Institute of Technology: Atlanta, GA, USA.

75. Achenbach, J.D., *Wave propagation in solids*. 1975, New York: Elsevier.

76. Lawrie, J.B. and R. Kirby, *Mode-matching without root-finding: Application to a dissipative silencer.* Journal of the Acoustical Society of America, 2006. **119**(4): p. 2050-2061.

77. *CES EduPack*, 2011, Granta Design Limited: Cambridge, UK.

78. Gruber, E.R., *Optimal configuration of adjustable noise suppressors*, in *Mechanical Engineering*2013, Georgia Institute of Technology: Atlanta, GA.

79. Morse, P.M. and K.U. Ingard, *Theoretical Acoustics*. 1968, New York: McGraw-Hill, Inc.

80. Gruber, E.R., et al., *Optimization of single and dual suppressors under varying load and pressure conditions.* International Journal of Fluid Power, 2014. **14**(3): p. 27-34.